2001

X -Ray Absorption Fine Structure (EXAFS and XANES) and Microscopic Investigations of Supramolecular Systems.

Pierre Nicolas Floriano
Louisiana State University and Agricultural & Mechanical College

INFORMATION TO USERS

This manuscript has been reproduced from the microfilm master. UMI films the text directly from the original or copy submitted. Thus, some thesis and dissertation copies are in typewriter face, while others may be from any type of computer printer.

The quality of this reproduction is dependent upon the quality of the copy submitted. Broken or indistinct print, colored or poor quality illustrations and photographs, print bleedthrough, substandard margins, and improper alignment can adversely affect reproduction.

In the unlikely event that the author did not send UMI a complete manuscript and there are missing pages, these will be noted. Also, if unauthorized copyright material had to be removed, a note will indicate the deletion.

Oversize materials (e.g., maps, drawings, charts) are reproduced by sectioning the original, beginning at the upper left-hand corner and continuing from left to right in equal sections with small overlaps.

Photographs included in the original manuscript have been reproduced xerographically in this copy. Higher quality 6" x 9" black and white photographic prints are available for any photographs or illustrations appearing in this copy for an additional charge. Contact UMI directly to order.

ProQuest Information and Learning
300 North Zeeb Road, Ann Arbor, MI 48106-1346 USA
800-521-0600

X-RAY ABSORPTION FINE STRUCTURE (EXAFS AND XANES) AND MICROSCOPIC INVESTIGATIONS OF SUPRAMOLECULAR SYSTEMS

A Dissertation

Submitted to the Graduate Faculty of the
Louisiana State University and
Agricultural and Mechanical College
in partial fulfillment of the
requirements for the degree of
Doctor of Philosophy

in

The Department of Chemistry

by
Pierre Floriano
D. E. A. University of Franche-Comté, Besançon, France, 1994
May 2001

Dedication

This dissertation is dedicated to:

My mother, Claudine Jacquin

My father, Gerard Floriano

My sister, Sylvie Peltier

my nephew, Julien Peltier

Thank you for your love and support despite the distance

My wife Christy Witt, without whom all of this would not have been possible

Thank you for your love, support, motivation and tolerance

and all my family and friends,

in France and in the U.S.

Finally,

Professor Alain Chambaudet and Michel Fromm, thank you for believing in me,

motivating me and thank you for your trust

and thank you Tintin and Milou

Acknowledgments

This work would not have been possible without the guidance of both of my advisors, Dr. Robin L. McCarley and Dr. Erwin D. Poliakoff. Thank you both for giving me the opportunity to work with you on this joint project that I have thoroughly enjoyed during my stay at Louisiana State University. This highly interesting research area helped me redefine my career goals and ambitions. I would also like to acknowledge Dr. Roland C. Tittsworth, John M. Schoonmaker, and the entire staff at the Center for Advanced Microstructures and Devices (CAMD) for providing me with a great deal of help and discussions about EXAFS experiments. I also had the wonderful opportunity to collaborate with the group of Dr. J. Hormes at the University of Bonn, Germany. I am very thankful for all the help that their group provided. Thanks to Cindy Henk and Dr. J. Jiang for help with the TEM work.

Being a part of two research groups was a very unique experience allowing me to learn about a wider range of scientific issues. I thank my past and present fellow group members and wish them the best of luck for their personal lives and careers. Finally, I would like to thank my family in France and in America, and especially my wife, Christy J. Witt who also went through the hardships and the good times of graduate school with me to earn a Ph. D. of her own in Psychology. The financial support for this work was provided by the U.S. National Science Foundation (RLM, CHE-9529770; EDP, CHE-9616908), LSU, and CAMD.

Table of Contents

List of Tables

List of Figures

Abstract

Self-assembled monolayers of n-alkanethiols, CH_3-$(CH_2)_x$-SH, on Au, Ag, and Cu have been studied with Grazing incidence EXAFS (GIXAFS) at the sulfur K-edge. Characterization of the bonding of self-assembled monolayers is of great interest because of their ability to tailor physical and chemical properties of surfaces. For both pentanethiol and decanethiol monolayers on Ag and Cu, the three-fold hollow site is found to be the most probable sulfur binding site. However, observations for octadecanethiol indicate that the three-fold-hollow site is not the exclusive binding site. In addition, the possible existence of disulfide bonds on the metal surface (adsorbed dialkyldisulfides) is not supported by the data. In addition, careful examination of the systems by XANES clearly demonstrate the peculiar behavior of octadecanethiol on surfaces. Preliminary results from monolayers on Au are also reported and constitute the first ever reported EXAFS data for alkanethiol monolayers on gold. These findings represent a great advance for the investigation of thin films on surfaces, and also present the possibility to study mixed monolayers as a complement to scanning probe microscopy.

Recently, dendritic systems, and especially dendrimer-metal complexes, have been shown to have outstanding properties which make them suitable for applications in catalysis and biology. Our long-term plans include investigations of adsorbed dendrimer-metal complexes on metal surfaces through the use of grazing incidence EXAFS. Preliminary X-ray absorption studies of poly(propylene imine) dendrimer-copper(II) complexes of generation 1-5 in powder form and methanolic solution are presented here. XANES allows determination of the oxidation state of the copper species and the geometry of the copper complex whereas EXAFS gives us information

about bond distances, coordination number and nature of the neighbor atoms. When reacted with $NaBH_4$, these dendrimer-copper complexes undergo reduction which leads to the formation of Cu(0) nanoclusters. We investigated these clusters by EXAFS, XANES, ultra violet-visible spectroscopy and high resolution transmission electron microscopy (HR-TEM) and discuss their geometry, composition and size depending on the dendrimer generation. The synthesis of metallic nanoclusters by the dendrimer route has been successful to produce nanoclusters of reduced size and increased monodispersity.

Chapter 1. Introduction

1.1. Introduction

The work presented in this dissertation focuses on investigations targeting the structure of supramolecular systems widely used in a variety of applications such as biosensensing, biomimetics, molecular electronics, wetting, and lubrication, to name a few. Such systems include single-component, self-assembled monolayers (SAMs) of *n*-alkanethiols (CH_3-$(CH_2)_{x-1}$-SH, hereafter referred to as C_x) adsorbed on various metal substrates, two-component or mixed SAMs, dendrimers in solution, powder, or on surfaces, or a combination of all of these. A large body of literature has been published in an attempt to fully characterize these systems and understand their physical and chemical properties.[1-78] The driving force behind this investigation of these systems is to gain an understanding of their properties on the nanometer scale so that future studies can be carried out to optimize their role in current applications and in the fabrication of nanoscale materials. Despite the large number of techniques employed to characterize these systems, questions of fundamental importance remain concerning specifically the bonding of the alkanethiols to the surface. The work described in this dissertation presents ways to access to the knowledge of the direct chemical environment of a particular chemical entity, and thus leads to information about the metal-sulfur interface in the case of alkanethiol monolayers or the metal coordination in the case of metal-encapsulated dendrimers.

The first family of compounds, alkanethiol SAMs on metals, have attracted the attention of a large number of research groups, and as a result, a great amount of knowledge has been obtained over the past 20 years. Initial interest in these systems originated from the ease of preparation of these highly ordered monomolecular films,

the reproducible manner in which they can be prepared, and their stability under a wide range of experimental conditions.[38,49,57,65,71,76] Alkanethiols self assemble on various metallic substrates, resulting in a two-dimensional structure that provides a unique scenario for investigating the interplay between the molecular (nanoscopic) structure of the sulfur-metal interface and the macroscopic properties of the monolayer. The possibility of controlling the properties of the monolayer by manipulating the monolayers structure (substrate type and orientation, alkane chain length, ω-substituent, etc.) has made and still makes these films very useful for wettability studies, corrosion inhibition, adhesion studies, and platforms for molecular devices.

In addition, it is possible to control the composition of these alkanethiol monolayers so that surfaces bearing selected functionalities can be designed and serve as sensors for a given functional group, atom, or molecule. For example, miniaturized immuno-assay-like sensors can be made by relying on the selectivity of the end groups (ω-substituents) and recognition of such groups by analytes in solution and vice versa.[79,80] It is also possible to intercalate electroactive species within the monolayer and fabricate arrays of conductive material within an insulating matrix. The design of such monolayers presents a ideal way of studying electron transfer theories.[11,12,81]

In all of the above examples, the overall properties of the monolayer very often depend on the functionality of the end group, but there are other factors that intervene during the formation of these films and their influence must be evaluated. The first factor that comes to mind is the chain length of the SAM; the molecular order of the SAM is dictated by the strong sulfur-metal bond and the degree of van der Waals interactions between the chains. Therefore, the number of methylene units will affect the properties of the monolayer (crystallinity, as has been shown in many studies).

Also, the bonding of the sulfur head group plays a role in the macroscopic properties of the SAMs because sulfur is the anchoring agent of the chains to the surface. Although scientists do not unanimously agree on the exact bonding scheme of alkanethiols to the metallic substrate, the strength of the S-Au bond has been shown to be ≈ 44 kcal/mol.[45,75,80] However, the effect of the bonding of the sulfur group (bond angle, order, etc.) on the metal surface on the properties of the SAM has not been precisely determined. Ultimately, the combination of these factors (chain order and S-M interaction) needs to be further investigated in order to provide a complete picture of these systems.

A great number of studies have focused on alkanethiol SAMs on the coinage metals and much information has been gained regarding effects on alkane chain order. However, fewer studies have focused on the sulfur-metal bond. In order to have access to the direct chemical environment of the sulfur atoms constituting the monolayer, we need a non-destructive technique that is capable of probing the sulfur-metal interface and yields a large quantity of information about the sulfur-metal bond. In particular, the desired technique must render structural information, and display excellent sensitivity. Extended X-ray absorption fine structure (EXAFS) appears to be the method of choice because it is element specific and sensitive enough to probe the sulfur layer so as to detect chemical effects, such a variation in oxidation state. In addition, EXAFS provides a way to access structural parameters such as bond distances, and coordination numbers, both of which will lead to elucidation of the way in which the sulfur head group bonds onto the metal surface.

Although EXAFS studies of the S K-edge for alkanethiol SAMs seemed to be ideal at the onset of this research, further experimental development was needed to

overcome the challenge of probing the single layer of sulfur on a 200-nm-thick metallic substrate that may exhibit interfering effects. One of the purposes of this work is demonstration of succesful use of EXAFS to obtain information on the bonding of alkanethiols in SAMs. To initiate the work at hand, a collaboration with a German group at the university of Bonn to develop a grazing incidence EXAFS (GIXAFS) fluorescence technique was undertaken. This work shows that by probing the sulfur layer at very grazing angles (typically on the order of hundredths of degrees), GIXAFS yields better sensitivity and a better S/N ratio, and consequently, more meaningful data when compared to the existing published EXAFS data of alkanethiols on Ag and Cu. The influence of chain length of the alkanethiol (C_5, C_{10}, C_{18}) on the bonding of the sulfur on the surface was investigated. It was found that the bonding model for C_{18} is different from that for C_5 and C_{10}. Furthermore, the chain length of the thiol was found to have an influence on the distribution of sulfur atoms on the metal surface (Cu or Ag).

A significant challenge of the work here was acquisition of data for alkanethiols adsorbed on Au, which represents the ultimate difficulty of extracting a weak sulfur fluorescence signal from the fluorescence emitted by the relatively thick Au layer. This challenge was met through the use of GIXAFS at the S K-edge and the data for such experiments reported for the first time. These experiments were performed at Louisiana State University's Center for Advanced Microstructures and Devices (CAMD). Various chain length alkanethiols on Ag were investigated, and it was found that C_{18} exhibited a different spectrum compared to those of C_6, C_{12}, C_{14}, C_{16}, and C_{22}, thereby corroborating the EXAFS data obtained in Germany. With the goal of investigating mixed monolayers in mind, the GIXAFS technique was also used to probe the iron center in ferrocene-terminated SAMs. These preliminary studies on the Fc-SAMs

indicate that future, more thorough GIXAFS investigations are possible for two-component SAM systems, and such results can possibly be used in conjunction with data from lateral force microscopy experiments.

In addition to the alkanethiol/metal supramolecular systems discussed above, scientists from various fields have been investigating the intriguing properties of dendritic molecule systems. These hyperbranched molecules are obtained by the repetitive addition of a building unit to an initiator core. Thus, their dendritic structure provides for polyfunctionality with the possibility of extending 2D SAM systems to a 3D structure. The quantity of literature on dendritic systems continues to grow exponentially, generating more and more research on their properties and potential applications.

Another interesting aspect of certain dendrimers is that of their ability to complex with metal ions to form multi-charged supramolecular complexes. In addition, these complexes can be used to produce metal nanoclusters upon reduction, which makes such a "template-assisted" method of making metal clusters very attractive in heterogeneous catalysis applications. Despite the extensive published work on these systems at the onset of the work described here, a number of questions remained unanswered. Very little was known about the structure of the dendrimer-metal complex itself, the dendrimer-metal complex geometry, and the coordination chemistry about the metal ion centers. Additionally, researchers are interested in finding the optimal conditions to produce very small monodisperse metallic nanoclusters and control their location with respect to the dendrimer interior. Because of the success of GIXAFS as applied to probing sulfur in SAMs on Ag, Cu, and Au, and also Fe in Fc-terminated SAMs, we envision a series of experiments that study the catalytic behavior of these

nanoclusters on surfaces. In order to assess the validity of conventional EXAFS for metal-dendrimer composites, powder and solution samples of copper-encapsulated poly(propylene imine) dendrimers were synthesized and studied. We acquired EXAFS and XANES spectra in order to obtain information on the binding of the metal ions to the dendrimer functionalities, and the size, composition and location of the metal nanoclusters formed upon reduction of the metal ion-dendrimer template. In particular, the geometry of the Cu(II) complex end group of the dendrimer was determined to be that of a square-based pyramid with three nitrogen atoms (Cu - N distance ≈ 2.03 Å) and 1 oxygen atom (Cu - O ≈ 1.94 Å) in the equatorial plane and 1 axial oxygen atom at about 2.6 Å. The information contained in the EXAFS data for the reduced complexes allowed us to assess the size of the copper nanoclusters through the use of structural parameters. These results were compared to data obtained from transmission electron microscope (TEM) images. The size and dispersity of the nanoclusters was shown to decrease as a function of increasing dendrimer generation. In addition, the sizes of the nanoclusters were compared to those of the dendrimers and conclusions were made about the location of the nanoclusters with respect to the dendrimer interior.

1.2. Alkanethiol Self-Assembled Monolayers

Self-assembled monolayers (SAMs) of alkanethiols (CH_3-$(CH_2)_x$-SH) adsorbed onto different metallic substrates (Ni, Pt, Cu, Ag, Au, Al) have attracted the attention of researchers for the past two decades due to their ease of preparation and diversified applications in wetting,[30,31,82] corrosion inhibition,[57,83] sensing, lubrication and biological systems.[79,80] SAMs are obtained by immersion of a clean metallic substrate in an ethanolic thiol solution, which results in the formation of metal thiolates. The most commonly studied systems consist of SAMs of alkanethiols on gold. Alkanethiol

SAMs on gold are popular because they are relatively easy to prepare, robust, densely packed, and because gold is known to be stable and resistant to oxidation.[38,49,57,65,71,76] A large variety of techniques has been employed to obtain information on the structure of alkanethiol SAMs and their chemical and physical properties. Figure 1.1 represents a self-assembled monolayer of alkanethiols adsorbed onto a metallic substrate and the different stages of the assembly process. It is generally believed that the sulfur head group of the thiol loses its hydrogen atom upon adsorption which results in the creation of a gold thiolate on the surface.[84,85] The alkanethiol is strongly chemisorbed onto the surface and the chains are ordered by the van der Waals interactions between the polymethylene units resulting in a tilt which is defined as the tilt angle (α). The tilt angle of the chain results from an equilibrium between chemisorption and Van der Waals interactions.[10,20,42,45,76,80]

The adsorption process, orientation of the chains, and bonding of the thiols to the surface have been studied by ellipsometry,[19,47,65,71] reflection/absorption infrared spectroscopy (RAIRS),[19,76] scanning tunneling microscopy (STM),[10,29,37,40,52,82,86,87] scanning probe microscopy (SPM),[12,33,34,55,73,74,88,89] infra-red or Raman spectroscopy,[10,23,30,40,43] low energy electron diffraction (LEED),[76,86] X-ray photoelectron spectroscopy(XPS),[8,13,31,43,47,56,60,65,71,78,86,90,91] surface plasmon resonance (SPR),[16,59,92] high energy electron energy loss spectroscopy (HREELS),[14,28] electrochemical techniques,[12,22] grazing incidence X-ray diffraction,[71,74] EXAFS,[27,82,93] and NEXAFS.[13,23,27,38,56,94,95] Reviews that summarize this work are also available.[75,80,82]

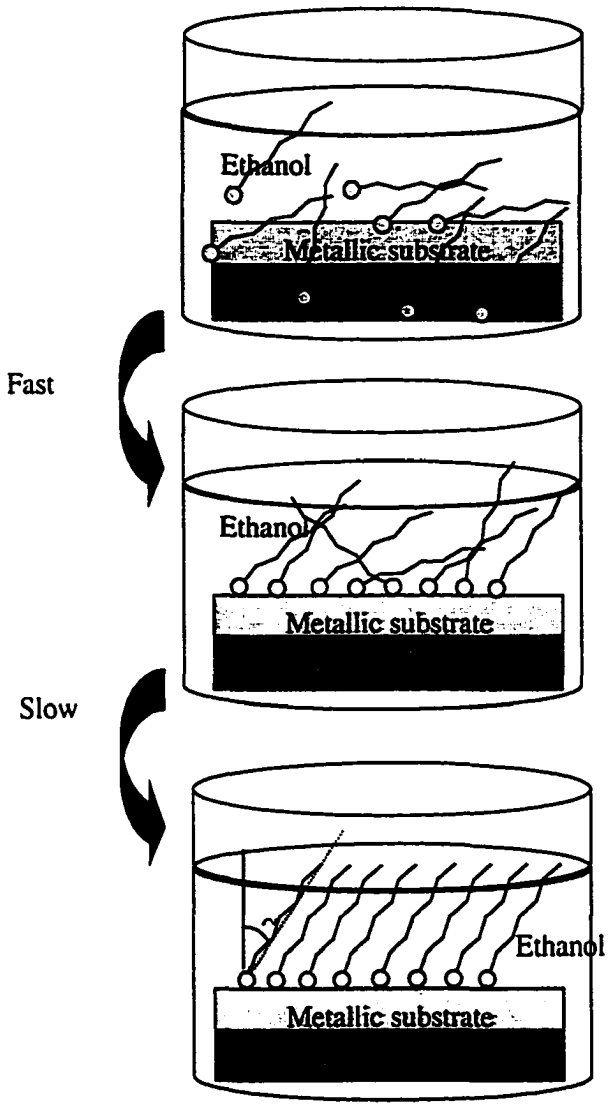

Figure 1.1. Representation of the self-assembly process of alkanethiols onto a metallic substrate.

The research described in this dissertation focuses on the characterization of the sulfur head-group bonding to the metallic substrate by means of EXAFS and XANES. Collectively, these studies can provide information on the local environment of the sulfur atom, leading to the elucidation of the bonding sites. As was previously mentioned, EXAFS and XANES have been used by other research groups to investigate thiol SAMs. In particular, carbon K-edge XANES has been utilized to investigate the

alkanethiol adsorption process,[23] or the orientation of the chains.[56,62,96] Prior to the work described here,[18] only two studies have focused on the sulfur K-edge.[27,93]

We are interested in determining the influence of the chain length of the thiol on the sulfur-metal (S-M) bond and the carbon-sulfur-metal (C-S-M) angle by examination of the EXAFS spectra of various thiols on Cu, Ag, and Au. EXAFS data will provide us with the coordination number for the sulfur atoms, a number which is indicative of the position of the sulfur atoms on the surface.

A generally well accepted model for the adsorption of alkanethiols on gold is the $(\sqrt{3}\times\sqrt{3})R30°$ model in which the sulfur atom of the thiol adopts a three-fold coordination to the hexagonal gold lattice and thus sits in a three-fold hollow site. The sulfur-to-sulfur distance for the adsorbate unit cell is dictated by the metal unit cell; Thus, for Au, the sulfur-to-sulfur distance is 4.97 Å (2.88 Å × $\sqrt{3}$). This binding model, as well as the possibility of the sulfur sitting in an atop position, is depicted in Figure 1.2. However, another adsorption scheme where two alkanethiols bind on the metal surface to form dialkyldisulfides has also been proposed elsewhere[27,70,71,92,97] and will be considered in this dissertation. Because the tethering of the alkanethiol on the surface will ultimately influence the overall properties of the monolayer, it is of great importance to further characterize the sulfur-metal interface and clarify the previously mentioned points.

1.3. Mixed SAMs

SAMs can also be constituted of more than one alkanethiol species and are referred to as mixed monolayers. Such systems are interesting due to their direct applications to biomolecular recognition and molecular electronics. A schematic of a mixed alkanethiol SAM is given in Figure 1.3. When designing such two-body

structures, it is important to understand the distribution of the components on the surface in terms of the intermixing of its constituents. For example, does the adsorption process result in a homogeneous combination of both of the precursors or the creation of domains of one of the components within the other (phase separation).[21,98]

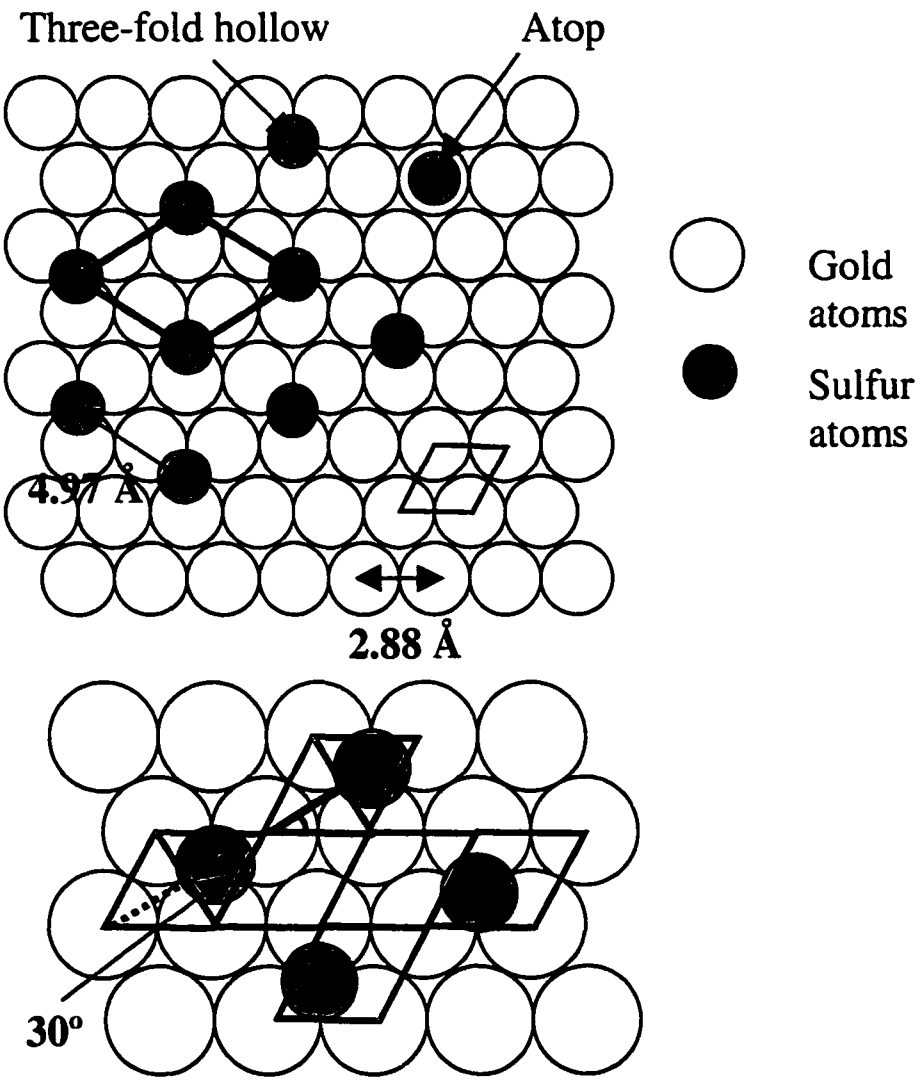

Figure 1.2. $(\sqrt{3}\times\sqrt{3})R30°$ binding model of the alkanethiols on gold.

When two different alkanethiols co-adsorb on a metallic substrate, a generally well accepted result is that long chain thiols adsorb preferentially to short chain ones.[30] Using a gold electrode immersed with a mixture solution of short and long chain alkanethiols, Chailakapul et al. have shown that over time, the short chain thiols were exchanged to finally form a monolayer of only the long chain thiol.[99] However, less information is available on the characterization of mixed alkanethiol SAMs of similar chain length and/or functionalized with different end groups. Overney et al.[100] demonstrated how a frictional force microscope could be used to provide information on chemical mapping of Langmuir-Blodgett (LB) films. Later, Frisbie et al.[101] described how the sensitivity of scanning probe microscopes could be improved by modifying the probe tip with functional groups so that mapping of chemically distinct domains on the surface could be obtained. Different mixed monolayers like 4-aminothiophenol (4-ATP)/C_{18},[98] 4-ATP/thiophenol,[102] C_{16}/3-Mercaptopropionic acid (3-MPA),[103] or carboxylic acid-terminated alkanethiol/stearic acid[21] were then studied on gold.

Willicut and McCarley showed that pyrrole films on gold modified with pyrrole-terminated alkanethiols were greatly stabilized compared to pyrrole films on bare Au.[104] Mixed films containing pyrrole-terminated thiols and *n*-alkanethiols could be conceived to build well defined architecture of stable pyrrole film on the surface. Using the ability of scanning probe microscopy (SPM) to map chemically distinct domains, we studied systems where C_{18} is co-adsorbed with pyrrole-terminated hexanethiol (SH-C_6-Py) by lateral force microscopy (LFM). The behavior of monolayers composed with different molar fraction of its constituents was investigated.

We performed frictional coefficient measurements for a series of monolayers made of different molar fraction of SH-C_6-Py and ODT in ethanol and investigated the ability of the monolayers to phase separate. These studies suffered from poor reproducibility of the determined values for the friction coefficient. However, a general trend denoting the influence of the composition of the monolayer on the coefficient of friction could be observed. The discrepancies between these results and results obtained on different monolayers by other groups could be explained by possible contamination of the tip over time.

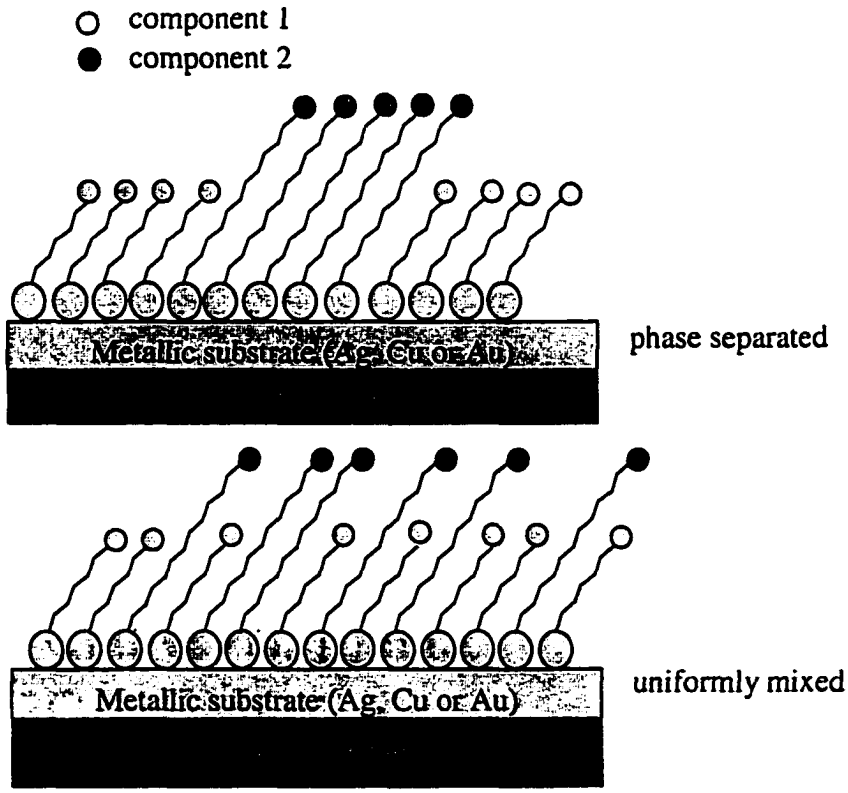

Figure 1.3. Cartoon of a mixed alkanethiol SAM and the possible surface structures of the film.

Grazing incidence EXAFS, as shown by the work on the alkanethiol monolayers on Ag, Cu, and Au, offers the possibility to probe the sulfur monolayer but could also provide an insight into the structure of the outmost layer in the case of mixed

monolayers. Our beamline facilities currently do not allow us to carry out nitrogen K-edge EXAFS experiments. In order to test the applicability of grazing incidence EXAFS to probe the outmost layer of the SAM, we obtained preliminary data for ferrocene-terminated SAMs by means of GIXAFS at the Fe K-edge. The preliminary GIXAFS data involving ferrocene-terminated alkanethiol/C_{18} mixed monolayers clearly proves the sensitivity and limit of detection of this technique is sufficient, and obtaining information about both the sulfur and the ferrocene environments is possible. Additionally, these results indicate the possibility of using GIXAFS at the N K-edge to probe the pyrrole-terminated monolayers.

1.4. Dendritic Systems

Other supramolecular systems such as dendrimers are capable of self-assembly[105] on various substrates and could contribute to new ways of making nanoscale devices. In the last decade, dendritic molecules have caught the attention of a number of researchers due to their outstanding properties that make them suitable to a broad range of applications.[106-108] Dendrimers can serve not only as contrast agents in magnetic resonance imaging,[109] drug delivery systems in medicine,[110,111] but are expected to contribute significantly in the fields of catalysis,[112,113] molecular recognition,[108] light harvesting[114] and environmental studies,[115] to name a few.

Poly(amidoamine), PAMAM, and poly(propylene imine)-diaminobutane core, DAB, dendrimers, as well as other dendrimers, have been shown to form complexes with metal ions.[116-131] Such metal-ion-dendrimer precursor species can be used to produce metal nanoparticles upon reduction of the dendrimer-metal complexes.[116-119,121,124,125,127,129] Both the dendrimer-metal-ion precursors and the resulting metal nanoparticles have been investigated using structural tools such as electron

paramagnetic resonance (EPR), ultraviolet and visible spectroscopy (UV-vis), and transmission electron microscopy (TEM). Although a large number of studies have focused on making metal nanoparticles from metal-PAMAM complexes (Au,[116-119] Ag,[116,118] Cu,[121,124,125] Pd,[127,129] and Pt.[127]), we know of no reports focusing on the use of metal-DAB dendrimer complexes for the fabrication of metal nanoclusters.

DAB dendrimers have been shown to form well-defined, stoichiometric complexes with ionic Cu, Zn, Ni and Co,[130,131] an attribute that may allow for control over the properties of metal nanoclusters derived from such metal-ion-dendrimer complexes. To this end, it would be of great importance to have the ability to obtain structural information for the metal ion complexed in the dendrimer, as well as information regarding the nature of the dendrimer-metal nanoparticle structure following reduction. We report here, for the first time, an investigation of Cu(II)-poly(propylene imine) dendrimer complexes (Figure 1.4) with a diaminobutane core (DAB-Am_n-$Cu(II)_x$, n=4 to 64, x=n/2) by means of extended X-ray absorption fine structure (EXAFS) and X-ray absorption near-edge structure (XANES) spectroscopies. By studying the EXAFS and XANES spectra of DAB-Am_n-$Cu(II)_x$ at the copper K-edge, we have been able to determine the geometry of the dendrimer end-group complex about the Cu ion and parameters such as bond distances, coordination numbers and nature of the ligands contributing to the copper coordination sphere.

In addition, we have studied the properties of the Cu(0) nanoclusters that result upon reduction of the DAB-Am_n-$Cu(II)_x$ template precursors. The size of the Cu(0) nanoclusters is determined from TEM data, and EXAFS measurements are used to understand the local environment of the reduced Cu nanoclusters. The EXAFS data are useful for correlating the present data with the outcomes from previous studies of

nanoparticles.[132-134] The TEM and EXAFS studies demonstrate that the size of the Cu(0) nanoclusters decreases with increased generation of the dendrimer.

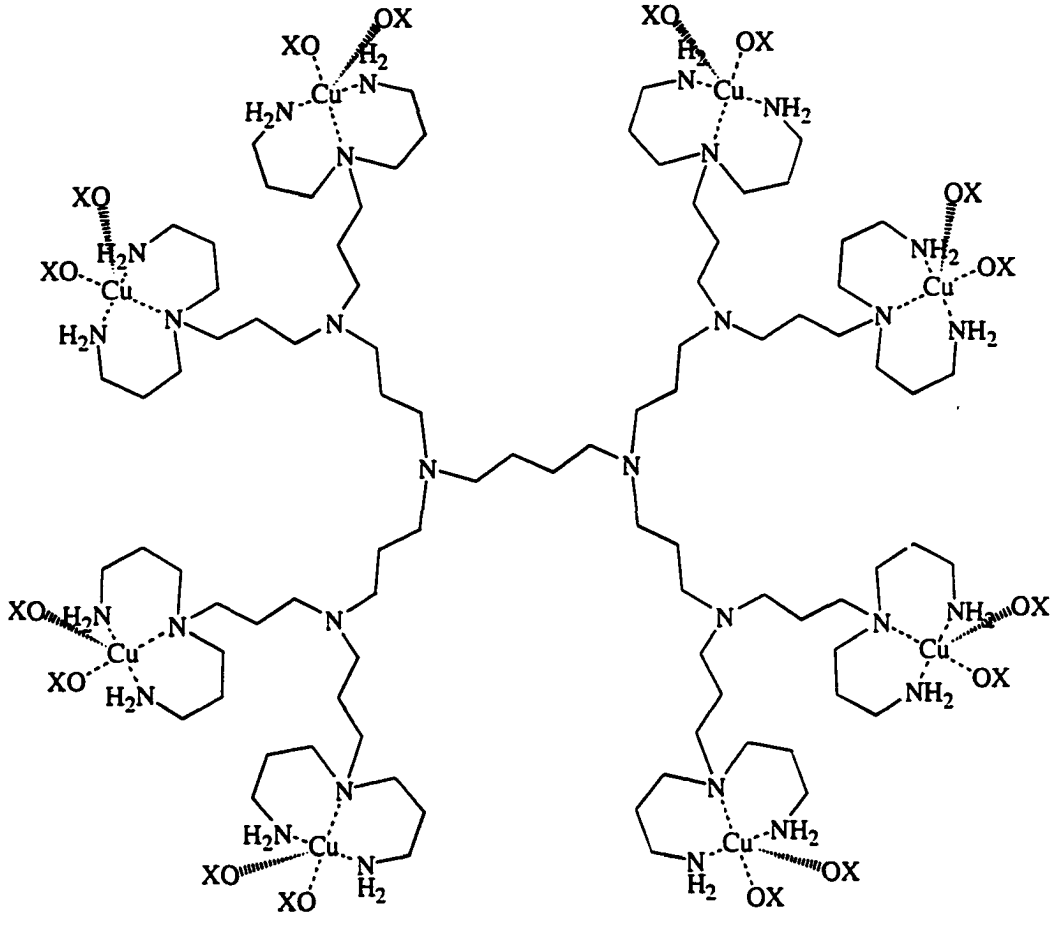

Figure 1.4. Representation of the DAB-Am_{16}-$Cu(II)_8$ complexes.

Based on the observed relationship between nanocluster size and dendrimer generation, we propose that the dendrimers coat the incipient copper nanocluster surfaces (Cu(0) nuclei) via Cu-N bonds. The "surfactant-like" dendrimer coating effectively inhibits the nascent Cu(0) nuclei from growing larger only if the steric interactions between Cu(0) atoms/nuclei and the various-sized dendimers is sufficiently large.

These studies that were performed on dendrimers in the powder or solution state show the importance of EXAFS and XANES as a tool for probing their physical and chemical properties. A combination of the work performed with the alkanethiol SAMs and the dendrimers would provide a great deal of information on the behavior of these compounds on surfaces. Indeed, researchers have shown a great interest in immobilizing dendrimers on surfaces and in some instances integrating them within alkanethiol SAMs.[50,135-139] PAMAM dendrimers have been shown to experience variations in their shape upon adsorption onto a surface but very little is known about their structural conformation.[50,135] As changes in the adsorbed dendrimer morphology have been observed by AFM in the case of the PAMAM dendrimers, it would be interesting to study the influence of these changes on the DAB-Am_n-$Cu(II)_x$ complex geometry when adsorbed on a surface. Because a small amount of a Cu-Cu interaction was observed in the EXAFS data for the powder of the DAB-Am_n-$Cu(II)_x$ complexes, it is possible, for example, that the distance between the metal atoms in the adsorbed dendrimers is small enough to have an impact on the EXAFS spectra. Grazing incidence EXAFS has been proven to be sensitive enough to detect very small structural changes, thereby offering the possibility of elucidating structural variations in the conformation of the adsorbed dendrimers.

1.5. Bibliography

1.1) Badia, A.; Gao, W.; Singh, S.; Demers, L.; Cuccia, L.; Reven, L. *Langmuir* **1996**, *12*, 1262-1269.

1.2) Badia, A.; Cuccia, L.; Demers, L.; Morin, F.; Lennox, R. B. *J. Am. Chem. Soc.* **1997**, *119*, 2682-2692.

1.3) Beardmore, K. M.; Kress, J. D.; Gronbech-Jensen, N.; R., B. A. *Chem. Phys. Lett.* **1998**, *286*, 40-45.

1.4) Bensebaa, F.; Zhou, Y.; Deslandes, Y.; Kruus, E.; Ellis, T. H. *Surf. Sci.* **1998**, *405*, L472-L476.

1.5) Berger, R.; Delamarche, E.; Lang, H. P.; Gerber, C.; Gimzewski, J. K.; Meyer, E.; Guntherodt, H.-J. *Appl. Phys. A* **1998**, *66*, S55-S59.

1.6) Camillone III, N.; Leung, T. Y. B.; Schwartz, P.; Eisenberger, P.; Scoles, G. *Langmuir* **1996**, *12*, 2737-2746.

1.7) Carg, N.; Friedman, J. M.; Lee, T. R. *Langmuir* **2000**, *2000*.

1.8) Castner, D. G.; Hinds, K.; Grainger, D. W. *Langmuir* **1996**, *12*, 5083-5086.

1.9) Cavalleri, O.; Gilbert, S. E.; Kern, K. *Chem. Phys. Lett.* **1997**, *269*, 479-484.

1.10) Chailapakul, O.; Sun, L.; Xu, C.; Crooks, R. M. *J. Am. Chem. Soc.* **1993**, *115*, 12459-12467.

1.11) Chidsey, C. E.; Bertozzi, C. R.; Putvinsky, T. M.; Mujsce, A. M. *J. Am. Chem. Soc.* **1990**, *112*, 4301-4306.

1.12) Creager, S. E.; Rowe, G. K. *Anal. Chim. Acta* **1991**, *246*, 233-239.

1.13) Danneberger, O.; Weiss, K.; Himmel, H., -J.; Jager, B.; Buck, M.; Woll, C. *Thin Solid Films* **1997**, *307*, 183-191.

1.14) Duwez, A., -S.; Yu, L. M.; Riga, J.; Pireaux, J.-J.; Delhalle, J. *Thin Solid Films* **1998**, *327-329*, 156-160.

1.15) Duwez, A.-S.; Yu, L.-M.; Riga, J.; Delhalle, J.; Pireaux, J.-J. *Langmuir* **2000**, *16*, 6569-6576.

1.16) Ehler, T. T.; Malmberg, N.; Noe, L. J. *J. phys. Chem. B* **1997**, *101*, 8043.

1.17) Fischer, D.; Marti, A.; Hahner, G. *J. Vac. Sci. Technol. A* **1997**, *15*, 2173-2180.

1.18) Floriano, P. N.; Schlieben, O.; Doomes, E. E.; Klein, L.; Janssen, J.; Hormes, J.; Poliakoff, E. D.; McCarley, R. L. *Chem. Phys. Lett.* **2000**, *321*, 175-181.

1.19) Garg, N.; Friedman, J. M.; Lee, T. R. *Langmuir* **2000**, *16*, 4266-4271.

1.20) Gerdy, J. J.; Goodard III, W. A. *J. Am. Chem. Soc.* **1996**, *118*, 3233-3236.

1.21) Green, J.-B. D.; McDermott, M. T.; Porter, M. D. *J. Phys. Chem.* **1995**, *99*, 10960-10965.

1.22) Groat, K. A.; Creager, S. E. *Langmuir* **1993**, *9*, 3668-3675.

1.23) Hahner, G.; Woll, C.; Buck, M.; Grunze, M. *Langmuir* **1993**, *9*, 1955-1958.

1.24) Himmelhaus, M.; Eisert, F.; Buck, M.; Grunze, M. *J. phys. Chem. B* **2000**, *104*, 576-584.

1.25) Hines, M. A.; Todd, J. A.; Guyor-Sionnest, P. *Langmuir* **1995**, *11*, 493-497.

1.26) Hostetler, M. J.; Wingate, J. E.; Zhong, C.-J.; Harris, J. E.; Vachet, R. W.; Clark, M. R.; Londono, J. D.; Green, S. J.; Stokes, J. J.; Wignall, G. D.; Glish, G. L.; Porter, M. D.; Evans, N. D.; Murray, R. W. *Langmuir* **1998**, *14*, 17-30.

1.27) Imanishi, A.; Isawa, K.; Matsui, F.; Tsuduki, T.; Yokoyama, T.; Kondoh, H.; Kitajima, Y.; Ohta, T. *Surf. Sci.* **1998**, *407*, 282-292.

1.28) Kluth, G. J.; Carraro, C.; Maboudian, R. *Phys. Rev. B* **1999**, *59*, R10449-R10452.

1.29) Kobayashi, K.; Horiuchi, T.; Ymada, H.; Matsushidge, K. *Thin Solid Films* **1998**, *331*, 210-215.

1.30) Laibinis, P. E.; Nuzzo, R. G.; Whitesides, G. M. *J. Phys. Chem.* **1992**, *96*, 5097-5105.

1.31) Laibinis, P. E.; Bain, C. D.; Nuzzo, R. G.; Whitesides, G. M. *J. Phys. Chem.* **1995**, *99*, 7663-7676.

1.32) Li, T.-W.; Chao, I.; Tao, Y.-T. *J. Phys. Chem. B* **1998**, *102*, 2935-2946.

1.33) Li, L.; Yu, Q.; Jiang, S. *J. Phys. Chem. B* **1999**, *103*, 8290-8295.

1.34) Lio, A.; Morant, C.; Ogletree, D. F.; Salmeron, M. *J. Phys. Chem. B* **1997**, *101*, 4767-4773.

1.35) McCarley, T. D.; McCarley, R. L. *Anal. Chem.* **1997**, *69*, 130-136.

1.36) McDermott, M. T.; Green, J.-B. D.; Porter, M. D. *Langmuir* **1997**, *13*, 2504-2510.

1.37) Poirier, G. E. *Langmuir* **1997**, *13*, 2019-2026.

1.38) Rieley, H.; Kendall, G. K.; Chan, A.; Jones, R. G.; Ludecke, J.; Woodruff, D. P.; Cowie, B. C. C. *Surf. Sci.* **1997**, *392*, 143-152.

1.39) Ron, H.; Rubinstein, I. *Langmuir* **1994**, *10*, 4566-4573.

1.40) Ron, H.; Cohen, H.; Matlis, S.; Rappaport, M.; Rubinstein, I. *J. phys. Chem. B* **1998**, *102*, 9861-9869.

1.41) Rowe, G. K.; Creager, S. E. *J. Phys. Chem.* **1994**, *98*, 5500-5507.

1.42) Schlenoff, J. B.; Li, M.; Ly, H. *J. Am. Chem. Soc.* **1995**, *117*, 12528-12536.

1.43) Schoenfisch, M. H.; Pemberton, J. E. *J. Am. Chem. Soc.* **1998**, *120*, 4502-4513.

1.44) Schonenberger, C.; Jorritsima, J.; Sondag-Huethorst, J. A. M.; Fokkink, L. G. J. *J. phys. Chem.* **1995**, *99*, 3259-3271.

1.45) Sellers, H.; Ulman, A.; Shnidman, Y.; Eilers, J. E. *J. Am. Chem. Soc.* **1993**, *115*, 9389-9401.

1.46) Shi, J.; Hong, B.; Parokh, A. N.; Collins, R. W.; Allara, D. L. *Chem. Phys. Lett.* **1995**, *246*, 90-94.

1.47) Sung, M. M.; Sung, K.; Kim, C. G.; Lee, S. S.; Kim, Y. *J. Phys. Chem. B* **2000**, *104*, 2273-2277.

1.48) Tamada, K.; Nagasawa, J.; Nakanishi, F.; Abe, K.; Hara, M.; Knoll, W.; Ishida, T.; Fukushima, H.; Miyashita, S.; Usui, T.; Koini, T.; Lee, T. R. *Thin Solid Films* **1998**, *327-329*, 150-155.

1.49) Tarlov, M. J.; Burgess, D. R. F.; Gillen, G. *J. Am. Chem. Soc.* **1993**, *115*, 5305-5306.

1.50) Tokuhisa, H.; Zhao, M.; Baker, L. A.; Phan, V. T.; Dermody, D. L.; Garcia, M. E.; Peez, R. F.; Crooks, R. M.; Mayer, T. M. *J. Am. Chem. Soc.* **1998**, *120*, 4492-4501.

1.51) van Patten, P. G.; Noll, J. D.; Myrick, M. L. *J. Phys. Chem. B* **1997**, *101*, 7874-7875.

1.52) Widrig, C. A.; Alves, C. A.; Porter, M. D. *J. Am. Chem. Soc.* **1991**, *113*, 2805-2810.

1.53) Willicut, R. J.; McCarley, R. L. *J. Am. Chem. Soc.* **1994**, *116*, 10823-10824.

1.54) Willicut, R. J.; McCarley, R. L. *Anal. Chim. Acta* **1995**, *307*, 269-276.

1.55) Xu, S.; Cruchon-Dupeyrat, S. J. N.; Garno, J. C.; Liu, G.-Y.; Jennings, G. K.; Yong, T.-H.; Laibinis, P. E. *J. Chem. Phys.* **1998**, *108*, 5002-5012.

1.56) Yan, C.; Golzhauser, A.; Grunze, M. *Langmuir* **1999**, *15*, 2414-2419.

1.57) Zamborini, F. P.; Crooks, R. M. *Langmuir* **1997**, *13*, 122-126.

1.58) Zerulla, D.; Mayer, D.; Hallmeir, K. H.; Chasse, T. *Chem. Phys. Lett.* **1999**, *311*, 8-12.

1.59) Zhang, Y.; Zhang, Y.; Terril, R. H.; Bohn, P. W. *Thin Solid Films* **1998**, *335*, 178-185.

1.60) Zhang, Q.; Huang, H.; He, H.; Chen, H.; Shao, H.; Liu, Z. *Surf. Sci.* **1999**, *440*, 142-150.

1.61) Zhao, X.-M.; Wilbur, J. L.; Whitesides, G. M. *Langmuir* **1996**, *12*, 3257-3264.

1.62) Zharnikov, M.; Frey, S.; Heister, K.; Grunze, M. *Langmuir* **2000**, *16*, 2697-2705.

1.63) Zubragel, C.; Schneider, F.; Neumann, M.; Hahner, G.; Woll, C.; Grunze, M. *Chem. Phys. Lett.* **1994**, *219*, 127-131.

1.64) Bain, C. D.; Whitesides, G. M. *Science* **1988**, *240*, 62.

1.65) Bain, C. D.; Troughton, E. B.; Tao, Y. T.; Evall, J.; Whitesides, G. M.; Nuzzo, R. G. *Journal of the American Chemical Society* **1989**, *111*, 321-335.

1.66) Bain, C. D.; Whitesides, G. M. *J. Am. Chem. Soc.* **1989**, *111*, 7155.

1.67) Bain, C. D.; Whitesides, G. M. *J. Am. Chem. Soc.* **1989**, *111*, 7164.

1.68) Shon, Y.-S.; Colorado Jr, R.; Williams, C. T.; Bain, C. D.; Lee, T. R. *Langmuir* **2000**, *16*, 541-548.

1.69) Fenter, P.; Eisenberger, P.; Li, J.; Camillone III, N.; Bernasek, S.; Scoles, G.; Ramanarayaman, T. A.; Liang, K. S. *7* **1991**.

1.70) Fenter, P.; Eisenberger, P.; Liang, K. S. *Phys. Rev. Lett.* **1993**, *70*, 2447-2450.

1.71) Fenter, P.; Eberhardt, A.; Eisenberger, P. *Science* **1994**, *266*, 1216-1218.

1.72) Fenter, P.; Schreiber, F.; Berman, L.; Scoles, G.; Eisenberger, M. J.; Bedzyck, M. *Surf. Sci.* **1998**, *412/413*, 213.

1.73) Ishida, T.; Yamamoto, S.; Mizutani, W.; Motomatsu, M.; Tokumoto, H.; Hokari, H.; Azehara, H.; Fujihira, M. *Langmuir* **1997**, *13*, 3261-3265.

1.74) Liu, G.-Y.; Fenter, P.; Chidsey, C. E.; Ogletree, D. F.; Eisenberger, P.; Salmeron, M. *J. Chem. Phys.* **1994**, *101*, 4301-4306.

1.75) Dubois, L. H.; Nuzzo, R. G. *Ann. Rev. Phys. Chem.* **1992**, *43*, 437-463.

1.76) Dubois, L. H.; Zegarski, B. R.; Nuzzo, R. G. *J. Chem. Phys.* **1993**, *98*, 678-688.

1.77) Laibinis, P. E.; Whitesides, G. M.; Allara, D. L.; Tao, Y.-T.; Parikh, A. N.; Nuzzo, R. G. *J. Am. Chem. Soc.* **1991**, *113*, 7152.

1.78) Nuzzo, R. G.; Zegarski, B. R.; Dubois, L. H. *J. Am. Chem. Soc.* **1987**, *109*, 733-740.

1.79) Peterlinz, K. A.; Georgiadis, R. M.; Herne, T. M.; Tarlov, M. J. *J. Am. Chem. Soc.* **1997**, *119*, 3401-3402.

1.80) Ulman, A. *Chem. Rev.* **1996**, *96*, 1533-1554.

1.81) Creager, S. E. *J. Phys. Chem.* **1992**, *96*, 2371-2375.

1.82) Poirier, G. E. *Chem. Rev.* **1997**, *97*, 1117-1127.

1.83)Ulman, A. *An introduction to ultrathin organic films* Boston, MA, 1991.

1.84) Poirier, G. E.; Herne, T. M.; Miller, C. C.; Tarlov, M. J. *J. Am. Chem. Soc.* **1999**, *121*, 9703-9711.

1.85) Poirier, G. E. *Langmuir* **1999**, *15*, 1167-1175.

1.86) Loepp, G.; Vollmer, S.; Witte, G.; Woll, C. *Langmuir* **1999**, *15*, 3767-3772.

1.87) Arce, F. T.; Vela, M. E.; Salvarezza, R. C.; Arvia, A. J. *J. Chem. Phys.* **1998**, *109*, 5703-5706.

1.88) Noy A., F. C. D., Rozsnyai L. F., Wrighton M. S., Lieber C. M. *J. Am. Chem. Soc.* **1995**, *117*, 7943-7951.

1.89) Dunaway, D. J.; McCarley, R. L. *Langmuir* **1994**, *10*, 3598-3606.

1.90) Zhong, C.-J.; Brush, R. C.; Anderegg, J.; Porter, M. D. *Langmuir* **1999**, *15*, 518-525.

1.91) Wirde, M., Gelius U., Allara D. L., *Nucl. Instr. Meth. B* **1997**, 131(1-4), 245-251.

1.92) Beulen, M. W. J.; Huisman, B.-H.; van der Heijden, P. A.; van Veggel, F. C. J. M.; Simons, M. G.; Biemond, E. M. E. F.; de Lange, P. J.; Reinhoudt, D. N. *Langmuir* **1996**, *12*, 6170-6172.

1.93) Hutt, D. A.; Cooper, E.; Legget, G. J. *Surf. Sci.* **1998**, *397*, 154-163.

1.94) Rieley, H.; Price, N. J.; White, R. G.; Blyth, R. I. R.; Robinson, A. W. *Surf. Sci.* **1995**, *331-333*, 189-195.

1.95) Outka, D. A.; Stohr, J.; Rabo, J. P.; Swalen, J. D. *J. Chem. Phys.* **1988**, *88*, 4076-4087.

1.96) Zharnikov, M.; Frey, S.; Rong, H.; Yang, Y.-J.; Heister, K.; Buck, M.; Grunze, M. *Phys. Chem. Chem. Phys.* **2000**, *2*, 3359-3362.

1.97) Fernandez, A.; Espinos, J. P.; Gonzalez-Elipe, A. R.; Kerkar, M.; Thompson, P. B. J.; Ludecke, J.; Scragg, G.; de Carvalho, A. V.; Woodruff, D. P.; Fernandez-Garcia, M.; Conesa, J. C. *J. Phys.:Condens. Matter* **1995**, *7*, 7781-7796.

1.98) Hayes, W. A.; Kim, H.; Yue, X.; Perry, S. S.; Shannon, C. *Langmuir* **1997**, *13*, 2511-2518.

1.99) Chailapakul, O.; Crooks, R. M. *Langmuir* **1995**, *11*, 1329.

1.100) Overney, R. M.; Meyer, E.; Frommer, J.; Brodbeck, D.; Luthi, R.; Howald, L.; Guntherodt, H.-J.; Fujihira, M.; Takano, H.; Gotoh, Y. *Nature* **1992**, *359*, 133-135.

1.101) Frisbie, C. D.; Rozsnyai, L. F.; Noy, A.; Wrighton, M. S.; Lieber, C. M. *Science* **1994**, *265*, 2071-2074.

1.102) Hayes, W. A.; Shannon, C. *Langmuir* **1996**, *12*, 3688-3694.

1.103) Hobara, D.; Ota, M.; Imabayashi, S.-I.; Niki, K.; Kakiuchi, T. *J. Elec. Anal. Chem.* **1998**, *444*, 113-119.

1.104) Willicut, R. J.; McCarley, R. L. *Adv. Mater.* **1995**, *7*, 759-762.

1.105) Narayanan, V. V.; Newkome, G. R. *Topics. Curr. Chem.* **1998**, *197*, 19-77.

1.106) Bosman, A. W.; Janssen, H. M.; Meijer, E. W. *Chem. Rev.* **1999**, *99*, 1665-1688.

1.107) Tomalia, D. A.; Hurst, H. D. *Topics in Current Chemistry* **1993**, *165*, 193-313.

1.108) Zeng, F.; Zimmerman, S. C. *Chem. Rev.* **1997**, *97*, 1681-1712.

1.109) Fischer, M.; Vögtle, F. *Angew. Chem. Int. Ed.* **1999**, *38*, 885-905.

1.110) Liu, M.; Kono, K.; Fréchet, J. M. J. *J. Control. Release* **2000**, *65*, 121-131.

1.111) Freemantle, M. *C&EN London* **1999**, *November 1, 1999*, 27-35.

1.112) Reetz, M. T.; Lohmer, G.; Schwickardi, R. *Angew. Chem. Int. Ed. Engl.* **1997**, *36*, 1526-1529.

1.113) Knapen, J. W. J.; van der Made, A. W.; de Wilde, J. C.; van Leeuwen, P. W. N. M.; Wijkens, P.; Grove, D. M.; van Koten, G. *Nature* **1994**, *372*, 659-663.

1.114) Balzani, V.; Campagna, S.; Denti, G.; Juris, A.; Serroni, S.; Venturi, M. *Acc. Chem. Res.* **1998**, *31*, 26-34.

1.115) Kovvali, A. S.; Chen, H.; Sirkar, K. K. *J. Am. Chem. Soc.* **2000**, *122*, 7594-7595.

1.116) Balogh, L.; Valluzi, R.; Laverdure, K. S.; Gido, S. P.; Hagnauer, G. L.; Tomalia, D. A. *J. Nanopart. Res.* **1999**, *1*, 353-368.

1.117) Grohn, F.; Bauer, B. J.; Akpalu, Y. A.; Jackson, C. L.; Amis, E. J. *Macromol.* **2000**, *33*, 6042-6050.

1.118) Esumi, K.; Suzuki, A.; Yamahira, A.; Torigoe, K. *Langmuir* **2000**, *16*, 2604-2608.

1.119) He, J.-A.; Valluzzi, R.; Yang, K.; Dolukhanyan, T.; Sung, C.; Kumar, J.; Tripathy, S. K. *Chem. Mater.* **1999**, *11*, 3268-3274.

1.120) Diallo, M. S.; Balogh, L.; Shafagati, A.; Johnson, J. H.; Goddard III, W. A.; Tomalia, D. A. *Env. Sci. Technol.* **1999**, *33*, 820-824.

1.121) Zhao, M.; Crooks, R. M. *Chem. mater.* **1999**, *11*, 3379-3385.

1.122) Ottaviani, M. F.; Bossmann, S.; Turro, N. J.; Tomalia, D. A. *J. Am. Chem. Soc.* **1994**, *116*, 661-671.

1.123) Ottaviani, M. F.; Montalti, F.; Turro, N. J.; Tomalia, D. A. *J. Phys. Chem. B* **1997**, *101*, 158-166.

1.124) Zhao, M. Q.; Sun, L.; Crooks, R. M. *J. Am. Chem. Soc.* **1998**, *120*, 4877-4878.

1.125) Balogh, L.; Tomalia, D. A. *J. Am. Chem. Soc.* **1998**, *120*, 7355-7356.

1.126) Liao, Y.-H.; Moss, J. R. *Organometallics* **1996**, *15*, 4307-4316.

1.127) Zhao, M.; Crooks, R. M. *Angew. Chem. Int. Ed.* **1999**, *38*, 364-366.

1.128) Bardaji, M.; Kustos, M.; Caminade, A.-M.; Majoral, J.-P.; Chaudret, B. *Organometallics* **1997**, *16*, 403-410.

1.129) Chechik, V.; Crooks, R. M. *J. Am. Chem. Soc.* **2000**, *122*, 1243-1244.

1.130) Bosman, A. W.; Schenning, A. P. H. J.; Janssen, R. A. J.; Meijer, E. W. *Chem. Ber./Recueil* **1997**, *130*, 725-728.

1.131) Vassilev, K.; Ford, W. T. *J. Polymer Sci. Part A.* **1999**, *37*, 2727-2736.

1.132) Montano, P. A.; Shenoy, G. K.; Alp, E. E.; Shulze, W.; Urban, J. *Phys. Rev. Letters* **1986**, *56*, 2076-2079.

1.133) Apai, G.; Hamilton, J. F.; Stöhr, J.; Thompson, A. *Phys. Rev. Letters* **1979**, *43*, 165-169.

1.134) Borowski, M. *J. Phys. IV France 7* **1997**, *C2*, 259-260.

1.135) Hierlemann, A.; Campbell, J. K.; Baker, L. A.; Crooks, R. M.; Ricco, A. J. *J. Am. Chem. Soc.* **1998**, *120*, 5323-5324.

1.136) Li, J.; Swanson, D. R.; Qin, D.; Brothers, H. M.; Piehler, L. T.; Tomalia, D.; Meier, D. J. *Langmuir* **1999**, *15*, 7347-7350.

1.137) Lackowski, W. M.; Campbell, J. K.; Edwards, G.; Chechik, V.; Crooks, R. M. *Langmuir* **1999**, *15*, 7632-7638.

1.138) Miksa, B.; Slomkowski, S.; Chehimi, M. M.; Delamar, M.; Majoral, J.-P.; Caminade, A.-M. *Colloid. Polym. Sci.* **1999**, *277*, 58-65.

1.139) Tsukruk, V. V.; Rinderspacher, F.; Bliznyuk, V. N. *Langmuir* **1997**, *13*, 2171-2176.

Chapter 2. Materials and Methods

2.1. Experimental

2.1.1. Chemicals

2.1.1.1. Preparation of Alkanethiol SAMs

Au (111) films were obtained by thermal evaporation of Au (Aldrich, 99.99 % purity) onto freshly cleaved muscovite mica sheets (V-2 grade, Asheville-Schoonmaker) or Si(100) wafers. Films of Ag and Cu were prepared by thermally evaporating Ag (Aldrich, 99.99 % purity) and Cu (Aldrich, 99.99 % purity), respectively, onto a Si(100) wafer. The Si wafers were cleaned in a piranha solution (1 to 3 ratio of H_2O_2 to H_2SO_4 at 70 °C for at least 30 minutes handled with extreme caution) and then placed under vacuum for evaporation. When using Si wafers, an adhesion layer of ~ 40 Å of Cr was deposited onto the freshly cleaned substrate prior to metal deposition. After evaporation, the samples were annealed at 325 °C for at least 4 hours. The annealing procedure leads to the formation of larger and flatter gold crystallites.[1,2] The typical size of the obtained gold crystallites is comprised between 150 and 300 nm. The preferred orientation of the crystallites has been shown to be predominantly (111).[1] The evaporated substrates were cooled to room temperature and immersed in a 1 mM ethanolic solution of the desired alkanethiol. Table 1 lists some of the chemical and physical properties of the alkanethiols used in this work.

2.1.1.2. Preparation of Mixed SAMs

The synthesis of the ω-(N-pyrrolyl) hexanethiol is described elsewhere.[3] We acknowledge Dr L. S. Curtin at Youngstown State University (Youngstown, OH) for the kind gift of the ferrocenoyl alkanethiol. The structures of these two functionalized thiols are shown in Figure 2.1.

Table 2.1. Physical and chemical properties of alkanethiols used in this study.

Molecular Formula	Name	Synonym	Molecular Weight ($g \times mol^{-1}$)	Purity	Density ($g \times cm^{-3}$)	Boiling Point (°C)
$C_5H_{12}S$	1-pentanethiol	amyl mercaptan	104.22	98%	0.840	126
$C_6H_{14}S$	1-hexanethiol	hexyl mercaptan	118.24	95%	0.838	150 to 154
$C_{10}H_{22}S$	1-decanethiol	decyl mercaptan	174.35	96%	0.841	114
$C_{12}H_{26}S$	1-dodecanethiol	*n*-dodecyl mercaptan	202.40	98+%	0.845	266 to 283
$C_{14}H_{30}S$	1-tetradecanethiol	n-tetradecyl mercaptan	230.46	98.0%	0.846	
$C_{16}H_{34}S$	1-hexadecanethiol	cetyl mercaptan or hexadecyl mercaptan	258.51	~95%	0.846	128–130
$C_{18}H_{38}S$	1-octadecanethiol	octadecyl mercaptan	286.57	98%	0.847	204 to 210

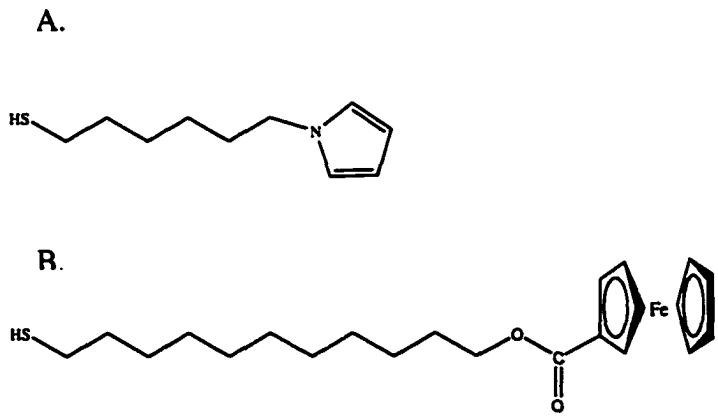

Figure 2.1. A. Structure of the ω-(N-pyrrolyl) hexanethiol. B. Structure of the 11-ferrocenoyl-undecane-1-thiol.

2.1.1.3. Preparation of the DAB-Am_n-$Cu(II)_x$ Complexes and DAB-Am_n-$Cu(0)_{cluster}$ Nanoparticles

The DAB-Am_n-$Cu(II)_x$ (n=4, 8, 16, 32, 64,x=n/2) complexes were all synthesized in the same manner. All chemicals were used as received from Aldrich. The requisite amounts of methanolic solutions of $Cu(NO_3)_2 \cdot 2.5\ H_2O$ and the corresponding amine-terminated poly(propylene imine) dendrimer with a diaminobutyl core (DAB-Am_n (n=4, 8, 16, 32, 64)) were mixed in order to result in a final Cu(II) concentration of 2 mM. The faint blue $Cu(NO_3)_2$ solution turned to an intense blue upon mixing with the dendrimer solution. The solution was stirred for 30 min. The concentration in dendrimer was 1 mM DAB-Am_4-$Cu(II)_2$, 0.5 mM DAB-Am_8-$Cu(II)_4$, 0.25 mM DAB-Am_{16}-$Cu(II)_8$, 0.125 mM DAB-Am_{32}-$Cu(II)_{16}$, 0.0625 mM DAB-Am_{64}-$Cu(II)_{32}$ for generation 1, 2, 3, 4, and 5 respectively when maintaining a Cu(II) concentration of 2 mM throughout the series of dendrimer generations. Cu nanoparticles were formed by reduction of the DAB-Am_n-$Cu(II)_x$ solutions with a 10 fold excess of $NaBH_4$.[4] The reduction resulted in a color change of the solution from blue to golden brown, which indicated the formation of the nanoclusters DAB-Am_n-$Cu(0)_{cluster}$. TEM samples of DAB-Am_n-$Cu(0)_{cluster}$ were obtained by placing a drop of the solution on a holey-carbon copper grid, and immediately transferred into vacuum. The DAB-Am_n-$Cu(0)_{cluster}$ samples for EXAFS and XANES were prepared by reduction of the DAB-Am_n-$Cu(II)_x$ solutions. As long as these reduced solution of Cu/dendrimer were kept under inert atmosphere, no precipitate or change of color was observed. Powders were obtained by rotary evaporation of the solvent. The resulting powders were transferred under Ar into an oxygen-free glove box where they were placed between layers of kapton tape. The resulting tape/powder samples were kept in an oxygen-free environment for all analysis.

2.1.1.4. Preparation of the Ferrocene-Terminated Dendrimers

The synthesis of the ferrocenyl dendrimers was based on the procedure described by Takada et al.[5] Briefly, a solution of the poly(propylene imine) dendrimer (DAB-Am$_n$, n=4, 8, 16, 32, and 64) and triethylamine in dichloromethane was added to a dichloromethane solution of the corresponding equivalents of 1-chlorocarbonylferrocene. The triethylamine hydrochloride formed was removed by washing with $NaHCO_3$, and the solution dried over $MgSO_4$. The resulting product obtained for x=32 is shown in Figure 1.7.

2.1.2. Scanning Probe Microscopy (SPM)

2.1.2.1. Scanning Tunneling Microscopy (STM)

The STM used was a Digital Instruments Nanoscope III[6] using one of two available scanners depending on the desired resolution. The piezoelectric scanners were 0.8 μm × 0.8 μm (A head), and 13 μm × 13 μm (D head). The scanning apparatus was suspended on a homemade support with a resonance frequency of about 1 Hz, which keeps vibrations from perturbing image acquisition. The tip was freshly cleaved from a Pt-Ir wire. All images were collected in air on freshly prepared substrates.

2.1.2.2. Atomic Force Microscopy (AFM) and Lateral Force Microscopy (LFM)

AFM and LFM were performed with the same Digital Instruments Nanoscope III microscope using the multi-mode head. We used contact AFM pyramidal gold cantilevers with a silicon nitride (Si_3N_4) tip (≈ 30 nm tip diameter) purchased from Digital Instruments. The calibration of the instrument was achieved through procedures described elsewhere.[7]

2.1.3. Synchrotron Radiation Experiments.

EXAFS experiments on alkanethiols described in chapter 4 were performed at the Synchrotron Light group (SYLI) at the Electron Stretcher Accelerator (ELSA) in Bonn, Germany (Physikalisches Institut der Rheinischen Friedrich-Wilhelms-Universität). The EXAFS experiments were carried out on the BN2 double crystal monochromator (DCM) beamline with the machine operating at 2.3 GeV providing an average ring current of 25 – 70 mA. XANES experiments as well as EXAFS experiments described in Chapter 5 and 6 were carried out at the Center for Advanced Microstructures and Devices (CAMD) in Baton Rouge, Louisiana (U.S.A.). Sulfur K-edge XANES experiments were performed with the ring operating at 1.3 GeV, with an average ring current of about 140 mA. Copper K-edge EXAFS spectra were measured with the synchrotron operating at 1.5 GeV with an average ring current of about 100 mA. Sulfur K-edge XANES spectra were acquired at the X-ray Microprobe Beamline (XMP), which is described in section 2.1.3.3. Sulfur K-edge, iron K-edge measurements were performed at the BN2-DCM beamline described in section 2.1.3.2. More details concerning the crystal pair mounted in the monochromator will be given within each separate experiment.

2.1.3.1. The Double Monochromator Beamline (DCM) at CAMD

This beamline was installed at bending magnet 5 port B on the CAMD storage ring in 1994 and its design and operation has been described by Schilling et al.[8] The beamline set-up is represented in Figure 2.2. The UHV system, including a Bremsstrahlung shutter, a fast closing shutter and a 1.8 m acoustic delay line is separated from the monochromator by a differential ion pump, which now replaces the initial Be window. The vacuum section in which the monochromator is operated, is

separated from the experimental station by a 50 μm-thick kapton window. The monochromator is a Lemonnier-type monochromator which was built at Bonn university (Germany) and its design can be found in the literature.[9]

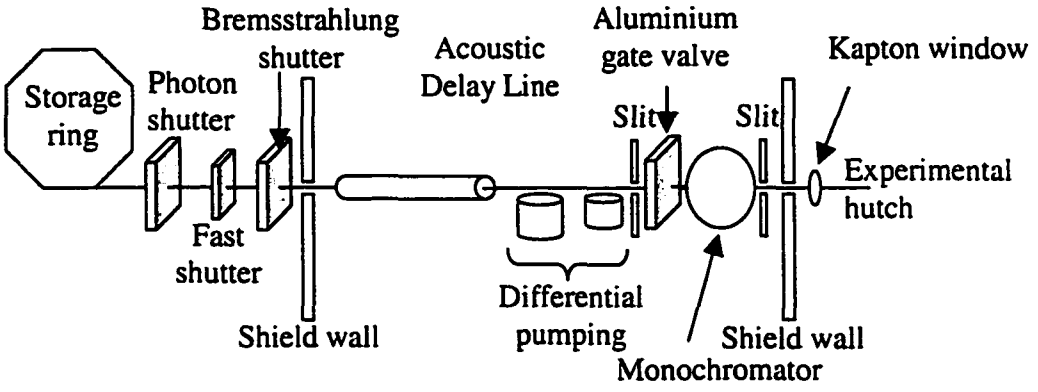

Figure 2.2. Cartoon depicting the Double Crystal Monochromator (DCM) beamline at CAMD.

Horizontal and vertical slits are placed on both sides of the monochromator and allow for control over the horizontal acceptance from 0 to 50 mm and vertical opening from 0 to 10 mm. The operation of the DCM beamline at CAMD provides usable flux over a broad range of energies (0.8 keV to 18 keV) to be realized.

2.1.3.2. The BN2 Beamline at ELSA

The design of the BN2 double crystal monochromator at ELSA is very similar to that of the DCM at CAMD and allows for conventional transmission and fluorescence experiments to be realized. However, the endstation was optimized for surface EXAFS experiments allowing the acquisition of EXAFS spectra taken at grazing incidence or (up to 0.05°). The grazing incidence EXAFS experimental set-up or GIXAFS is shown in figure 2.3.

Sulfur K-edge and iron K-edge measurements were performed at the BN2-DCM beamline. The fluorescence yield was measured by a single element Si(Li) detector described in section 2.1.5.4. The monochromator was calibrated with the strong sulfur

peak of $ZnSO_4$ at 2481.44 eV. A 7.5 μm iron foil ($E_0 \approx 7112$ eV) was used for calibration at the iron K-edge. A multi-channel analyzer (MCA) was used to discriminate against the gold fluorescence for the samples on Au substrates, or to window the sulfur signal when copper and silver substrates were used.

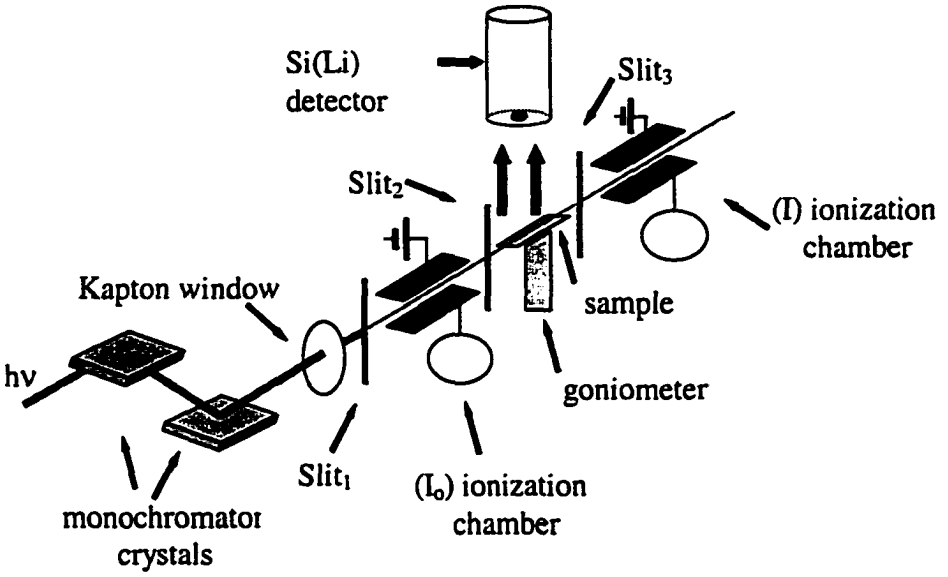

Figure 2.3. Schematic of the BN2 double crystal monochromator grazing incidence beamline (DCM) at ELSA.

The detector was calibrated using radioactive ^{55}Fe. InSb(111) crystals were used for XAFS studies at the sulfur K-edge and Ge(422) crystals were used for experiments at the iron K-edge. The alignment procedure was achieved with the sample out of the beam path, by optimizing the current in ionization chambers I_0 and I. This was realized by adjusting slits 1 to 3 in Figure 2.3. The sample was then tilted to an angle of 0.2° and moved back up into the beam path, until the current in ionization chamber I was found to decrease. The angle was then reduced by 0.02° increments and the sample was lifted again into the beam path. This procedure was repeated until 0° angle was reached. The position of the true 0° angle was validated when rotation of the sample in either direction (pitch) resulted in a decrease of I. Further verification of the

0° angle was also achieved by applying the following procedure: The angle between the beam and the sample surface was set to a chosen value θ. Slit 3 was vertically scanned in order to find the height h_{slit3} that led to a maximum intensity of I. The distance between the sample and slit 3 being known, the equation $h_{slit3} = d \times \tan(\theta)$ permits to verify if the alignment was properly realized. The goniometer also allowed for yaw and roll motions. The roll motion was limited by the sample geometry, and was not typically optimized. The yaw was optimized following the same procedure as for the pitch angle. The grazing incidence angle was optimized by monitoring the intensity of the sulfur fluorescence Kα peak at 2307 eV while varying the incidence angle. The discrimination window of the MCA was defined such that the signal from sulfur was maximized while the contribution from the metallic substrate was minimized. The incidence angle was chosen to be 0.4° with respect to the surface for silver and copper substrate samples.

Due to the strong gold fluorescence, it was not possible to collect data at the same incidence angle for the gold substrate samples. The range of incident angles was much narrower than for silver and copper due to the overlap between the sulfur signal and the gold fluorescence. Typically, we acquired data for gold between 0.01° and 0.05° incidence angle. The quality of the data was extremely sensitive to a change of only 0.005°. Each spectrum except for the gold data is an average of at least five separate scans, with an integration time of at least 3 seconds per data point. The current read in the I_0 chamber was used to normalize the fluorescence counts.

2.1.3.3. The X-ray Microprobe (XMP) Beamline at CAMD

The XMP beamline is similar to that of the original DCM beamline.[10] This beamline shares the dipole chamber used by the DCM beamline and operates on port

5A. In addition to its capacity of performing X-ray microscopy, the XMP beamline was also designed for EXAFS and XANES measurements. A schematic of the XMP beamline is shown in figure 2.4.

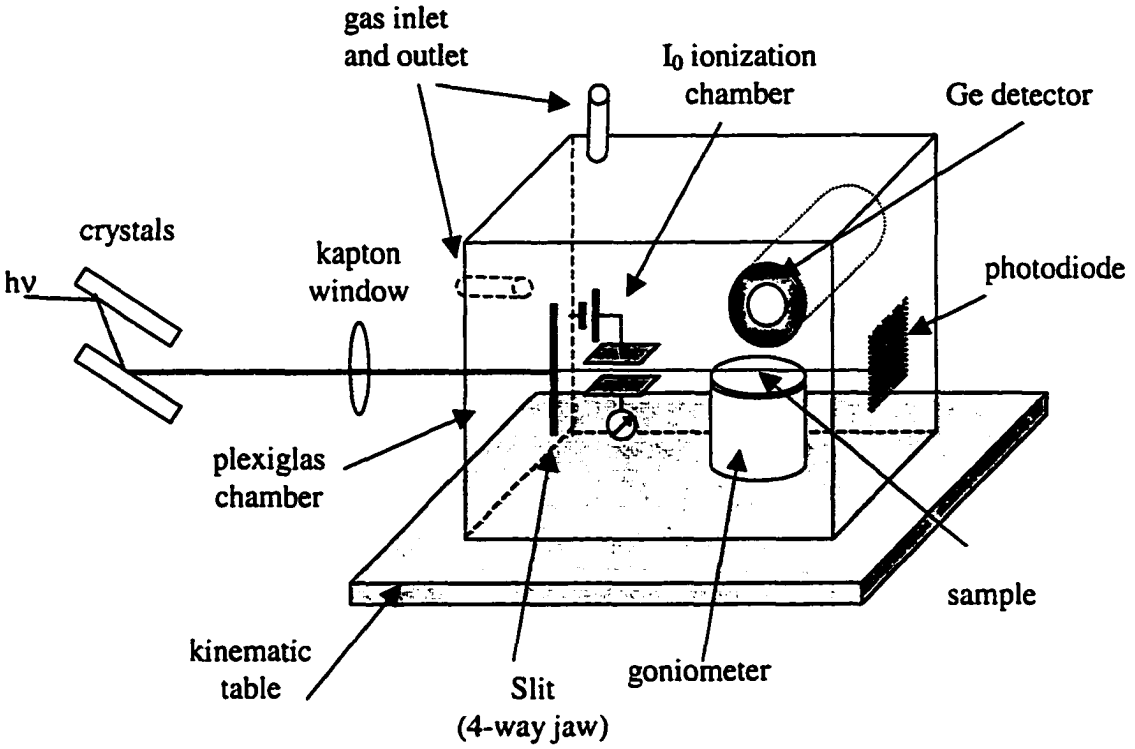

Figure 2.4. Schematic of the end-station at the X-ray Microprobe (XMP) beamline at CAMD

The UHV section, including the photon shutter, gate valve, fast closing valve, and bremsstrahlung shutter, is separated from the experimental station by a 125 μm-thick Be window. An additional kapton window, 50 μm or 12.5 μm-thick depending on the energy range at wich the study is conducted, allows the endstation to operate at atmospheric pressure. The beamline relies on a modified double crystal monochromator designed by the Laboratório Nacional de Luz Síncrotron (LNLS, Campinas, Brazil).[8] The microprobe end-station consists of a kinematic table, a plexiglas chamber, and a goniometer. The kinematic table allows for vertical motion of the entire end-station. The enclosed chamber containing the stages allows for air

absorption to be minimized by purging with He, or other appropriate gases depending on the energy range of the investigation. Finally, the motorized stages permit vertical, horizontal, pitch and yaw motions of the sample. The fluorescence Ge detector (Canberra, model GUL01110P[11]) with a resolution of 150 eV (FWHM) at 5895 eV (Mn Kα) is placed at 90 ° from the beam direction and positioned on a *xyz* translation stage. Alignment of the beam was realized by vertically adjusting the entrance slits and monitoring the intensity at a photodiode. Alignment of the sample was achieved by the procedure described in section 2.1.3.2. for the GIXAFS experiment.

2.1.4. Synchrotron Radiation

When high-energy electrons (up to several GeV) are accelerated along a circular orbit, the presence of bending magnets induces a strong centripetal acceleration which results in the production of electromagnetic waves also known as synchrotron radiation.[12,13] The electrons are injected at a relatively low kinetic energy (on the order of 100 MeV) by a linear accelerator and introduced and accelerated in the synchrotron. The ring consists of an arrangement of bending and focusing magnets and straight sections.[14] Synchrotron radiation has become a powerful tool for spectroscopists due to properties summarized by Koch[13,15] that are listed below :

- Synchrotron radiation covers a broad range of the electromagnetic spectrum from microwave to the hard X-ray and γ-ray regions
- Synchrotron radiation offers a much higher intensity than conventional X-ray sources (on the order of 10^6 times superior)
- High degree of collimation which associated with the small cross section of the electrons leads to high brilliance of the source

- The radiation is linearly polarized in the plane of the electron orbit. Off the orbital plane, the polarization is elliptically polarized
- Pulsed emission of the electrons which travel in bunches with a pulse duration as short as 50 ps
- Clean environment in ultra high vacuum

The advent of synchrotron radiation tremendously contributed to the development of EXAFS and XANES spectroscopies, due to the outstanding properties of synchrotron radiation over conventional X-ray sources, namely X-ray tubes and rotating anodes.

2.1.5. X-ray Absorption Fine Structure (XAFS)

The interaction of photons with matter results in the absorption of all or part of the energy of the incident beam to the material which undergoes different processes of rearrangement of its electronic structure. These processes are scattering, pair production or photoelectric absorption. In absorption, the loss of intensity of the incident beam is proportional to the initial intensity I_0 and the thickness x of the sample and is given by the relationship :

$$dI = -\mu \times I dx \qquad (2.1)$$

where μ is the linear absorption coefficient. Integration of equation 2.1 leads to:

$$I = I_0 \times e^{-\mu x} \qquad (2.2)$$

The linear absorption coefficient is sometimes substituted for the mass absorption coefficient (μ_a) which is obtained by dividing μ by the density (ρ) of the material. The mass absorption coefficient of a mixture can be approximated by a linear combination of the mass absorption coefficients of the individual constituents.[12] μ_a is expressed in cm^2/g. As the energy of the incident photon is increased, there is a

smooth decrease in the absorption coefficient which is accompanied by a sudden increase when the energy reaches a critical value corresponding to the binding energy of the electron. Such a discontinuity in the spectrum is called an absorption edge. An absorption edge corresponds to the ejection of an electron from an inner shell of the atom to the continuum. Electrons in an atom are distributed in a succession of shells, K, L, M, N, etc..., which are labeled in order of decreasing energy. The edge energies are specific for each element and tabulated (Appendix I). The work in this dissertation is concerned with EXAFS and XANES studies of sulfur, copper, and iron at the K-edge and corresponds to monitoring the absorption coefficient when an electron is ejected from the inner-most shell of the atom, i.e., the K shell.

When an atom is isolated, the spectrum consists of the absorption edge and a smooth decrease of the absorption coefficient. For molecules or clusters, a fine structure, small amplitude oscillations superimposed on the decreasing absorption coefficient called EXAFS can be seen following the absorption edge. The fine structure might extend up to 1000 eV after the edge. The extended fine structure has been observed by Kronig as early as 1931,[16] but its use to determine structural parameters was not exploited until the work of Stern, Lytle, and Sayers in the early 1970s.[17-20] The origin of the EXAFS oscillations is illustrated in figure 2.5.

The EXAFS wiggles correspond to the interaction between the ejected photoelectron wave and that part of it that is backscattered with constructive and destructive interference by the neighboring atoms. The EXAFS region extends from about 50 eV after the edge to about 1000 eV in some cases and contains information about the environment of the central absorber atom. EXAFS allows determinations of bond distances, coordination numbers and the chemical identity of the neighbor atoms.

The low energy region of the spectrum containing the pre-edge and the near-edge, which extends from 20 eV before the edge to about 50 eV after the edge, contains information about the chemical state of the absorber atom such as its oxidation state and is called Near-Edge X-ray Absorption Fine Structure (NEXAFS) or most commonly X-ray Absorption Near-Edge Structure (XANES).

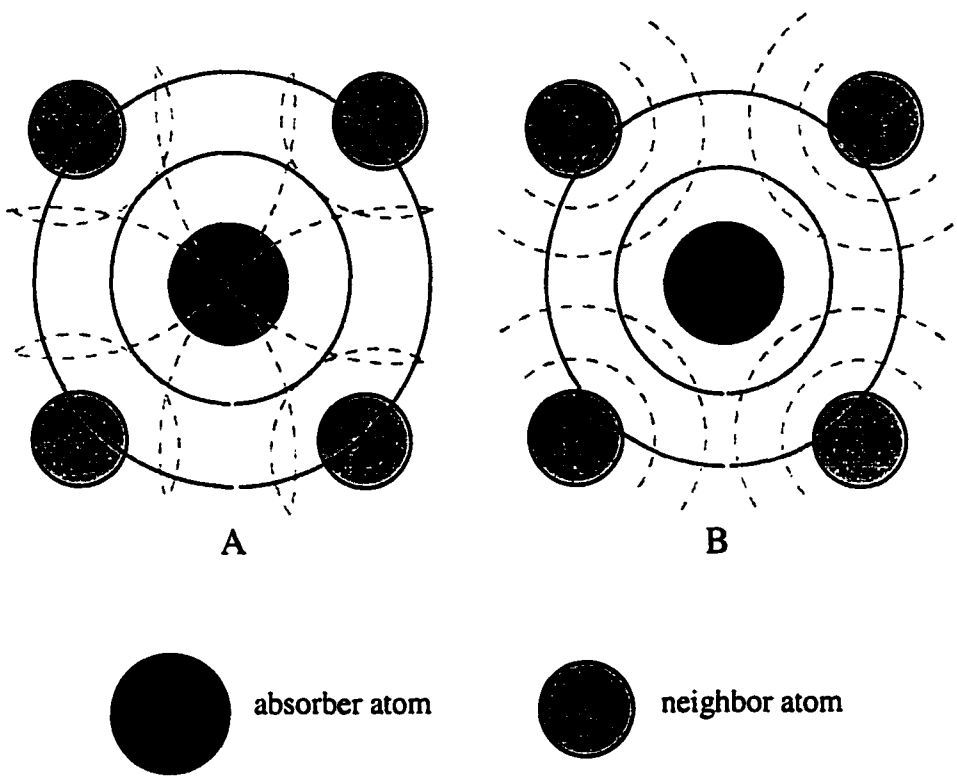

Figure 2.5. The outgoing photelectron wave meets the backscattered wave resulting in constructive interference in A and destructive interference in B.

Multiple-scattering is responsible for intense maxima in the XANES region, whereas a single-scattering theory can be used to model the weak maxima that result in the EXAFS region. The two regions are shown in figure 2.6.

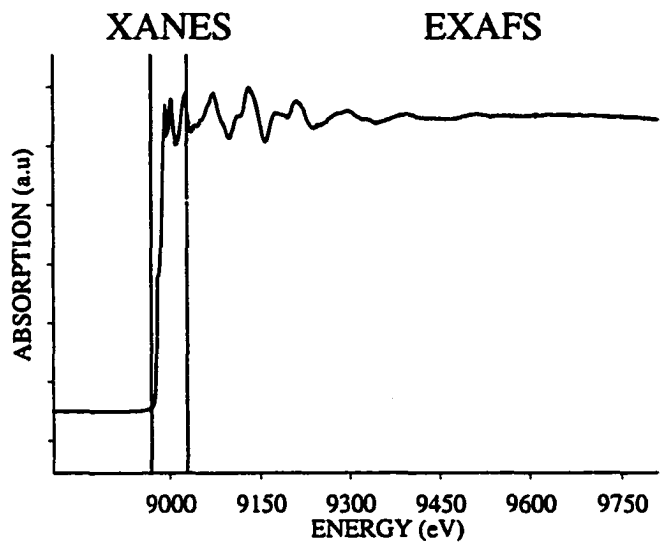

Figure 2.6. X-Ray absorption spectrum of metallic copper, showing the XANES and EXAFS regions.

2.1.5.1. Theory of EXAFS

As a photoelectron is ejected from the core shell of the atom, the photoelectron wave vector k can be expressed as in equation (2.3), where E is the energy of the incident photon, E_0 is the binding energy of the atom for the given shell, m is the mass of the photoelectron, $\hbar$ is the reduced Planck constant ($\hbar$=h / 2π).

$$k = \sqrt{\frac{2m}{\hbar^2} \times (E - E_0)} \qquad (2.3)$$

The photoelectron is backscattered by the neighboring atoms, which then generate a backscattering wave that can constructively or negatively interfere with the outgoing wave. By monitoring the variations in μ as a function of the energy, we obtain information on the nature and distances of the neighboring atoms from the absorber. The mathematical development of EXAFS is based on a short-range single-electron, single-scattering theory.[12,21,22] The variations in the absorption coefficient as a function of energy are given by equation (2.4) where $\mu_0(E)$ is the "background" absorption coefficient.

$$\chi(E)=\frac{\mu(E)-\mu_0(E)}{\mu_0(E)} \tag{2.4}$$

The structural information that is contained in the response of μ to the photoelectron wave vector k can be accessed by converting the expression of χ from energy space to k space by using equation (2.3). This results in an expression of χ as a function of k in equation (2.5).

$$\chi(k)=\frac{\mu(k)-\mu_0(k)}{\mu_0(k)} \tag{2.5}$$

The EXAFS function is given by equation (2.6).

$$\chi(k)=\sum_j N_j S_i(k) F_j(k) e^{-2\sigma_j^2 k^2} e^{-2r_j/\lambda_j(k)} \frac{\sin\left(2kr_j+\Phi_{ij}(k)\right)}{kr_j^2} \tag{2.6}$$

This expression represents the summation of the contributions of all the neighbors j to the central absorber atom i. N_j is the number of atoms of type j at a distance r_j from the absorber atom. $F_j(k)$ is the backscattering function from each of the N_j atoms. σ_j is the Debye-Waller factor and accounts for thermal and static disorder of the atoms N_j around their position. ϕ_{ij} (k) is the total phase shift of the photoelectron wave. The term $\exp(-r_j/\lambda_j)$, accounts for inelastic scattering, where λ_j is the mean free path of an electron. $S_i(k)$ is a scaling factor that accounts for many-body effects. N_j, r_j, and σ_j are the structural parameters whereas $F_j(k)$ and λ_j are scattering parameters. Data analysis (Appendix II) was performed using well-established procedures.[22]

2.1.5.2. Data Acquisition in the Transmission Mode

The simplest and most common way to acquire an absorption spectrum is to measure the intensity of the transmitted beam as a function of energy and normalize it to the intensity of the incident beam using equation (2.2). The intensities of the

transmitted and incident beam, I and I_0 respectively, are measured through the use of ionization chambers. The experimental set-up used for transmission is shown in Figure 2.7.

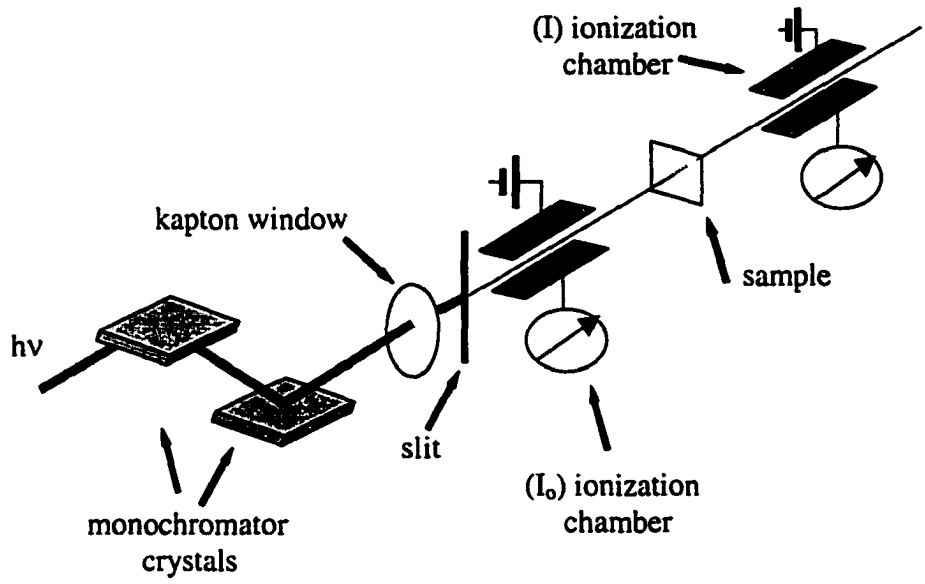

Figure 2.7. Schematic of the transmission experiment set-up.

2.1.5.3. Data Acquisition in the Fluorescence Mode

Frequently one wishes to measure the EXAFS or XANES spectrum of a sample that has a very dilute absorber, and in such cases the attenuation of the X-ray beam is minimal. Therefore, it is not possible to determine the absorption coefficient by measuring the transmission of X-rays and one measures some sort of "excitation' spectrum such as the fluorescence intensity as a function of the incident X-ray energy. The intensity of the X-ray fluorescence is proportional to the absorption probability because the creation of a core vacancy results in the emission of a fluorescence photon as outer electrons relax and fill the core vacancy. If the absorber density is relatively high, fluorescence measurements can result in technical problems. For example, if the composition of a sample is too rich in the element of interest, self-absorption can occur.

In this case, fluorescence photons are energetic enough to eject electrons in the sample and other fluorescence photons which contribute to great distortions of the spectrum. When an electron from the K shell is ejected upon absorption of an X-ray photon, Kα fluorescence emission and Auger emission are two competitive processes. The probability of these mechanisms depends on the atomic number of the absorber element. While fluorescence emission is more probable for heavy elements, Auger emission is more likely for lighter atoms. For the experiments performed in the fluorescence mode, two types of detectors were used, a Si(Li) detector and a Lytle detector.

2.1.5.4. The Si(Li) Detector

A Lithium-drifted Silicon detector was used for the experiments performed at ELSA. X-rays from the fluorescence process interact with the semiconductor silicon crystal to generate electron-hole pairs. The charge collected is then converted into a voltage which is proportional to the X-ray energy. This results in a spectrum displaying counts as a function of energy. Typically, fluorescence is detected at 90 ° from the sample normal. The Si(Li) detector used was a EG&G ORTEC SLP-16220-P, based on the detection by a single diode with a diameter of 16 mm and an energy resolution (FWHM) of 220 eV at 5900 eV.

2.1.5.5. The Lytle Detector

Typically, the Lytle detector designed by Lytle at the Stanford Synchrotron Radiation Light Source (SSRL),[21,23] is used to detect a signal from an absorber that displays a weak fluorescent yield, or when the concentration of the absorber atom is very low in the sample of interest (1000 ppm). The optimal configuration for detection of fluorescence in a Lytle detector is attained at a 45° angle between the incident beam

and the entrance slits of the detector. The Lytle chamber is a 3 cm-ion chamber that is filled with the appropriate absorbing gas depending on the energy of the absorber atom. For experiments involving Cu K-edge measurements, the Lytle detector was filled with krypton, whereas argon was used in experiments carried out at the Fe K-edge. A filter is placed directly in front of the Soller slits to absorb most of the elastic and Compton scattering from the sample. For Fe K-edge and Cu K-edge, (Z-1) filters made out of Mn and Ni, respectively, were chosen.

2.1.6. Scanning Tunneling Microscopy (STM)

Gerd Binnig and Heini Rohrer invented the scanning tunneling microscope (STM) in 1982.[24,25] The use of the STM, whose theory was proposed prior to its invention, has revolutionized fields such as semiconductor physics, materials science, chemistry, biochemistry, and a number of others.[26] The widespread use of STM is based on its ability to provide surface imaging with ultra-high resolution. STM is based on the understanding of electron tunneling, a phenomenon that was first studied as early as the 1920s.[27] When a conductive sharp tip is placed very close to a conducting sample surface, the electrons from the sample will tunnel to the surface of the tip when a voltage is applied. A schematic of the STM is shown in Figure 2.8. The tip, usually made of Pt or W, is mounted on a piezoelectric tube, which controls the motion of the tip in the x, y, and z directions. The piezoelectric reacts to the applied voltage by expanding or contracting in the direction perpendicular to the applied electric field. A saw-tooth voltage is applied to the x piezo, while a ramping voltage is applied to the y piezo, allowing the xy plane to be scanned.

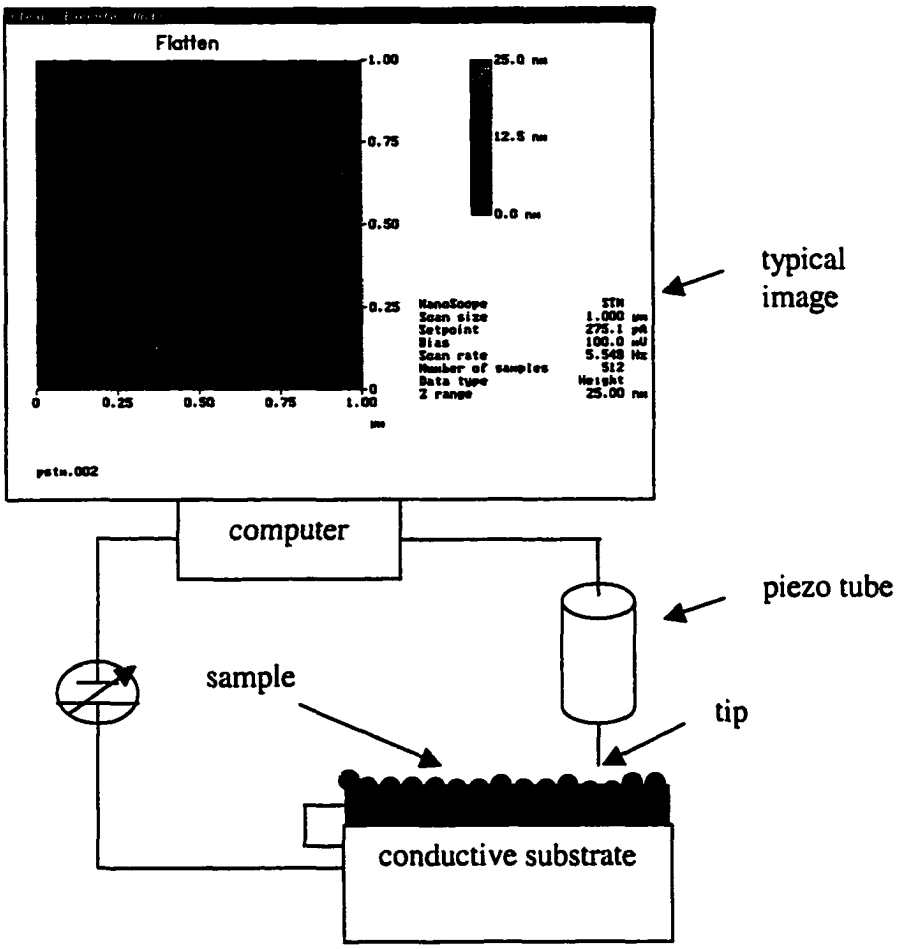

Figure 2.8. Schematic of a scanning tunneling microscope (STM).

The STM can be run while keeping the voltage between the tip and the sample constant in the constant-voltage mode or allowing the voltage to vary and fixing the height in the constant-height mode. In the constant-voltage (or constant-current) mode, the tunneling current is amplified and converted to a voltage that is compared to the reference value. A z piezo adjusts the height of the tip (or tip-sample separation distance) through a feedback loop until the voltage is equal to that of the reference value. Surface of the sample and tip behave as two conducting electrodes separated by a potential barrier. The transmission probability or tunneling current is determined by

solving the Schröedinger equation for an electron in a rectangular potential well.[27-30] The tunneling current (I) decreases exponentially with increased tip-sample separation distance, as expressed in equation (2.7), where d is the distance between the tip and the sample, and κ is the decay constant.

$$I \propto e^{-\kappa d} \qquad (2.7)$$

In the constant-height mode, the tip is scanned across the xy plane at a constant distance from the sample, and the measured variations in tunneling current allow for a 3D visualization of the surface to be obtained.

2.1.7. Atomic Force Microscopy (AFM)

Binnig et al. published the first AFM results in 1986.[31] The invention of the AFM by Binnig relied on the exploitation of the minute forces that were observed between the tip and the sample in the STM. In the original instrument, a STM tip was monitoring the deflections by attractive or repulsive forces exerted on a cantilever by the sample. Later on, the monitoring of the deflections was achieved through the use of optical technology. The forces exerted between two atoms can be of short or long order, repulsive or attractive. The theory behind AFM is based on long-order interactions, taking into account an average of the individual forces exerted between atoms. Different theories have been proposed to explain the interactions between atoms and their utilization for AFM imaging.[32] The treatment of AFM theory involves a complex combination of interactions such as tip-sample, Coulomb, ion-dipole, dipole-dipole, van der Waals.

A schematic of a typical AFM is shown in Figure 2.9. The triangular Au cantilever is characterized by a spring constant that depends on its shape and size (width and length of the triangle legs). The cantilever is brought into contact with the surface

of the sample. A laser beam is directed onto the end of the reflective Au cantilever, and the reflected beam is aligned in order to optimize its collection by a four-quadrant photodiode.

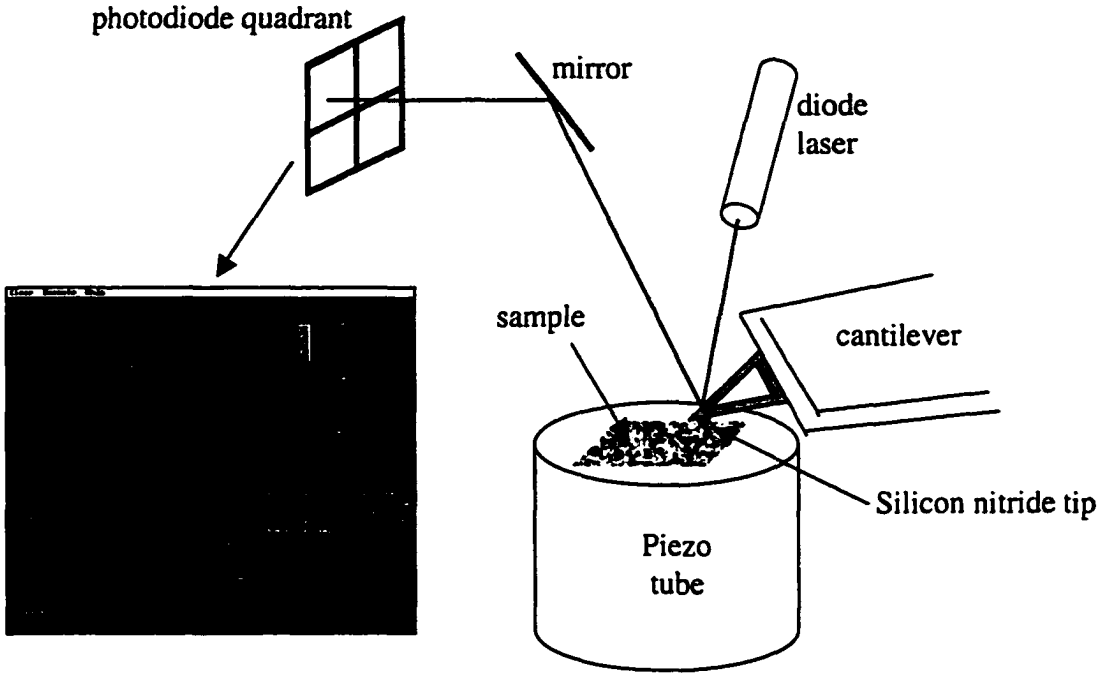

Figure 2.9. Schematic of an atomic force microscope (AFM).

A piezoelectric tube controls the motion of the sample in the x, y, and z directions. While scanning the motion of the sample, the deflections of the cantilever are monitored by recording the signal from the four-quadrant photodiode. Variations in the signal received by the photodiode are representative of the topography of the studied surface. One of the main advantages of AFM is its ability to operate on conducting as well as insulating samples.

2.1.8. Lateral Force Microscopy (LFM)

In LFM, the torsion induced on the cantilever by the sample is monitored (cantilever roll) and is proportional to the frictional forces between tip and sample.[33,34]

LFM was introduced by Meyer and Amer,[35] who correlated the torsion of the cantilever with the amplitude of the frictional forces. The ability of LFM ability to map chemically distinct domains with nanometer resolution was first shown by Green et al.[7] and Frisbie et al.[36] Given the lateral and normal spring constants of the cantilevers (k_l and k_N) expressed in N/nm, lateral and normal forces are derived from Hooke's law[37] in equation (2.8)

where

$$F_N = \Delta V \times k_N \times Z_{sensitivity} \qquad (2.8)$$

and ΔV is given by equation (2.9).

$$\Delta V = \left| Voltage\ @\ pulloff - setpoint \right| \qquad (2.9)$$

$Z_{sensitivity}$ is measured as the slope of the contact line in the force mode of the microscope. The slope of the contact line is determined by averaging at least 5 scan measurements. Calculation of the lateral force involves the acquisition of friction loops. A typical friction loop, displayed in Figure 2.10, allows for the sensitivity of the detector to be calculated.

The lateral force is given by equation (2.10)

$$F_l = k_l \times \Delta X \qquad (2.10)$$

where

$$\Delta X = (\text{TMR/2 in V}) \times (\text{sensitivity in nm} \times V^{-1}) \qquad (2.11)$$

TMR (trace mode retrace) represents the sum of the friction curve intensity in the trace mode and in the retrace mode of the microscope. A plot of lateral force versus normal force is linear with the slope representing the friction coefficient and provides us with a way to characterize a surface or differentiate between the different constituents of a mixture on a surface.

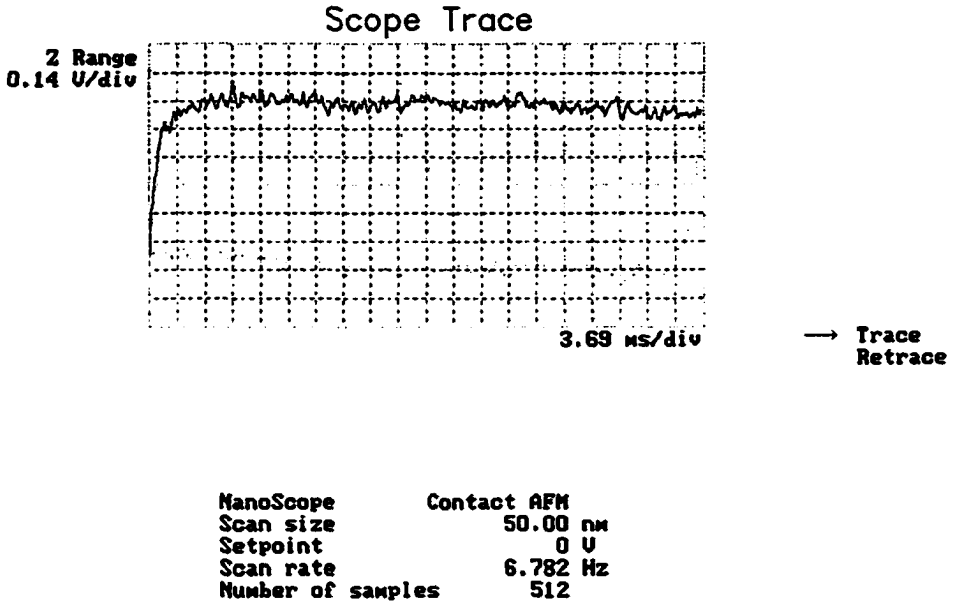

Figure 2.10 Typical friction loop obtained in the contact mode of the AFM.

2.1.9. Transmission Electron Microscopy (TEM)

Transmission electron microscopy was developed in 1935 by Ruska (who was awarded a Nobel Prize later in 1986), von Borries, and Knoll in Berlin.[38] Routinely used in most materials characterization laboratories around the world, the TEM is complementary to electron diffraction, and it provides a way to image microscopic and nanoscopic materials with high resolution. In a conventional microscope, the sample is irradiated with an electron beam in the range 10-150 keV or in the range 150 keV-3 MeV for high-voltage TEM. In Figure 2.11. is shown a schematic of a TEM.

Electrons are produced by an electron gun and accelerated by a potential V_0. The electron beam is propagated in a vacuum that depends on the type of the gun. Typically, a vacuum of 10^{-5} is enough for thermo-ionic W filament gun, whereas, higher vacuum is necessary for a LaB_6 gun or a field emission gun. Two sets of condenser lenses are used to control the illumination aperture and the irradiated sample area. A

carbon-coated copper grid serves as a support for the sample (deposited as a thin film) and is placed directly after the condensing system. The objective, whose role is to focus the beam onto the object is placed after the sample and is followed by the objective diaphragm, which determines the aperture α. An image is then formed onto the image plan of the objective and projected onto a fluorescent screen by a system of projector lenses. Image collection can be realized through photographic emulsion, or digitally with a charge-coupled device (CCD).

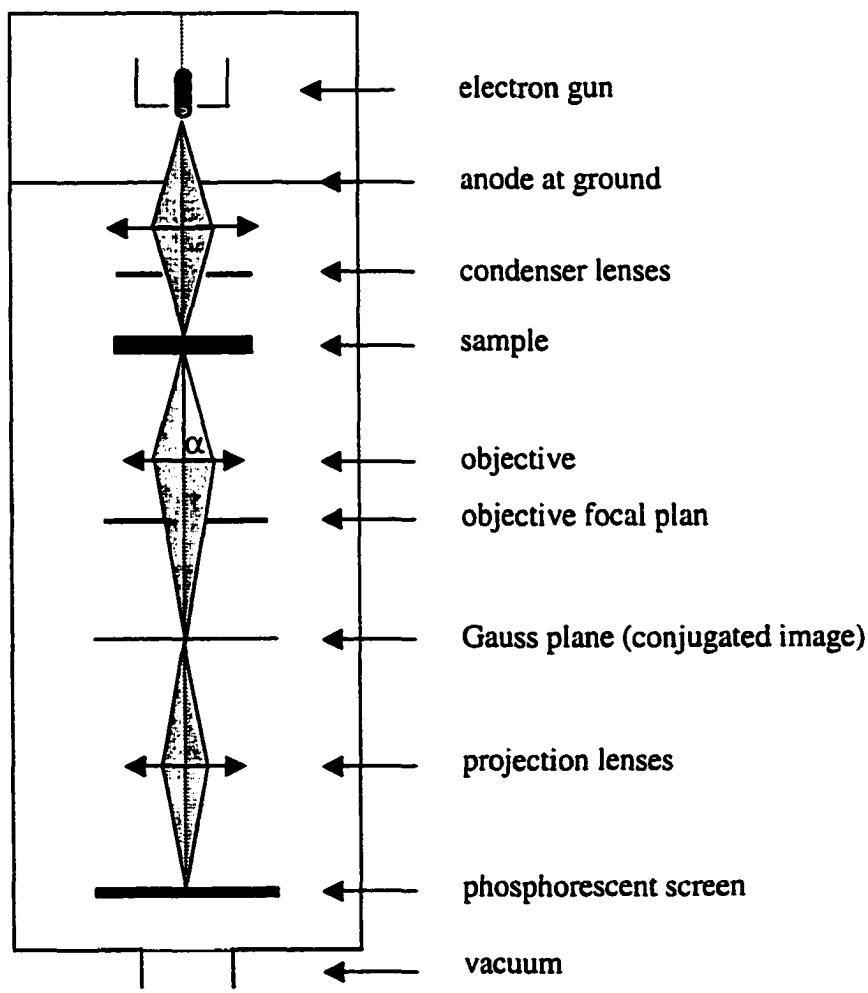

Figure 2.11. Basic elements of a transmission electron microscope.

Diffraction phenomena at the objective diaphragm limit the resolution whose expression is given in equation (2.12).

$$d = \frac{0.61 \times \lambda}{n \times \sin \alpha} \qquad (2.12)$$

where d is the smallest distance between two points from the object that can be separated in the image formed by the objective, λ is the wavelength, n is the refractive index of the medium between the object and the objective, and α is the objective aperture.

2.2. Bibliography

2.1) Chidsey, C. E. D.; Loiacono, D. N.; Sleator, T.; Nakahara, S. *Surf. Sci.* **1988**, *200*, 45-66.

2.2) McKendry, R.; Theoclitou, M.-E.; Abell, C.; Rayment, T. *Langmuir* **1998**, *14*, 2846-2849.

2.3) Willicut, R. J.; McCarley, R. L. *Langmuir* **1995**, *11*, 296.

2.4) Increasing the molar ratio of $NaBH_4$ does not induce any change in the UV-vis spectra of any of the DAB-Am_n-$Cu(0)_{cluster}$ complexes but prevents the rapid oxidation of the copper atoms back to Cu(I) or Cu(II), thus increasing their stability.

2.5) Takada, K.; Diaz, D. J.; Abruna, H. D.; Cuadrado, I.; Casado, C.; Alonso, B.; Moran, M.; Losada, J. *J. Am. Chem. Soc.* **1997**, *119*, 10763-10773.

2.6) Digital Instruments, *Santa Barbara, CA.*

2.7) Green, J.-B. D.; McDermott, M. T.; Porter, M. D. *J. Phys. Chem.* **1995**, *99*, 10960-10965.

2.8) Schilling, P.; Morikawa, E.; Tolentino, H.; Tamura, E.; Kurtz, R. L.; Cusatis, C. *Rev. Sci. Instrum.* **1995**, *66*, 2214-2216.

2.9) Lemonnier, M.; Collet, O.; Depautex, C.; Esteva, J.-M.; Raoux, D. *Nucl. Instrum. Met.* **1978**, *152*, 109-111.

2.10) Molders, N.; Moser, H. O.; Saile, V.; Schilling, P. J. *Dissertation* **1999**.

2.11) Canberra Industries Inc. *800 Research Parkway, Meriden, CT 06450*.

2.12) Koningsberger, D. C.; Prins, R. *X-ray absorption ; principles, applications, techniques of EXAFS, SEXAFS and XANES*; John Wiley & sons: New York, 1988.

2.13) Koch, E.-E. *Handbook on synchrotron radiation, 1A* Amsterdam, 1983.

2.14) Craft, B. C.; Feldman, M.; Morikawa, E.; Poliakoff, E. D.; Saile, V.; Scott, J. D.; Stockbauer, R. L. *Rev. Sci. Instrum.* **1992**, *63*, 1561.

2.15) Koch, E.-E. *Handbook on synchrotron radiation, 1B* Amsterdam, 1983; Vol. 1B.

2.16) Kronig, R. D. L. *Z. Phys.* **1931**, *70*, 317.

2.17) Sayers, D. E.; Lytle, F. W.; Stern, E. A. *Advan. X-ray Anal.* **1970**, *13*, 248-271.

2.18) Sayers, D. E.; Stern, E. A.; Lytle, F. W. *Phys. Rev. Lett.* **1971**, *27*, 1204-1207.

2.19) Sayers, D. E. *Phys. Rev. B* **1975**, *11*, 4836-4845.

2.20) Lytle, F. W.; Sayers, D. E.; Stern, E. A. *The history and modern practice of EXAFS spectroscopy. In: Advances in X-ray Spectroscopy*; Pergamon: Oxford, 1982.

2.21) Stern, E. A.; Heald, S. M. *Rev. Sci. Instr.* **1979**, *50*, 1579-1582.

2.22) Teo, B. K. **1986**.

2.23) Stanford Synchrotron Radiation Light Source *Guide to EXAFS Measurements at SSRL.*

2.24) Binnig, G.; Rohrer, H. *Hev. Phys. Acta* **1982**, *55*, 726.

2.25) Binnig, G.; Rohrer, H.; Weibel, E. *Phys. Rev. Lett.* **1982**, *49*, 57.

2.26) Bottomley, L. A. *Anal. Chem.* **1998**, *70*, 425R-475R.

2.27) Stroscio, J. A.; Kaiser, W. J. *Scanning Tunneling Microscopy*; Academic Press Publishers, Inc: Boston, 1993; Vol. 27.

2.28) Wiesendanger, R.; Guntherodt, H.-J. *Scanning Tunneling Microscopy III* Berlin, 1993; Vol. 29.

2.29) Wiesendanger, R. *Scanning Probe Microscopy; Analytical Methods*; Springer: Berlin, 1998.

2.30) Bonnell, D. A. *Scanning Tunneling Microscopy and Spectroscopy; Theory, Techniques, and Applications*; VCH: New York, 1993.

2.31) Binnig, G.; Quate, C. F.; Gerber, C. *Phys. Rev. Lett.* **1986**, *56*, 930-933.

2.32) Sarid, D. *Scanning Force Microscopy with applications to electric, magnetic, and atomic forces*; Oxford University press: new York, Oxford, 1991.

2.33) Overney, R. M.; Meyer, E.; Frommer, J.; Brodbeck, D.; Luthi, R.; Howald, L.; Guntherodt, H.-J.; Fujihira, M.; Takano, H.; Gotoh, Y. *Nature* **1992**, *359*, 133-135.

2.34) Hoh, J. H.; Engel, A. *Langmuir* **1993**, *9*, 3310-3312.

2.35) Meyer, G.; Amer, N. M. *Appl. Phys. Lett.* **1990**, *57*, 2089-2091.

2.36) Frisbie, C. D.; Rozsnyai, L. F.; Noy, A.; Wrighton, M. S.; Lieber, C. M. *Science* **1994**, *265*, 2071-2074.

2.37) Burnham, N. A.; Colton, R. J.; Pollock, H. M. *J. Vac. Sci. Technol. A* **1991**, *9*, 2548-2555.

2.38) Eberhart, J. P. *Analyse structurale et chimique des materiaux*, 1989.

Chapter 3. LFM Investigations of Mixed Monolayers

3.1. Motivation for this Study

Previous work in our group has focused on pyrrole-containing self-assembled monolayers.[1-4] In particular, it was shown that poly(pyrrole) formation could be achieved on a surface through the use of pyrrole-terminated alkanethiol monolayers.[3] The properties of these films were further investigated by electrochemistry and STM in various environments in order to study their formation and stability. In the case of mixed hexanethiol/*ω*-(*N*-pyrrolyl)-hexanethiol monolayers, neither cyclic voltammetry nor STM were able to confirm polymer formation,[4] possibly as the result of phase separation or homogeneous mixing of our pyrrole-thiol and *n*-hexanethiol. In the study at hand, we are interested in monitoring the behavior of mixed monolayers of different compositions of *ω*-(*N*-pyrrolyl)-hexanethiol, (C_4H_4N-$(CH_2)_6$-SH), and *n*-octadecane-1-thiol by LFM.

When applying an increasing load (normal force) to a surface, the response of the surface (lateral force) linearly increases, following the equation:

$$F_l = \alpha F_N + f_o \qquad (3.1)$$

where F_N is the normal force, F_l the lateral force, α the coefficient of friction, and f_o a constant that is related to the chemical composition of the interface.[5] Values of α and f_o can be found in the literature for a number of surfaces modified with alkanethiols of different chain lengths[6] and different compositions (mixed monolayers).[5] In certain scenarios, monolayers composed of more than one constituent have been shown to phase separate, resulting in the formation of islands of one compound within the other one. For example, Hobara et al. have used STM and cyclic voltammetry to study the phase separation of monolayers of 1-hexadecanethiol and 3-

mercaptopropionic acid.[7] In addition, Hayes et al. reported LFM images showing domains of 4-ATP within an octadecanethiol monolayer.[8]

In order to check for the reliability of the LFM experimental procedure in our laboratories, we obtained F_l vs F_N plots for a series of single-component monolayers. The alkanethiols used were *n*-octadecane-1-thiol, (CH_3-$(CH_2)_{17}$-SH), 11-mercapto undecan-1-ol, (HO-$(CH_2)_{11}$-SH), and 4-aminothiophenol. Octadecanethiol and 4-ATP were purchased from Aldrich and used without any further purification. The substrates were prepared by deposition of 1500 Å of gold onto mica, annealing at 300 ° C for 3 hours, and exposure to ozone for 30 minutes. Clean gold substrates were immersed in 1 mM solutions of CH_3-$(CH_2)_{17}$-SH, or HO-$(CH_2)_{11}$-SH in ethanol. The lateral force measurements were performed under atmosphere using a multimode Nanoscope III (Digital Instruments) under ambient conditions. We used a commercially available triangular , or V-shaped cantilever with a Si_3N_4 pyramidal tip (30-50 nm tip radius) with a spring constant k_N=0.06 N/m.

The normal force corresponding to the applied load applied to the sample through the cantilever was calculated through the measurement of force curves. The normal force is given by the following equation derived from Hooke's law :

$$F_N\ (10^{-9}\ \text{N or nN}) = \Delta V\ (\text{V}) \cdot z_{sens}\ (\text{nm/V}) \cdot k_N\ (\text{N/m}) \qquad (3.2)$$

where ΔV is the absolute value of the difference between the voltage at pull-off and the setpoint voltage ($\Delta V = |\ V_{pull\text{-}off} - V_{setpoint}\ |$). $V_{pull\text{-}off}$ is the voltage at which the contact between the tip and the sample is lost. $V_{setpoint}$ is the operating voltage that allows for the load applied to the tip and the sample to be varied. z_{sens} is the sensitivity of the detector and is calculated as the inverse of the slope of the force curve in the

force mode of the Nanoscope III microscope. k_N is the spring constant of the cantilever (0.06N/m). The lateral force is calculated from equation (3.3).

$$F_l\ (nN) = k_l\ (N/m)\ .\ \Delta X\ (nm) \qquad (3.3)$$

ΔX can be calculated upon evaluation of the signal generated through 50 nm-friction loops using equation (3.4).

$$\Delta X\ (nm) = TMR/2\ .\ \text{detector sensitivity}\ (nm/V) \qquad (3.4)$$

The detector sensitivity is calculated through the average of five 5 nm-friction loops as the inverse of the slope of the contact line in the scope mode of the Nanoscope III microscope. The domains chosen for measurements were in all cases 5-nm-flat regions of the monolayer (pure or mixed) on a gold crystallite. The sensitivity was obtained from the slope of the contact line in the force mode. The pull-off voltage, which is supposed to remain constant throughout the experiment was checked at regular intervals. The nanoscope was then switched to the scope mode and 5 friction loops were captured for a given setpoint, chosen as the middle range of voltages applied, in order to calculate the sensitivity of the detector. Then, friction traces were collected through the use of 50 nm friction loops for each setpoint voltage. Using equations (3.2) and (3.3), the values of the lateral force can be calculated as a function of applied normal force.

3.2. Results Obtained for HO-$(CH_2)_{11}$-SH; Validation of the Method

Examples of results obtained for monolayers composed of HO-$(CH_2)_{11}$-SH on Au (111) are plotted in Figure 3.1. The values of the friction coefficient are derived from the slope of the best linear fit for each curve and are given in Figure 3.1. The standard deviation associated with the mean value of the friction coefficient (α=0.46) is low ($\pm$ 0.03), but this is not always the case. Extreme caution in the preparation of the

sample and the tip does not always prevent erroneous results to be acquired. In particular, we found that the value of the friction coefficient, α, could fluctuate by ± 100% in some cases even when the tip was rinsed between measurements of different samples. Accumulation of material on the tip is also responsible for extreme variations in f_0.

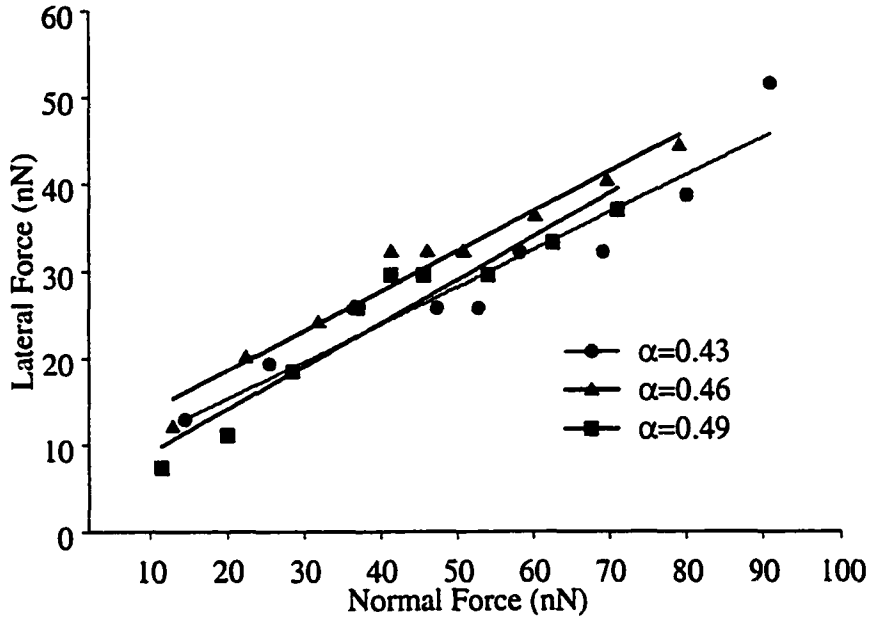

Figure 3.1. Variations of the coefficient of friction as a function of the applied load for HO-$(CH_2)_{11}$-SH on Au(111).

The relationship between lateral force and normal force is linear up to a given applied load. Past the critical load, different behaviors can be observed. This non-linear behavior has been reported by Lio et al.[9] who demonstrated the existence of a critical load for the applied normal force. In their study, they showed that beyond that critical load, the frictional force either fluctuates or decreases, and then stabilizes (a roll

off in response). In the study of 11-mercaptoundecan-1-ol, we found that the relationship between lateral force and normal force was linear until the applied force F_N reached ≈ 40 nN. The non linearity above the critical load is strongly correlated to changes in the contact area between tip and sample, and therefore depends on the radius of curvature of the tip.[10] In addition to this peculiar behavior of the lateral force, we observed a large scatter in the determination of the friction coefficient and f_0. With these observations in mind, we believe that extreme caution should be taken when interpreting lateral force data.

3.3. Mapping Chemically Distinct Domains

In order to verify the ability of LFM to differentiate between chemically distinct materials on a surface, we obtained curves of the lateral force as a function of the normal load applied for a series of thiols with different functionalities. The samples were prepared according to the experimental procedure described earlier. In Figure 3.2 are displayed the results obtained for monolayers of 4-ATP, 11-mercaptoundecan-1-ol, octadecanethiol, and ω-(*N*-pyrrolyl)-hexanethiol. For each compound, the values of the lateral force are plotted for a set of normal forces chosen below the critical load, which varies depending on the sample. The values obtained for f_0 and the friction coefficient α are given in Table 3.1.

Problems concerning the stability of f_0 were encountered during the experiments as illustrated in Figure 3.2 by the large variations in f_0. Therefore, a qualitative assessment of the graphs can not be done solely on the values of f_0. However, the large differences between the slope of the curves clearly demonstrate the ability of the frictional force method to differentiate between distinct chemical identities with the pyrrole sample exhibiting the largest friction coefficient.

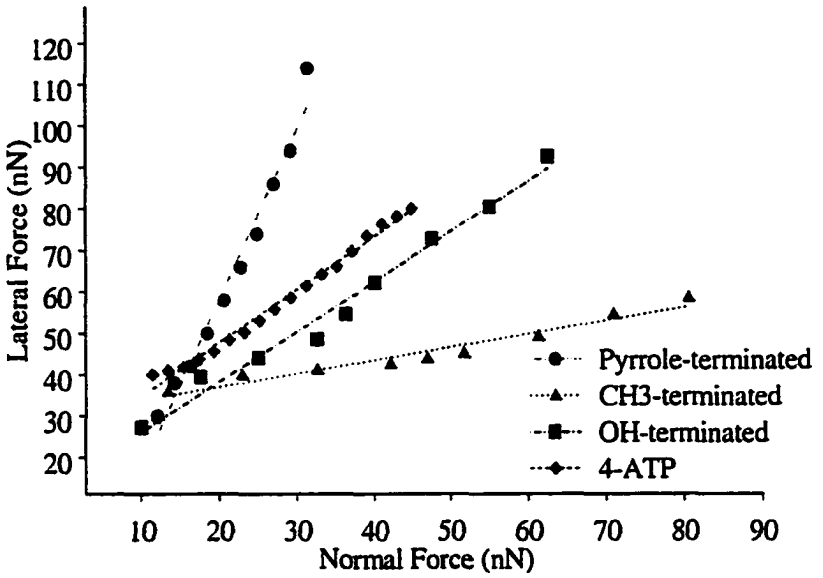

Figure 3.2. Variations of the coefficient of friction as a function of the applied load for HO-$(CH_2)_{11}$-SH, CH_3-$(CH_2)_{17}$-SH, 4-ATP, and pyrrole-terminated hexanethiol.

Table 3.1. f_0 and coefficient of friction α obtained for different monolayers as calculated from linear regression of the curves in Figure 3.2.

Mixture mole fraction	$X_{CH_3\text{-}(CH_2)_{17}\text{-}SH}$	$X_{C_4H_4N\text{-}(CH_2)_6\text{-}SH}$
X_{60}	0.40	0.60
X_{65}	0.35	0.65
X_{70}	0.30	0.70
X_{80}	0.20	0.80
X_{90}	0.10	0.90
X_{100}	0.00	1.00

As can be seen from examination of the curves in Figure 3.2, each of the samples verifies a linear relationship between the applied load and the resulting measured lateral force. The values of the friction coefficient listed in Table 3.2 were found to slightly vary between scans. However, the trend followed by these compounds with different functionalities is always verified. In other words, during the same experiment, and using the same cantilever, $\alpha_{pyrrole} > \alpha_{4\text{-}ATP} > \alpha_{hydroxyl} > \alpha_{methyl}$.

Fluctuations of f_0 for each functionality were also observed. Because of these observations, LFM can not be used to identify constituents in a mixture solely based on the values of α and f_0. However, LFM offers a way to compare relative abundances of two (or potentially more) distinct chemical entities in a mixture, because the friction coefficient is dependent on the functionality and chain length of the thiol as seen from the differences in slope for each sample. It is our belief that in order to acquire the most meaningful data, one must use the same cantilever throughout a set of experiments.

3.4. Mixed Monolayers of C_4H_4N-$(CH_2)_6$-SH and Octadecanethiol

This ability of LFM to distinguish between monolayers composed of different chemical functionalities was exploited to compare mixed monolayers made out of different molar fractions of pyrrole-terminated and methyl-terminated alkanethiols. A 1mM solution of C_4H_4N-$(CH_2)_6$-SH stored in a Ar-filled glove box was used for the preparation of the mixtures listed in table 3.2.

Table 3.2. Molar fractions of octadecanethiol and pyrrole-terminated hexanethiol in the mixtures.

compound	f_0	α
Py-$(CH_2)_6$-SH	13.8	4.10
4-ATP	22.1	1.28
HO-$(CH_2)_{11}$-SH	14.1	1.21
CH_3-$(CH_2)_{17}$-SH	30.7	0.32

The mixtures will be later referred to as X_n, with n reflecting the composition percentage of the mixture of ω-(*N*-pyrrolyl)-hexanethiol. The mixtures were prepared under argon and stored in an argon-filled glove box until they were analyzed in order to prevent oxidation of the pyrrole end groups. The composition of the mixtures has been

derived from the work reported by Hayes and Shannon[11] on mixed monolayers of 4-aminothiophenol and octadecanethiol on gold.

The curves obtained for different compositions of the mixed monolayers of pyrrole-terminated and octadecanethiol are shown in Figure 3.3.

A monolayer composed only of octadecanethiol exhibits a friction coefficient of 0.32 whereas a pyrrole-terminated monolayer is characterized by a friction coefficient of 4.10. The friction coefficients and the values of f_0 are listed for each composition of the monolayer in Table 3.3.

An increase of the friction coefficient can be seen when the composition of the mixed monolayer is increased in its pyrrole constituent. However, friction images collected for all compositions of the monolayers are similar and do not indicate that domains of either of the constituents is formed within the monolayer (phase separation).

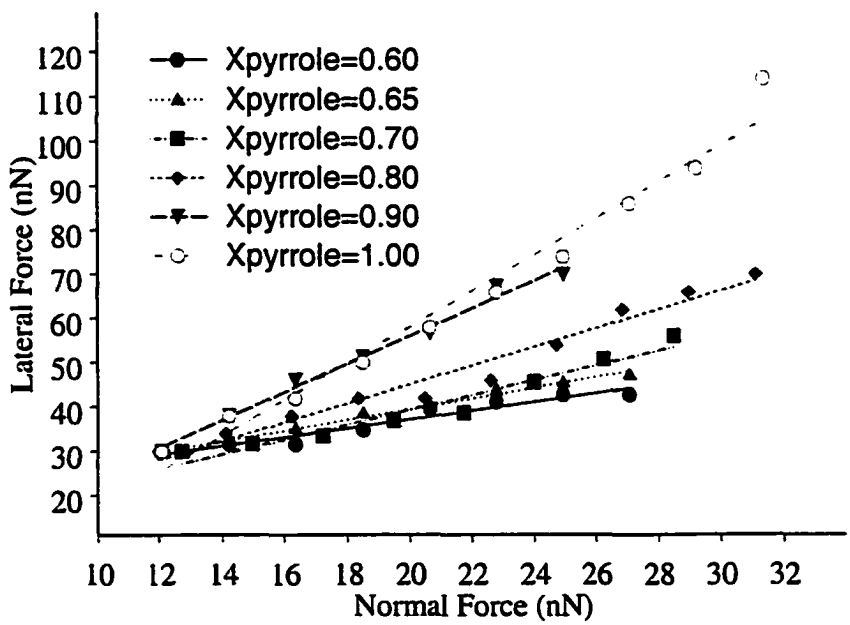

Figure 3.3. Variations of the coefficient of friction as a function of the applied load for the mixtures of CH_3-$(CH_2)_{17}$-SH and pyrrole-terminated hexanethiol.

Table 3.3. f_0 and coefficient of friction α obtained for different compositions of the mixture of C_{18} and pyrrole-terminated alkanethiol monolayers as calculated from linear regression of the curves in Figure 3.3.

molar fraction	f_0	α
$X_{C_{18}} = 0.40 . X_{pyrrole} = 0.60$	47.3	0.99
$X_{C_{18}} = 0.35 . X_{pyrrole} = 0.65$	45.4	1.20
$X_{C_{18}} = 0.30 . X_{pyrrole} = 0.70$	36.0	1.67
$X_{C_{18}} = 0.20 . X_{pyrrole} = 0.80$	32.7	2.12
$X_{C_{18}} = 0.10 . X_{pyrrole} = 0.90$	23.0	3.15
$X_{C_{18}} = 0.00 . X_{pyrrole} = 1.00$	13.8	4.10

The absence of contrast in imaging between the octadecanethiol and the pyrrole-terminated hexanethiol seems to indicate that instead of forming domains within the octadecanethiol matrix, the pyrrole-terminated thiols are distributed homogeneously throughout the monolayer. This proposition is supported by the increase of the coefficient of friction α with increasing molar fraction of the pyrrole constituent.

3.5. Conclusions

The lack of reproducibility of the data prevents this method to be used as a quantitative tool. The poor reproducibility of LFM data has been acknowledged by other groups.[12] Factors such as contact area, sample environment, non ideal positioning of the laser beam on the cantilever tip have been shown to be greatly responsible for important variations in LFM results, even within the same experiments. A procedure was proposed to correct for the influence of these factors. However, the estimation of the errors for V-shaped cantilevers being too complicated to model, only rectangular cantilevers were taken into account.[12] These considerations together with the power of LFM as a probing tool, emphasize on the importance of utilizing caution when

interpreting LFM data. One way to overcome these obstacles might be the derivatization of the cantilever tip with organic material. It is suggested that modifying the tips offers a more direct method for the investigation of chemically distinct domains on a surface.[5,13,14] Other steps include performing experiments in a fluid cell to minimize the effect of the accumulation of material on the tip or in vacuum to prevent oxidation and humidity.

3.6. Bibliography

3.1) Willicut, R. J.; McCarley, R. L. *J. Am. Chem. Soc.* **1994**, *116*, 10823-10824.

3.2) Willicut, R. J.; McCarley, R. L. *Langmuir* **1995**, *11*, 296.

3.3) Willicut, R. J.; McCarley, R. L. *Adv. Mater.* **1995**, *7*, 759-762.

3.4) Willicut, R. J.; McCarley, R. L. *Anal. Chim. Acta* **1995**, *307*, 269-276.

3.5) Green, J.-B. D.; McDermott, M. T.; Porter, M. D. *J. Phys. Chem.* **1995**, *99*, 10960-10965.

3.6) McDermott, M. T.; Green, J.-B. D.; Porter, M. D. *Langmuir* **1997**, *13*, 2504-2510.

3.7) Hobara, D.; Ota, M.; Imabayashi, S.-I.; Niki, K.; Kakiuchi, T. *J. Elec. Anal. Chem.* **1998**, *444*, 113-119.

3.8) Hayes, W. A.; Kim, H.; Yue, X.; Perry, S. S.; Shannon, C. *Langmuir* **1997**, *13*, 2511-2518.

3.9) Lio, A.; Morant, C.; Ogletree, D. F.; Salmeron, M. *J. Phys. Chem. B* **1997**, *101*, 4767-4773.

3.10) Putman, C. A. J.; Igarashi, M.; Kaneko, R. *Appl. Phys. Lett.* **1995**, *66*, 3221-3223.

3.11) Hayes, W. A.; Shannon, C. *Langmuir* **1996**, *12*, 3688-3694.

3.12) Schwarz, U. D.; Koster, P.; Wiesendanger, R. *Rev. Sci. Instrum.* **1996**, *67*, 2560-2567.

3.13) Noy A., F. C. D., Rozsnyai L. F., Wrighton M. S., Lieber C. M. *J. Am. Chem. Soc.* **1995**, *117*, 7943-7951.

3.14) Frisbie, C. D.; Rozsnyai, L. F.; Noy, A.; Wrighton, M. S.; Lieber, C. M. *Science* **1994**, *265*, 2071-2074.

Chapter 4. EXAFS and XANES Investigations of Alkanethiols Adsorbed on Metallic Substrates

4.1. Grazing Incidence Surface X-ray Absorption Fine Structure (GIXAFS) Study of Alkanethiols Adsorbed on Au, Ag, and Cu.

An extensive amount of literature has been published on alkanethiols adsorbed onto a number of substrates such as Ag,[1-12] Cu,[1,13-24] Pt,[2] Ni,[24-29] Al,[30] Rh,[31] Pd,[32] and Au.[1-8,33-110] Alkanethiols on gold are clearly the most studied of these systems. This is due to their ease of preparation, their robustness, and the fact that gold is not easily oxidizable or subject to contamination. Our interest for these systems is motivated by the need for a clearer understanding of the relationship between a strong chemisorption of the sulfur onto the gold substrate and the van der Waals interactions between the polymethylene chains, that contributes to the overall equilibrium of these architectures. We are seeking the answers to some fundamental questions that might facilitate the design and the use of these monolayers in different applications. Even with the extensive research into the properties of alkanethiol SAMs, there are still significant gaps in our understanding about the actual site of adsorption. It is widely believed that alkanethiols adsorb on Au such that the sulfur atoms reside in a fraction of the 3-fold-hollow sites of the hexagonal Au array yielding a $(\sqrt{3} \times \sqrt{3})R30°$ basic adsorbate lattice. Although this binding site model is supported by many studies [6,52,63,104], a recently proposed alternative model suggests that the alkane chains bind to the metal as *dialkyldisulfides* [76,96,111]. Also, it has been proposed that dialkylsulfides remain intact after adsorption on Au [105]. Thus, it is clear that a better understanding of the surface structure and bonding is required, and this point has been stressed in recent surface enhanced Raman scattering studies [112] and STM investigations [113] of SAMs on gold. In

addition, the adsorption of alkanethiols on Ag and Cu is even less documented [6,10,14,114] and thus warrants further investigation.

Surface EXAFS data at the sulfur K-edge of adsorbed alkanethiols on Ag(111) and Cu(111) have been reported by Hutt et al. [10] and Imanishi and co-workers [14], respectively. There are unique difficulties associated with the investigation of these systems by means of surface EXAFS. In the fluorescence detection mode, there are major obstacles arising from low sulfur fluorescence yield. Additionally, in the case of Au substrates, the large background resulting from Au (M-shell fluorescence) has made data collection nearly impossible. Finally, only a few surface EXAFS studies have targeted the sulfur K-edge region; [10,14,68] most of the investigations have been focused on carbon K-edge XANES.

We report grazing incidence surface EXAFS (GIXAFS) spectra of alkanethiols on Cu and Ag that have increased resolution due to less noise, smoother pre-edge and post-edge background, and increased usable photoelectron wave vector k range in comparison to those from previous work.[10,14] Preliminary GIXAFS results on Au are also reported. To our knowledge, *this is the first report on sulfur K-edge surface EXAFS data of alkanethiols on Au.* Within this study, we have obtained data for *n*-alkanethiols on all three substrates by measuring sulfur fluorescence resulting from excitation at grazing incidence (0.01° to 0.40°). It is known that the chain length of the thiol has an effect on the ordering and packing of the alkane chains of the monolayer.[106] In addition, it has been proposed that the chain length of the alkane moiety may have an impact on the way in which the sulfur functionality binds to the Au substrate.[115] This relationship between chain length and sulfur binding site on the metal surfaces studied here is noted in our study. By comparing the GIXAFS data of different chain length

alkanethiol SAMs on Au, Ag, and Cu, we are able to make inferences about the nature of S-*M* bond, as well as characteristics of the SAMs. The work presented, issued from a collaboration with the group of Dr. J. Hormes at the University of Bonn, Germany, serves as a progress report on our continuing efforts to better characterize the environment of the sulfur atom in alkanethiol-metal systems.

In Figure 4.1 are displayed the unsmoothed spectra obtained for self-assembled monolayers of pentanethiol (C_5), decanethiol (C_{10}) and octadecanethiol (C_{18}) on Ag. Data for self-assembled monolayers of C_5 and C_{18} on Cu are shown in Figure 4.2.

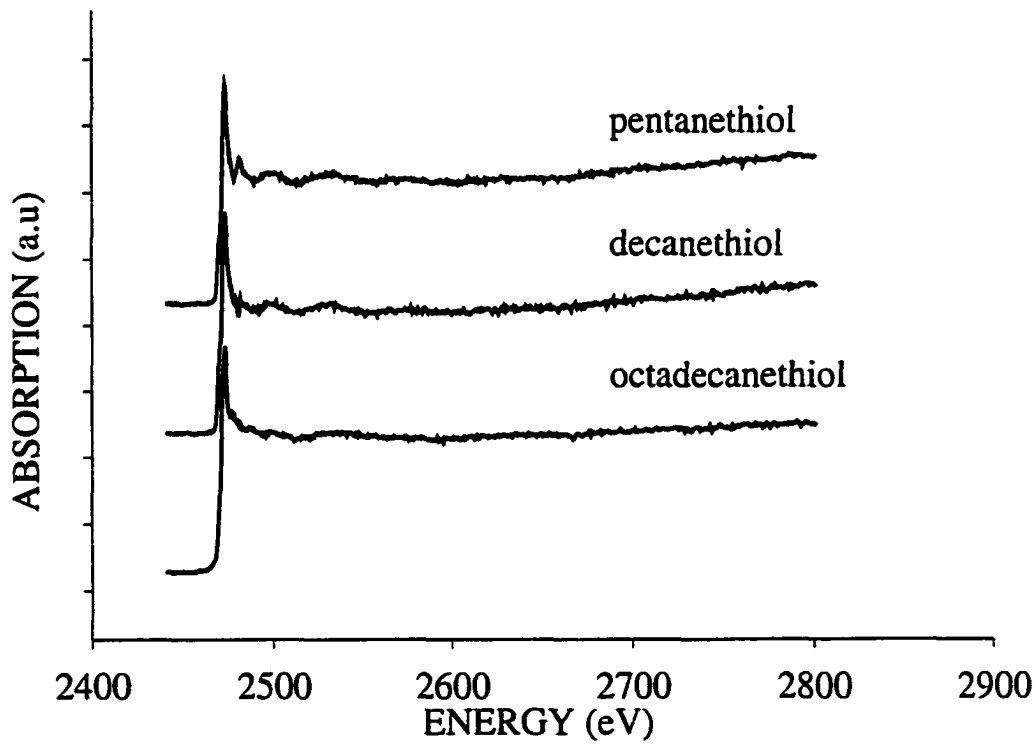

Figure 4.1. Sulfur K-edge EXAFS spectra of *n*-alkanethiols on Ag.

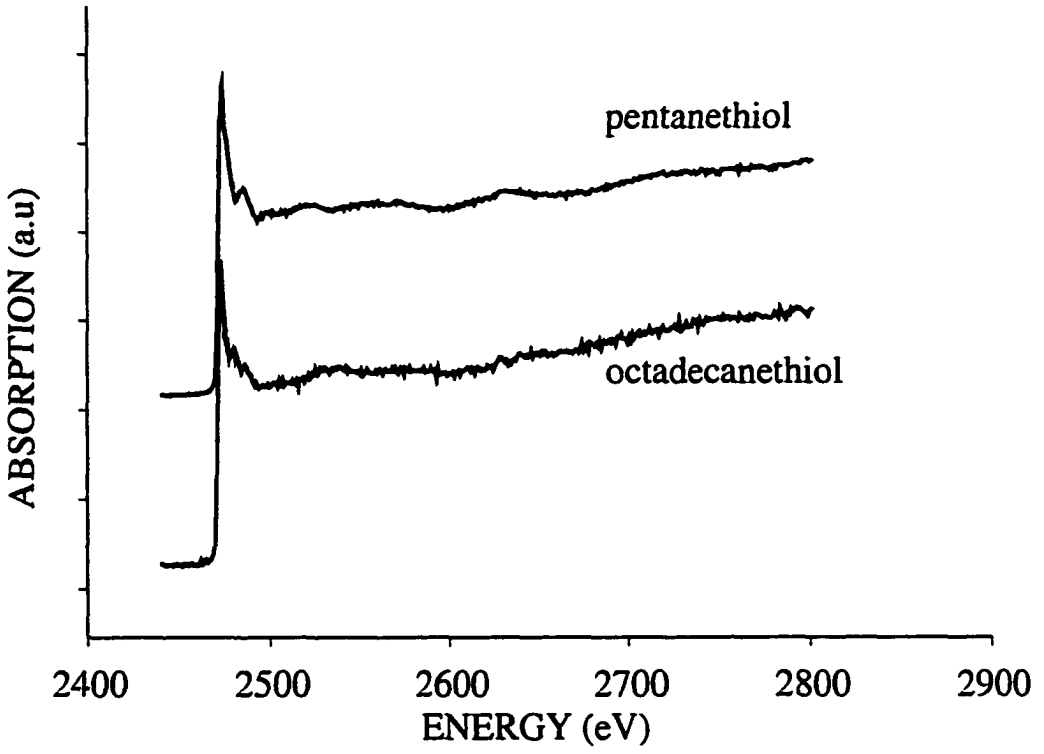

Figure 4.2. Sulfur K-edge EXAFS of *n*-alkanethiols on copper.

The data presented here are of improved quality in comparison to that obtained from electron yield detection methods as a result of lower noise, smoother background, as well as increased energy range of the fluorescence data. Specifically, the usable k range is thus increased from 3-6 $Å^{-1}$ to 3-9 $Å^{-1}$, which allows for a better determination of the bond distances around sulfur.[10]

A decrease in the amplitude of the EXAFS oscillations in the spectra is noted when moving from C_5 to C_{18}. This indicates that the environment of the sulfur absorber atom is dependent on the alkane chain length. In Figure 4.3 are displayed the Fourier transforms of the EXAFS function obtained for C_5, C_{10}, and C_{18} on Ag. The presence of two peaks in the Fourier transformed data is observed—the S-C peak and the S-Ag peak. The experimental data for C_5 and C_{10} on Ag can be fitted with a first shell of only 3 Ag atoms (sulfur atom adsorbed in the three-fold-hollow site). Small improvements

in the fit residual can be obtained if an additional Ag atom corresponding to an atop Ag atom bound to a sulfur atom is added. However, fitting of the C_{18} data with a fit index comparable to those of C_5 and C_{10} *requires* the use of both the three-fold-hollow and atop sites for location of the sulfur atoms.

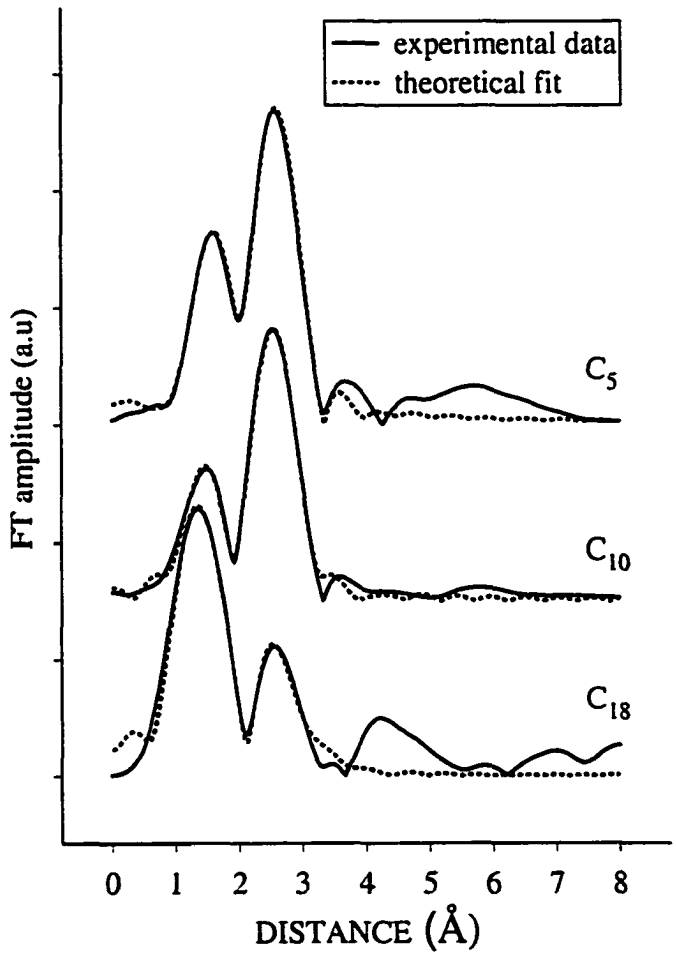

Figure 4.3. Fourier transform of the EXAFS function for C_5, C_{10}, and C_{18}.

Note that the Debye-Waller factor was locked during the fit at 0.005 $Å^{-2}$, a value that can typically be found in the literature.[10] When it was allowed to vary, its value would converge to 0.005. This indicates that the thermal disorder is comparable within the thiol series. Moreover, this is an indication that the effects that we report are not a

result of artifacts of the data analysis resulting from unphysical Debye-Waller factors. In Table 4.1 are listed various bond distances obtained for the three different chain length monolayers on Ag and Cu. It is observed that the S-C bond length is dependent on the number of methylene units in the alkanethiol chain. Similar observations have been found for monolayers on Cu.

Table 4.1. Bond distances for the various *n*-alkanethiols on Ag and Cu substrates.

Sample	S-C (Å)	S-M (Å) [atop]
C_5 on Ag	1.86 ± 0.06	2.52 ± 0.02
C_{10} on Ag	1.90 ± 0.04	2.50 ± 0.03
C_{18} on Ag	1.79 ± 0.03	2.54 ± 0.03 [2.00 ± 0.04]
C_5 on Cu	1.83 ± 0.04	2.29 ± 0.03
C_{18} on Cu	1.72 ± 0.06	2.25 ± 0.05 [2.70 ± 0.06]

A possible explanation for the observed differences in the data for the short (C_5 and C_{10}) and long (C_{18}) chain alkanethiols is one which relates the competing energetics of the S-*M* interaction and the chain-chain van der Waals interactions to the monolayer formation process. For short chain alkanethiols, the monolayer formation process should be dominated by the chemisorption reaction (~ 44 kcal mol^{-1}), while the van der Waals interactions will dominate for long chain alkanethiols.[63] In the case of C_{18}, the intermolecular chain-chain interactions dictate the arrangement of alkane chains, and thus the position of the sulfur head groups with respect to the Ag lattice. Such an "alkane chain-controlled" sulfur adsorption site model—three-fold hollow site for short chains and atop/three-fold hollow sites for long chains—is at odds with that proposed

for C_{10} and C_{18} on Ag(111) (based on data from scanning tunneling microscopy (STM)[116] and He/electron diffraction studies[117]). It was proposed in these previous two studies that the known $(\sqrt{7} \times \sqrt{7})R10.9°$ adlattice (both atop and three-fold hollow binding sites) for CH_3SH on Ag(111)[118] does not hold for C_{10}[116] and C_{18}[117]—an incommensurate (slightly expanded $(\sqrt{7} \times \sqrt{7})R10.9°$ structure) adlayer with roughly equivalent sulfur binding sites was suggested. It must be pointed out that the STM study focused exclusively on C_{10} and the diffraction study targeted solely C_{18}. Thus, a more extensive GIXAFS study involving a complete series of *n*-alkanethiols on Ag will be performed in the near future to test our hypothesis concerning monolayer structure and clarify the differences in the conclusions drawn from the work presented here and those from the previous STM and diffraction studies.

Additionally, the data for C_5, C_{10}, and C_{18} on Ag and Cu were fitted with a model involving a S-S bond of 2.2 Å (possible dialkyldisulfide monolayer structure[96,111]). It was impossible to fit our data to this disulfide model with a residual comparable to those discussed above, indicating that our data do not support evidence for the presence of dialkyldisulfide species on Ag or Cu. Furthermore, analysis of the data in the XANES region supports this EXAFS-based conclusion.

Spectra for monolayers of C_5 and C_{10} on Au are shown in Figure 4.4. *This is to our knowledge the first report of S K-edge surface EXAFS data for alkanethiols on Au.* In addition to the expected signals, the appearance of a sharp feature at 2481.44 eV indicates the presence of oxidized sulfur (S at the oxidation state +VI) in the monolayer, most likely the result of reactions with atmospheric species[7]; future studies will target the effects of sample environment on this oxidation process. Upon inspection and evaluation of the data in Figure 4.4, it is found that the usable k range (3-6 $Å^{-1}$) and

signal intensity are not as large as that found for Ag and Cu and currently make data analysis more challenging and less accurate. This latter issue is associated with the difficulty of extracting the sulfur signal from the overlapping Au fluorescence resulting from the M_{III}, M_{IV}, and M_V edges.

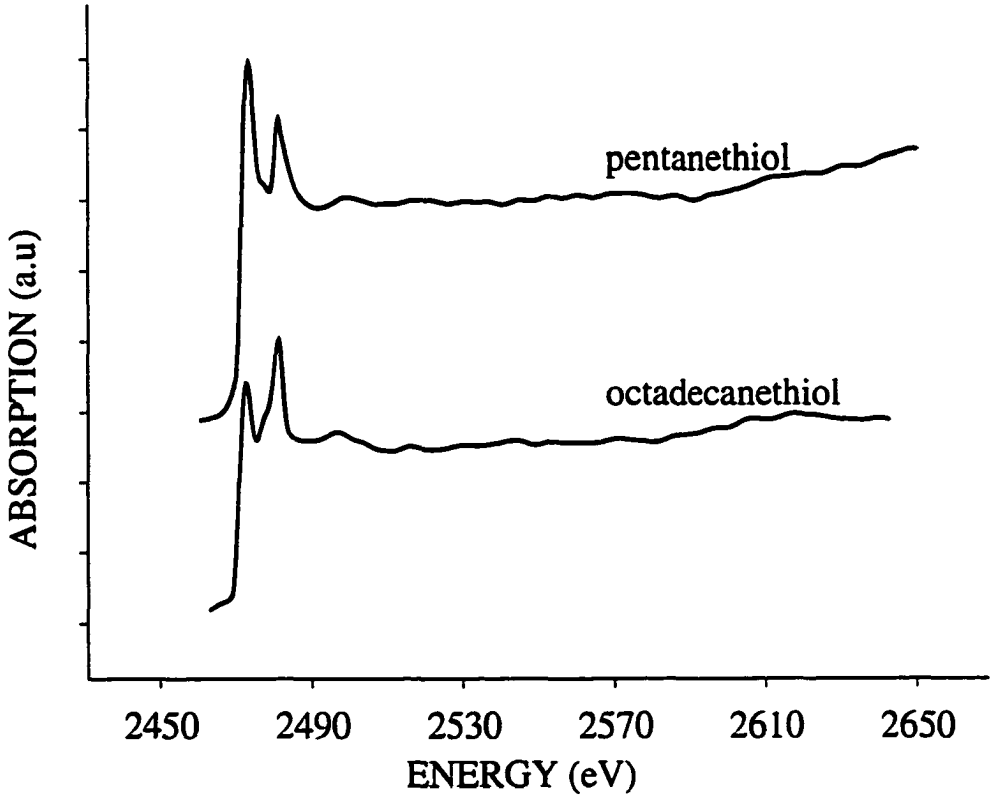

Figure 4.4. Sulfur K-edge EXAFS of *n*-alkanethiols on Au/mica.

However, these preliminary GIXAFS results for alkanethiols on Au are very encouraging. We are currently working on optimizing data obtained on Au by using a more sensitive detector.[119]

The current work holds promise for new avenues of research into XANES, as well. There has been considerable effort devoted to studying the correlation

between molecular bond lengths and energy shifts of above threshold shape resonances. It is possible that extensions of the work reported here can provide insights into correlations between XANES characteristics and *bond angles*. When sufficiently refined, such measurements will allow us to determine the geometry about the sulfur atoms precisely, including the bond angle. Because the bond angle about the sulfur atom is affected by the length of the alkyl chain, it will be possible to study the influence of bond angle on the XANES region with some precision. Higher quality data will be required, but the progress demonstrated by the current measurements can provide new insights into XANES measurements in the future. Thus, it is apparent that the current work lays the foundation for a range of further studies.

We have demonstrated the ability to acquire improved quality EXAFS data of alkanethiol monolayers on Ag and Cu by using Grazing Incidence X-ray Absorption Fine Structure (GIXAFS). This improvement will be beneficial to other studies involving a low concentration sample and/or a low Z backscatterer. The analysis of our data indicated no evidence for the presence of dialkyldisulfides on Cu or Ag. We have reported for the first time surface EXAFS data from monolayers adsorbed on Au. While there is still a need for improvement in order to make a more quantitative assessment of the environment around the sulfur head group, the data presented here demonstrate that such information is accessible. Our data analysis indicates that the three-fold hollow site is largely favored for short chain alkanethiols on Ag and Cu, whereas such a model is not sufficient to best fit the data obtained from C_{18} monolayers. This finding indicates that there may be a correlation between chain length and the monolayer formation process, and thus the site for adsorption of the sulfur head group may in part be dictated by the nature of the alkane chain. As stated previously, this

study represents considerable progress in determining the local geometry about the sulfur-metal bond and bodes well for investigations targeting SAMs on Au. Further experiments such as low temperature studies, which would minimize Debye-Waller effects and amplify the EXAFS oscillations, kinetic studies to investigate the competitive mechanisms for adsorption, as well as those focusing on the effects of chain length, are planned to further elucidate the structure of SAMs on the coinage metals.

4.2. Remarks on the Oxidation of the Alkanethiols on Ag, and Au

The first remark concerns the differences in oxidation observed between alkanethiol SAMs of various chain lengths. As can be seen in Figure 4.1, the amount of oxidation as reflected by the peak at 2481.44 eV, increases with increasing chain length. This observation is supported by oxidation studies of alkanethiol SAMs in air or photo-oxidized.[7,9] This is generally explained by the increased difficulty for an oxidant to penetrate through the longer chain thiols which are more tightly packed. The more closely packed, almost crystalline-like structure of the long chain alkanethiol SAMs, protects the surface-bound sulfur more effectively from oxidation than in the case of the short chain thiols.

The results presented for the alkanethiols on gold in Figure 4.4 were obtained using evaporated films of gold on mica as a substrate. We also have looked at monolayers that have been prepared with the same procedure but using Si(100) as a support for the gold film. A typical example of EXAFS data acquired for decanethiol on Au/Si is shown in Figure 4.5.

As is obvious from this spectrum, the near-edge region is very different from the spectra shown in Figure 4.4. This is due to the presence of a very strong signal at 2481.44 eV, that corresponds to sulfate species, or sulfur at the oxidation state +VI.

Because these systems were made according to the same procedure as the ones on Au/mica, and using ethanolic alkanethiol solutions of the same concentration (1mM), the surface coverage is expected to be the same.

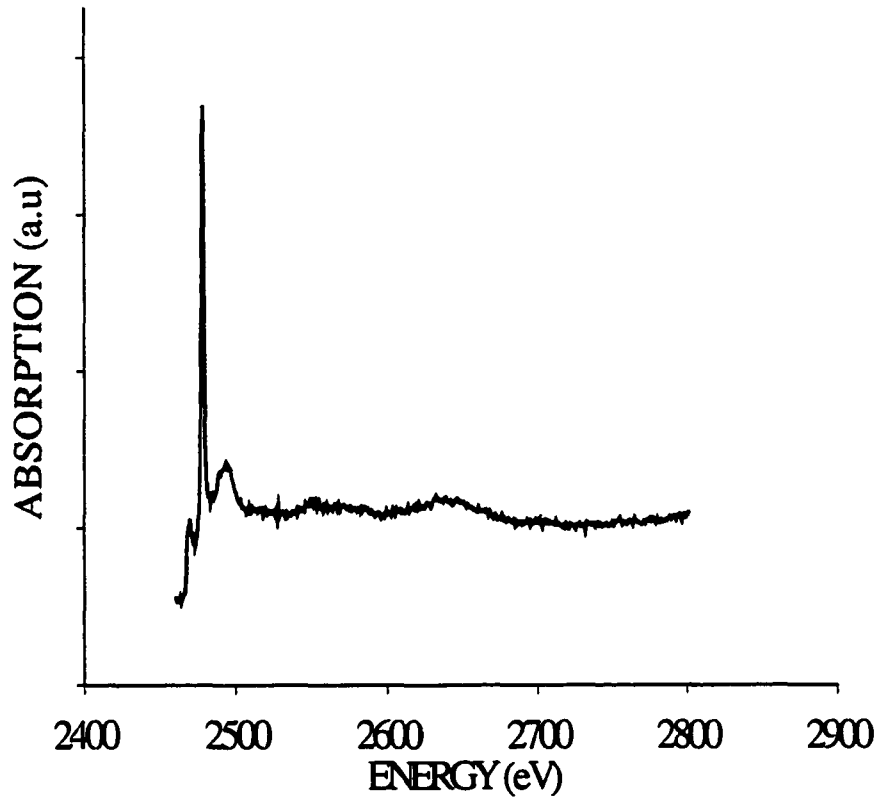

Figure 4.5. Sulfur K-edge EXAFS of *n*-alkanethiols on Au/Si.

In other words, the total amount of sulfur species on the surface is identical. However, as observed in Figure 4.5, the signal of sulfur at the oxidation state +II is very weak. This indicates that the sulfur atoms adsorbed on Au/Si are more prone to oxidation than the ones adsorbed on Au/mica. The presence of this sulfate peak greatly complicates the interpretation and analysis of the EXAFS spectrum as resonances from oxygen atoms of the sulfate species dominate the beginning of the EXAFS oscillations. The intensity of the sulfate peak at 2481 eV was very sensitive to the amount of ethanol and water rinsing, but the sulfate species did not convert back to S(II). The S(VI) peak

would ultimately disappear with thorough rinsing, indicating that the sulfate species were either weakly attached to the surface, or free alkyl-sulfonates were created upon scission of the metal-sulfur bond. Two mechanisms have been proposed for the oxidation of alkanethiol SAMs.[7,61] In one scenario, the oxidative agent penetrates through the monolayer, resulting in the oxidation of the sulfur atom into sulfonates, which induces S-C bond scission and the formation of sulfates at the surface through oxidation of the metal-bound sulfur. It has also been proposed that the S-M bond is broken upon oxidation resulting in the production of alkylsulfonates. In the latter case, the sulfonates can easily be rinsed with water and ethanol.

Our studies are consistent with both of these mechanisms, where the sulfate species ultimately disappear from the surface upon rinsing. The difference in behavior between alkanethiol SAMs on Au/Si and Au/mica could be an effect of surface roughness with a greater number of edge sites on Au/Si as compared to the large flatter crystallites obtained for Au/mica.

4.3. Probing the End-Group.

The very sensitive GIXAFS technique was also tested to probe iron absorber atoms in ferrocene-terminated alkanethiols. The structure of 11-ferrocenoyl-undecane-1-thiol. later referred to as Fc-C_{11} is given in Figure 2.1. EXAFS spectra of Fc-C_{11} as well as a mixture of Fc-C_{11} with C_{18} are shown in Figure 4.6.

These spectra clearly demonstrate the ability of GIXAFS to probe a very dilute layer of an element. This is especially true in the case of a 50/50 mixture of Fc-C_{11}/C_{18} where the surface coverage of the shortest thiol, here Fc-C_{11}, is supposed to be significantly smaller than in the case of a plain Fc-C_{11} monolayer.

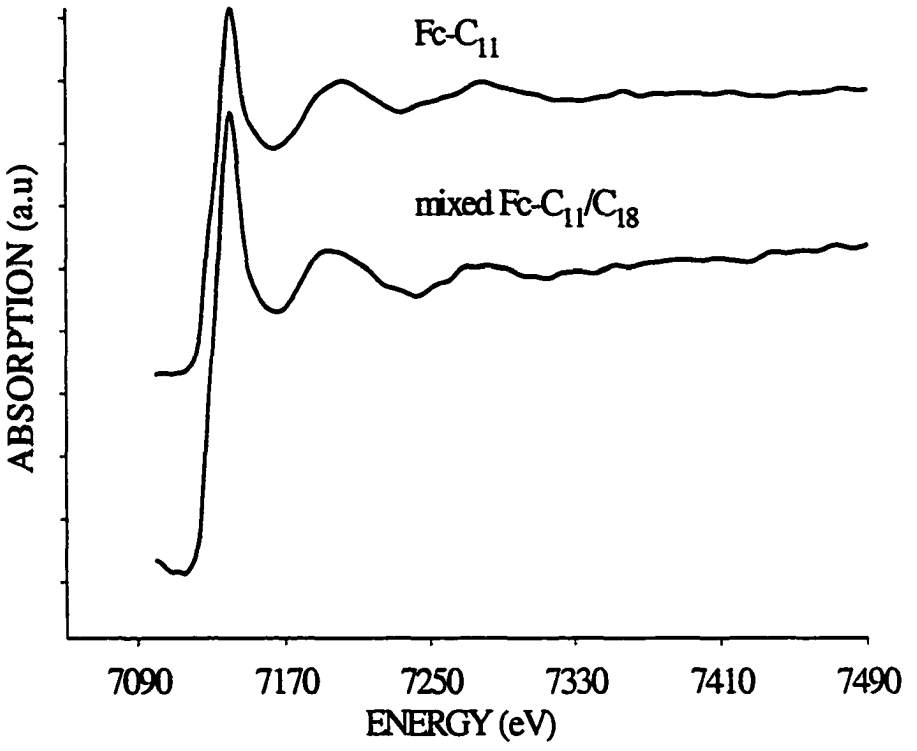

Figure 4.6. Iron K-edge EXAFS of ferrocene-terminated alkanethiols on Au/Si.

4.4. XANES Studies of Alkanethiols on Ag; The Unique Behavior of Octadecanethiol.

Upon careful inspection of the XANES spectra acquired at the BN2-DCM beamline, differences in the edge region of C_5, C_{10}, and C_{18} can be observed (Figure 4.7). As C_5 and C_{10} are characterized by an oxidation peak of the sulfur at around 2481 eV, C_{18} exhibits a sharp feature at 2487 eV.

In addition, the oxidation peak that corresponds to the formation of sulfinates, sulfonates, and sulfates, is shown to decrease with increasing chain length, which supports previous work by Hutt and Schoenfisch[7,9] We decided to conduct experiments in order to characterize the behavior of a more complete series of alkanethiol SAMs.

Experiments conducted at the BN2-DCM beamline at ELSA with pentanethiol, decanethiol, and octadecanethiol were reproduced at the XMP beamline at CAMD and completed with a set of experiments with dodecanethiol (C_{12}), tetradecanethiol (C_{14}),

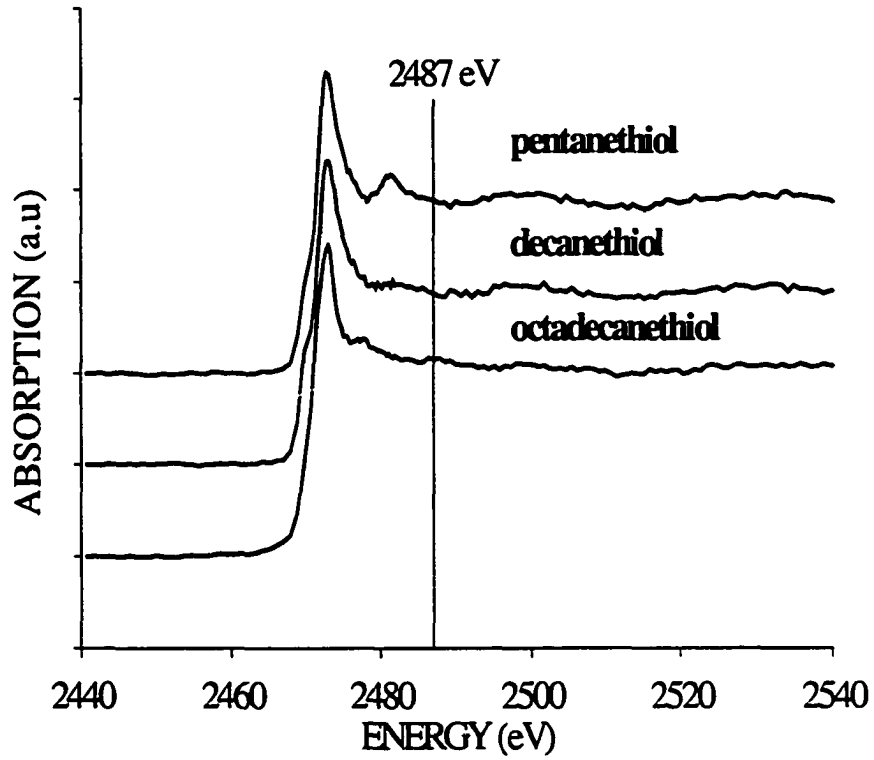

Figure 4.7. Sulfur K-edge XANES of *n*-alkanethiols on Ag/Si measured at ELSA.

hexadecanethiol (C_{16}), and eicosanethiol (C_{22}). For the CAMD experiments, C_5 and C_{10} were substituted for C_6 and C_{12}, which are of comparable chain length. In Figure 4.8 are shown XANES spectra obtained from C_6, C_{12}, and C_{18} taken at the XMP beamline at CAMD.

The similarities with Figure 4.7 are striking, demonstrating the reproducibility of the XANES features, obtained from different light sources, instrumentation, and chemicals. C_{18} clearly exhibits a resonance at 2487 eV that does not appear for either C_6 or C_{12}.

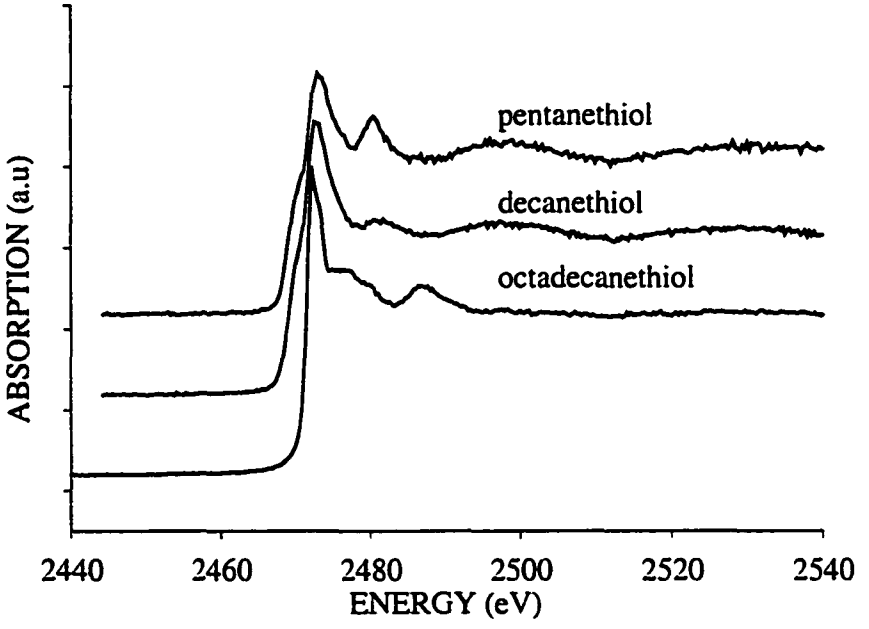

Figure 4.8. Sulfur K-edge XANES of *n*-alkanethiols on Ag/Si measured at CAMD.

We performed experiments on C_{14}, C_{16}, and C_{22} but could not identify such a feature for any of these compounds. As the highest possible oxidation state (+VI) of sulfur lies at 2481.44 eV, we can discard any oxidation cause as being responsible for this feature. It was deduced from our EXAFS work,[1] that C_{18} does not follow the same adsorption model as C_5 and C_{10} on the metallic substrate. Additionally to the sulfur binding to the metal in the three-fold hollow site, atop sites where the sulfur sits on top of the metal had to be considered in order to satisfy fitting parameters for C_{18}. The sharp resonance observed for C_{18} in the XANES region could be a consequence of this particularity. This intriguing feature for C_{18} was shown to be very sensitive to minute changes in incidence angle. Further experiments are needed to explain the unique behavior of C_{18}, with some of them developed in the conclusion of this dissertation.

4.5. Bibliography

4.1) Floriano, P. N.; Schlieben, O.; Doomes, E. E.; Klein, I.; Janssen, J.; Hormes, J.; Poliakoff, E. D.; McCarley, R. L. *Chem. Phys. Lett.* **2000**, *321*, 175-181.

4.2) Hines, M. A.; Todd, J. A.; Guyor-Sionnest, P. *Langmuir* **1995**, *11*, 493-497.

4.3) Tarlov, M. J.; Burgess, D. R. F.; Gillen, G. *J. Am. Chem. Soc.* **1993**, *115*, 5305-5306.

4.4) Patrito, E. M.; Olivera, P. P.; Sellers, H. *Surf. Sci.* **1997**, *380*, 264-282.

4.5) Ehler, T. T.; Malmberg, N.; Noe, L. J. *J. phys. Chem. B* **1997**, *101*, 8043.

4.6) Sellers, H.; Ulman, A.; Shnidman, Y.; Eilers, J. E. *J. Am. Chem. Soc.* **1993**, *115*, 9389-9401.

4.7) Schoenfisch, M. H.; Pemberton, J. E. *J. Am. Chem. Soc.* **1998**, *120*, 4502-4513.

4.8) Laibinis, P. E.; Bain, C. D.; Nuzzo, R. G.; Whitesides, G. M. *J. Phys. Chem.* **1995**, *99*, 7663-7676.

4.9) Hutt, D. A.; Cooper, E.; Leggett, G. J. *J. Phys. Chem. B* **1998**, *102*, 174-184.

4.10) Hutt, D. A.; Cooper, E.; Legget, G. J. *Surf. Sci.* **1998**, *397*, 154-163.

4.11) Gutierrez-Sosa, A.; Walsh, J. F.; Muryn, C. A.; Finetti, P.; Thornton, G.; Robinson, A. W.; D'Addato, S.; Frigo, S. P. *Surf. Sci.* **1996**, *364*, L519-L524.

4.12) Olivera, P. P.; Patrito, E. M.; Sellers, H. *Surf. Sci.* **1998**, *418*, 376-394.

4.13) Ron, H.; Cohen, H.; Matlis, S.; Rappaport, M.; Rubinstein, I. *J. phys. Chem. B* **1998**, *102*, 9861-9869.

4.14) Imanishi, A.; Isawa, K.; Matsui, F.; Tsuduki, T.; Yokoyama, T.; Kondoh, H.; Kitajima, Y.; Ohta, T. *Surf. Sci.* **1998**, *407*, 282-292.

4.15) Sung, M. M.; Sung, K.; Kim, C. G.; Lee, S. S.; Kim, Y. *J. Phys. Chem. B* **2000**, *104*, 2273-2277.

4.16) Rieley, H.; Kendall, G. K.; Chan, A.; Jones, R. G.; Ludecke, J.; Woodruff, D. P.; Cowie, B. C. C. *Surf. Sci.* **1997**, *392*, 143-152.

4.17) Loepp, G.; Vollmer, S.; Witte, G.; Woll, C. *Langmuir* **1999**, *15*, 3767-3772.

4.18) Nakahashi, T.; Hamamatsu, H.; Terada, S.; Sakano, M.; Matsui, F.; Yokoyama, T.; Kitajima, Y.; Ohta, T. *J. Phys. IV France* **1997**, *C2*, 679-681.

4.19) Atrei, A.; Johnson, A. L.; King, D. A. *Surf. Sci.* **1991**, *254*, 65-72.

4.20) Yagi, S.; Yokoyama, T.; Kitajima, Y.; Imanishi, A.; Takaneka, S.; Ohta, T. *Physica B* **1995**, *208&209*, 447-448.

4.21) Nakahashi, T.; Terada, S.; Yokoyama, T.; Hamamatsu, H.; Kitajima, Y.; Sakano, M.; Matsui, F.; Ohta, T. *Surf. Sci.* **1997**, *373*, 1-10.

4.22) Prince, N. P.; Seymour, D. L.; Woodruff, D. P.; Jones, R. G.; Walter, W. *Surf. Sci.* **1989**, *215*, 566-576.

4.23) Jayassoriya, U. A.; Anson, C. E.; Al-Jowder, O.; D'Alfonso, G.; Stanghellini, P. L.; Rosseti, R. *Surf. Sci.* **1993**, *294*, 131-140.

4.24) Kiguchi, M.; Yokoyama, T.; Terada, S.; Sakano, M.; Okamoto, Y.; Ohta, T.; Kitajima, Y.; Kuroda, H. *Phys. Rev. B* **1997**, *56*, 1561-1567.

4.25) Takata, Y.; Yokoyoma, T.; Yagi, S.; Happo, N.; Sato, H.; Seki, K.; Ohta, T.; Kitajima, Y.; Kuroda, H. *Surf. Sci.* **1991**, *259*, 266-274.

4.26) Yokoyama, T.; Terada, S.; Yagi, S.; Imanishi, A.; Takenaka, S.; Kitajima, Y.; Ohta, T. *Surf. Sci.* **1995**, *324*, 25-34.

4.27) Terada, S.; Imanishi, A.; Yokoyama, T.; Takenaka, S.; Kitajima, Y.; Ohta, T. *Surf. Sci.* **1995**, *336*, 55-62.

4.28) Ohta, T. *Physica B* **1995**, *208&209*, 427-430.

4.29) Fernandez, A.; Espinos, J. P.; Gonzalez-Elipe, A. R.; Kerkar, M.; Thompson, P. B. J.; Ludecke, J.; Scragg, G.; de Carvalho, A. V.; Woodruff, D. P.; Fernandez-Garcia, M.; Conesa, J. C. *J. Phys.:Condens. Matter* **1995**, *7*, 7781-7796.

4.30) Shen, W.; Nyberg, G. L. *Surf. Sci.* **1993**, *296*, 49-56.

4.31) Uvdal, K.; Kariis, H.; Westermark, G.; Wirde, M.; Gelius, U.; Persson, I.; Liedberg, B. *Langmuir* **1998**, *14*, 7189-7196.

4.32) Terada, S.; Sakano, M.; Kitajima, Y.; Yokoyama, T.; Ohta, T. *J. Phys. IV France* **1997**, *7*, 703-704.

4.33) Hobara, D.; Ota, M.; Imabayashi, S.-I.; Niki, K.; Kakiuchi, T. *J. Elec. Anal. Chem.* **1998**, *444*, 113-119.

4.34) Hayes, W. A.; Shannon, C. *Langmuir* **1996**, *12*, 3688-3694.

4.35) Hayes, W. A.; Kim, H.; Yue, X.; Perry, S. S.; Shannon, C. *Langmuir* **1997**, *13*, 2511-2518.

4.36) Chailapakul, O.; Sun, L.; Xu, C.; Crooks, R. M. *J. Am. Chem. Soc.* **1993**, *115*, 12459-12467.

4.37) McDermott, M. T.; Green, J.-B. D.; Porter, M. D. *Langmuir* **1997**, *13*, 2504-2510.

4.38) Xu, S.; Cruchon-Dupeyrat, S. J. N.; Garno, J. C.; Liu, G.-Y.; Jennings, G. K.; Yong, T.-H.; Laibinis, P. E. *J. Chem. Phys.* **1998**, *108*, 5002-5012.

4.39) Bonner, T.; Baratoff, A. *Surf. Sci.* **1997**, *377-379*, 1082-1086.

4.40) Lio, A.; Morant, C.; Ogletree, D. F.; Salmeron, M. *J. Phys. Chem. B* **1997**, *101*, 4767-4773.

4.41) Willicut, R. J.; McCarley, R. L. *J. Am. Chem. Soc.* **1994**, *116*, 10823-10824.

4.42) Willicut, R. J.; McCarley, R. L. *Anal. Chim. Acta* **1995**, *307*, 269-276.

4.43) Willicut, R. J.; McCarley, R. L. *Adv. Mater.* **1995**, *7*, 759-762.

4.44) Chidsey, C. E.; Bertozzi, C. R.; Putvinsky, T. M.; Mujsce, A. M. *J. Am. Chem. Soc.* **1990**, *112*, 4301-4306.

4.45) Creager, S. E.; Rowe, G. K. *Anal. Chim. Acta* **1991**, *246*, 233-239.

4.46) Green, J.-B. D.; McDermott, M. T.; Porter, M. D. *J. Phys. Chem.* **1995**, *99*, 10960-10965.

4.47) Noy A., F. C. D., Rozsnyai L. F., Wrighton M. S., Lieber C. M. *J. Am. Chem. Soc.* **1995**, *117*, 7943-7951.

4.48) Frisbie, C. D.; Rozsnyai, L. F.; Noy, A.; Wrighton, M. S.; Lieber, C. M. *Science* **1994**, *265*, 2071-2074.

4.49) Duwez, A., -S.; Yu, L. M.; Riga, J.; Pireaux, J.-J.; Delhalle, J. *Thin Solid Films* **1998**, *327-329*, 156-160.

4.50) Beardmore, K. M.; Kress, J. D.; Gronbech-Jensen, N.; R., B. A. *Chem. Phys. Lett.* **1998**, *286*, 40-45.

4.51) Kluth, G. J.; Carraro, C.; Maboudian, R. *Phys. Rev. B* **1999**, *59*, R10449-R10452.

4.52) Nuzzo, R. G.; Zegarski, B. R.; Dubois, L. H. *J. Am. Chem. Soc.* **1987**, *109*, 733-740.

4.53) Dubois, L. H.; Zegarski, B. R.; Nuzzo, R. G. *J. Chem. Phys.* **1993**, *98*, 678-688.

4.54) Laibinis, P. E.; Nuzzo, R. G.; Whitesides, G. M. *J. Phys. Chem.* **1992**, *96*, 5097-5105.

4.55) Shi, J.; Hong, B.; Parokh, A. N.; Collins, R. W.; Allara, D. L. *Chem. Phys. Lett.* **1995**, *246*, 90-94.

4.56) van Patten, P. G.; Noll, J. D.; Myrick, M. L. *J. Phys. Chem. B* **1997**, *101*, 7874-7875.

4.57) Schonenberger, C.; Jorritsima, J.; Sondag-Huethorst, J. A. M.; Fokkink, L. G. J. *J. phys. Chem.* **1995**, *99*, 3259-3271.

4.58) Li, T.-W.; Chao, I.; Tao, Y.-T. *J. Phys. Chem. B* **1998**, *102*, 2935-2946.

4.59) Siepmann, J. I.; McDonald, I. R. *Mol. Phys.* **1993**, *79*, 457-473.

4.60) Ron, H.; Rubinstein, I. *Langmuir* **1994**, *10*, 4566-4573.

4.61) Garrell, R. L.; Chadwick, J. E.; Severance, D. L.; McDonald, N. A.; Myles, D. C. *J. Am. Chem. Soc.* **1995**, *117*, 11563-11575.

4.62) Gerdy, J. J.; Goodard III, W. A. *J. Am. Chem. Soc.* **1996**, *118*, 3233-3236.

4.63) Dubois, L. H.; Nuzzo, R. G. *Ann. Rev. Phys. Chem.* **1992**, *43*, 437-463.

4.64) Zharnikov, M.; Frey, S.; Heister, K.; Grunze, M. *Langmuir* **2000**, *16*, 2697-2705.

4.65) Yan, C.; Golzhauser, A.; Grunze, M. *Langmuir* **1999**, *15*, 2414-2419.

4.66) Zharnikov, M.; Frey, S.; Rong, H.; Yang, Y.-J.; Heister, K.; Buck, M.; Grunze, M. *Phys. Chem. Chem. Phys.* **2000**, *2*, 3359-3362.

4.67) Danneberger, O.; Weiss, K.; Himmel, H., -J.; Jager, B.; Buck, M.; Woll, C. *Thin Solid Films* **1997**, *307*, 183-191.

4.68) Hahner, G.; Woll, C.; Buck, M.; Grunze, M. *Langmuir* **1993**, *9*, 1955-1958.

4.69) Rieley, H.; Price, N. J.; White, R. G.; Blyth, R. I. R.; Robinson, A. W. *Surf. Sci.* **1995**, *331-333*, 189-195.

4.70) Gronbeck, H.; A., C.; Andreoni, W. *J. Am. Chem. Soc* **2000**, *122*, 3839-3842.

4.71) Shon, Y.-S.; Lee, T. R. *J. Phys. Chem. B* **2000**, *104*, 8182-8191.

4.72) Vondrak, T.; Wang, H.; Winget, P.; Cramer, C. J.; Zhu, X.-Y. *J. Am. Chem. Soc.* **2000**, *122*, 4700-4707.

4.73) Lee, M.-T.; Hsueh, C.-C.; Freund, M. S.; Ferguson, G. S. *Langmuir* **1998**, *14*, 6419-6423.

4.74) Duwez, A.-S.; Yu, L.-M.; Riga, J.; Delhalle, J.; Pireaux, J.-J. *Langmuir* **2000**, *16*, 6569-6576.

4.75) Poirier, G. E. *Chem. Rev.* **1997**, *97*, 1117-1127.

4.76) Fenter, P.; Eberhardt, A.; Eisenberger, P. *Science* **1994**, *266*, 1216-1218.

4.77) Bain, C. D.; Troughton, E. B.; Tao, Y. T.; Evall, J.; Whitesides, G. M.; Nuzzo, R. G. *Journal of the American Chemical Society* **1989**, *111*, 321-335.

4.78) Wirde, M. **1999**.

4.79) Huang, J. Y.; Hemminger, J. C. *J. Am. Chem. Soc.* **1993**, *115*, 3342-3343.

4.80) Zubragel, C.; Schneider, F.; Neumann, M.; Hahner, G.; Woll, C.; Grunze, M. *Chem. Phys. Lett.* **1994**, *219*, 127-131.

4.81) Groat, K. A.; Creager, S. E. *Langmuir* **1993**, *9*, 3668-3675.

4.82) Zhao, X.-M.; Wilbur, J. L.; Whitesides, G. M. *Langmuir* **1996**, *12*, 3257-3264.

4.83) McCarley, T. D.; McCarley, R. L. *Anal. Chem.* **1997**, *69*, 130-136.

4.84) Zamborini, F. P.; Crooks, R. M. *Langmuir* **1997**, *13*, 122-126.

4.85) Arce, F. T.; Vela, M. E.; Salvarezza, R. C.; Arvia, A. J. *J. Chem. Phys.* **1998**, *109*, 5703-5706.

4.86) Ishida, T.; Yamamoto, S.; Mizutani, W.; Motomatsu, M.; Tokumoto, H.; Hokari, H.; Azehara, H.; Fujihira, M. *Langmuir* **1997**, *13*, 3261-3265.

4.87) van Velzen, E. U. T.; Engbersen, J. F. J.; de Lange, P. J.; Mahy, J. W. G.; Reinhoudt, D. N. *J. Am. Chem. Soc.* **1995**, *117*, 6853-6862.

4.88) Peterlinz, K. A.; Georgiadis, R. *J. Phys. Chem. B* **1997**, *101*, 8041-8042.

4.89) Poirier, G. E. *Langmuir* **1997**, *13*, 2019-2026.

4.90) Castner, D. G.; Hinds, K.; Grainger, D. W. *Langmuir* **1996**, *12*, 5083-5086.

4.91) Cavalleri, O.; Hirstein, A.; Kern, K. *Surf. Sci.* **1995**, *340*, L960-L964.

4.92) Schlenoff, J. B.; Li, M.; Ly, H. *J. Am. Chem. Soc.* **1995**, *117*, 12528-12536.

4.93) Shon, Y.-S.; Lee, T. R. *Langmuir* **1999**, *15*, 1136-1140.

4.94) Shon, Y.-S.; Colorado Jr, R.; Williams, C. T.; Bain, C. D.; Lee, T. R. *Langmuir* **2000**, *16*, 541-548.

4.95) Cavalleri, O.; Gilbert, S. E.; Kern, K. *Chem. Phys. Lett.* **1997**, *269*, 479-484.

4.96) Fenter, P.; Eisenberger, P.; Liang, K. S. *Phys. Rev. Lett.* **1993**, *70*, 2447-2450.

4.97) Garg, N.; Friedman, J. M.; Lee, T. R. *Langmuir* **2000**, *16*, 4266-4271.

4.98) Himmelhaus, M.; Eisert, F.; Buck, M.; Grunze, M. *J. phys. Chem. B* **2000**, *104*, 576-584.

4.99) Camillone III, N.; Leung, T. Y. B.; Schwartz, P.; Eisenberger, P.; Scoles, G. *Langmuir* **1996**, *12*, 2737-2746.

4.100) Zhong, C.-J.; Brush, R. C.; Anderegg, J.; Porter, M. D. *Langmuir* **1999**, *15*, 518-525.

4.101) Li, L.; Yu, Q.; Jiang, S. *J. Phys. Chem. B* **1999**, *103*, 8290-8295.

4.102) Zhang, Q.; Huang, H.; He, H.; Chen, H.; Shao, H.; Liu, Z. *Surf. Sci.* **1999**, *440*, 142-150.

4.103) Kobayashi, K.; Horiuchi, T.; Ymada, H.; Matsushidge, K. *Thin Solid Films* **1998**, *331*, 210-215.

4.104) Widrig, C. A.; Alves, C. A.; Porter, M. D. *J. Am. Chem. Soc.* **1991**, *113*, 2805-2810.

4.105) Beulen, M. W. J.; Huisman, B.-H.; van der Heijden, P. A.; van Veggel, F. C. J. M.; Simons, M. G.; Biemond, E. M. E. F.; de Lange, P. J.; Reinhoudt, D. N. *Langmuir* **1996**, *12*, 6170-6172.

4.106) Chidsey, C. E.; Liu, G.-Y.; Rowntree, P.; Scoles, G. *J. Chem. Phys.* **1989**, *91*, 4421-4423.

4.107) Hahner, G.; Kinzler, M.; Thummler, C.; Woll, C.; Grunze, M. *J. Vac. Sci. Technol. A* **1992**, *10*, 2758-2763.

4.108) Fischer, D.; Marti, A.; Hahner, G. *J. Vac. Sci. Technol. A* **1997**, *15*, 2173-2180.

4.109) Tamada, K.; Nagasawa, J.; Nakanishi, F.; Abe, K.; Hara, M.; Knoll, W.; Ishida, T.; Fukushima, H.; Miyashita, S.; Usui, T.; Koini, T.; Lee, T. R. *Thin Solid Films* **1998**, *327-329*, 150-155.

4.110) Rieley, H.; Price, N. J.; Smith, T. L.; Yang, S. *J. Chem. Soc. Faraday Trans.* **1996**, *92*, 3629-3634.

4.111) Fenter, P.; Schreiber, F.; Berman, L.; Scoles, G.; Eisenberger, M. J.; Bedzyck, M. *Surf. Sci.* **1998**, *412/413*, 213.

4.112) Clark, B. K.; Gregory, B. W.; Avila, A.; Cotton, T. M.; Standard, J. M. *J. Phys. Chem. B* **1999**, *103*, 8201.

4.113) Voets, G.; Gerritsen, J. W.; Grimbergen, R. F. P.; van Kempen, H. *Surf. Sci.* **1998**, *399*, 316.

4.114) Laibinis, P. E.; Whitesides, G. M.; Allara, D. L.; Tao, Y.-T.; Parikh, A. N.; Nuzzo, R. G. *J. Am. Chem. Soc.* **1991**, *113*, 7152.

4.115) Camillone III, N.; Eisenberger, P.; Leung, T. Y. B.; Schwartz, P.; Scoles, G.; Poirier, G. E.; Tarlov, M. J. *J. Chem. Phys.* **1994**, *101*, 11031.

4.116) Dhirani, A.; Hines, M. A.; Fisher, A. J.; Ismail, O.; Guyot-Sionnest, P. *Langmuir* **1995**, *11*, 2609.

4.117) Fenter, P.; Eisenberger, P.; Li, J.; Camillone III, N.; Bernasek, S.; Scoles, G.; Ramanarayaman, T. A.; Liang, K. S. *7* **1991**.

4.118) Schwaha, K.; Spencer, N. D.; Lambert, R. M. *Surf. Sci.* **1979**, *81*, 273.

4.119) Cramer, S. P.; Tench, O.; Yocum, M.; George, G. N. *Nucl. Instrum. Meth. A* **1988**, *266*, 586.

Chapter 5. Cu(0) Nanoclusters Derived from Poly(propylene imine) Dendrimer Complexes of Cu(II)

5.1. Experimental Details

5.1.1. Preparation of DAB-Am_n-$Cu(II)_x$ Complexes and DAB-Am_n-$Cu(0)_{cluster}$ Nanoparticles

All chemicals were used as received from Aldrich. The DAB-Am_n-$Cu(II)_x$ (n=4, 8, 16, 32, 64; x=n/2) complexes were synthesized in the same manner, as described by Bosman.[1] In order to ensure that the proper stoichiometric ratios were obtained (i.e. a given ratio of Cu(II) to dpt end groups), the requisite amounts of methanolic solutions of $Cu(NO_3)_2 \cdot 2.5\ H_2O$ and the corresponding amine-terminated poly(propylene imine) dendrimer with a diaminobutane core (DAB-Am_n (n=4, 8, 16, 32, 64)) were mixed in order to result in a final Cu(II) concentration of 2 mM. The faint blue $Cu(NO_3)_2$ solution turned to an intense blue upon mixing with the dendrimer solution. The solution was stirred for 30 min. Maintaining a Cu(II) concentration of 2 mM throughout the series of dendrimer generations results in the following, in terms of Cu(II)-dendrimer complex concentration: 1 mM DAB-Am_4-$Cu(II)_2$, 0.5 mM DAB-Am_8-$Cu(II)_4$, 0.25 mM DAB-Am_{16}-$Cu(II)_8$, 0.125 mM DAB-Am_{32}-$Cu(II)_{16}$, and 0.0625 mM DAB-Am_{64}-$Cu(II)_{32}$. Cu nanoparticles were formed by reduction of the DAB-Am_n-$Cu(II)_x$ solutions with a 10 fold excess of $NaBH_4$.[2] The reduction resulted in a color change of the solution from blue to golden brown indicating the formation of nanoclusters, DAB-Am_n-$Cu(0)_{cluster}$. TEM images of DAB-Am_n-$Cu(0)_{cluster}$ were obtained by placing a drop of the solution on a holey-carbon copper grid, and then immediately transferring the sample into vacuum. The DAB-Am_n-$Cu(0)_{cluster}$ samples for EXAFS and XANES were prepared by reduction of the DAB-Am_n-$Cu(II)_x$ solutions. As long as these reduced solution of Cu/dendrimer were kept under inert atmosphere,

no precipitate or change of color was observed. Powders were obtained by vacuum evaporation of the solvent. The resulting powders were transfered under Ar into an oxygen-free glove box where they were placed between Kapton tape. The resulting tape/powder samples were kept in an oxygen-free environment for all analyses.

5.1.2. EXAFS and XANES Measurements

EXAFS and XANES measurements were taken at the Center for Advanced Microstructures and Devices (CAMD) in Baton Rouge, LA. The experiments were performed at the double crystal monochromator (DCM) beamline with a Lemonnier-type monochromator[3] equipped with a pair of Si(400) crystals. The ring was operated at 1.3 or 1.5 GeV with corresponding average ring currents of 140 mA and 100 mA, respectively. At least two scans were taken for the DAB-Am_n-$Cu(II)_x$ (n=4, 8, 16, 32, and 64, $x=n/2$) from 8779 eV to 9779 eV in both fluorescence and transmission mode. The powder samples were kept between two pieces of Kapton tape and no degradation of the samples was observed over time or exposure to radiation. The solution samples were held in a homemade liquid cell with Kapton windows. The fluorescence was measured with a krypton-filled Lytle detector,[4] using a Ni filter and normalized to the incident beam current I_o measured by an ionization chamber placed before the sample. Transmission measurements were taken by monitoring the current in an ionization chamber placed after the sample. Additionally, a copper foil (8979 eV) or copper oxide powder (Cu_2O at 8983.79 eV) were scanned in all measurements for calibration purposes in a third ionization chamber. The calibration was also checked between each sample. The DAB-Am_n-$Cu(0)_{cluster}$ (n=4 to 64), were measured in the transmission mode with Si(311) crystals. Spectra were acquired in the quick-EXAFS mode[5] over the energy range 8800-9900 eV. This instrumentation will be described in detail elsewhere

[6], but is modeled after the apparatus described by Frahm.[5] Briefly, quick-EXAFS entails integrating the motion control with the data acquisition system to facilitate the rapid production of the data sets generated in the course of the typical EXAFS study. The stepper motor stage that drives the monochromator is equipped with an optical encoder that transmits quadrature signals marking angular rotation with a resolution of 1 millidegree. These TTL level signals take the form of pulse trains when the monochromator is rotated. A multifunction data acquisition board that features sampling of analog and TTL inputs allows instrument readings (represented by scaled analog voltages) to be correlated with the concurrent position of the rotating monochromator, as determined from the TTL pulse train. Therefore, minimal real-time processing of the sampled encoder and instrumentation signals provide a fast and accurate measurement of photon flux as a function of photon energy.

Data reduction and analysis involving energy calibration, pre-edge and post-edge background subtraction, edge normalization, conversion to k space and extraction of the EXAFS function $\chi(k)$ were carried out using well established procedures.[7,8] Winxas 97[9] was used for data analysis in conjunction with autobk[10] and feff7.[11]

5.2. DAB-Am$_n$-Cu(II)$_x$ Complexes—Generation-Independent, Square-Based Pyramid Structure Solution Studies.

Normalized, solution-phase, fluorescence mode XANES spectra at the Cu K-edge for the DAB-Am$_n$-Cu(II)$_x$ complexes (n=4, 8, 16, 32, x=n/2) are displayed in Figure 5.1. The XANES spectra in Figure 5.1 support the claim that Cu(II) is the only copper species present, as is demonstrated by the presence of only the expected three major bands for Cu(II).[12-17] In addition, the positions of the spectral features indicate that Cu(II) is bound to nitrogen atoms. Feature B in Figure 5.1 is known to be associated with a copper 1s→ 4p transition with simultaneous shakedown[12,13] and is

apparent in the first derivative spectra, as shown in Figure 2B for DAB-Am_{16}-$Cu(II)_8$. The 1s→4p transition occurs at 8985.5 eV for the entire DAB-Am_n-$Cu(II)_x$ complex series (data not shown), which is typical of Cu(II) complexes.[14]

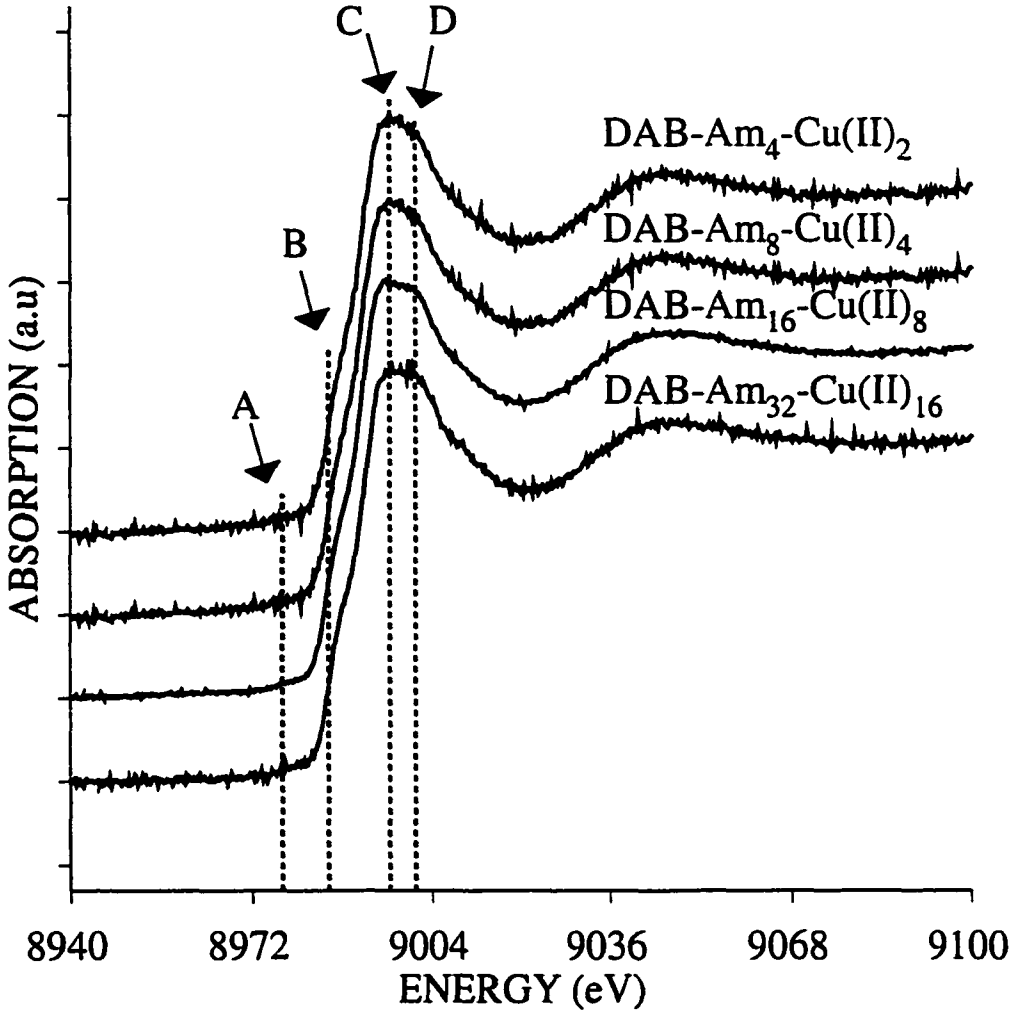

Figure 5.1. Normalized Cu K-edge XANES spectra for the DAB-Am_n-$Cu(II)_x$ (n=4 to 32, x=n/2) complexes in CH_3OH solution.

The spectra in Figures 5.1 and 5.2 point to the lack of any uncoordinated Cu(II), as observed upon comparison of the spectra for the DAB-Am_n-$Cu(II)_x$ complexes with those of $Cu(NO_3)_2$.[14,17-26] In addition, features C and D further support the +2 oxidation state of copper in the complexes. The 8996.4 eV value for the transition

associated with feature C is routinely observed in the XANES spectra of Cu(II)–ligand complexes containing Cu–N bonds and has been described to be caused by a larger degree of covalency between the Cu(II) and equatorial ligands.[14] In addition, feature D is observed at 9001 eV for all generations and is typical of nitrogen-bonded Cu(II) ions.[16,17]

A slight increase in the intensity of feature D, in comparison to the other spectral features, is observed when moving from dendrimer generation 1 to 4, Figure 5.1.

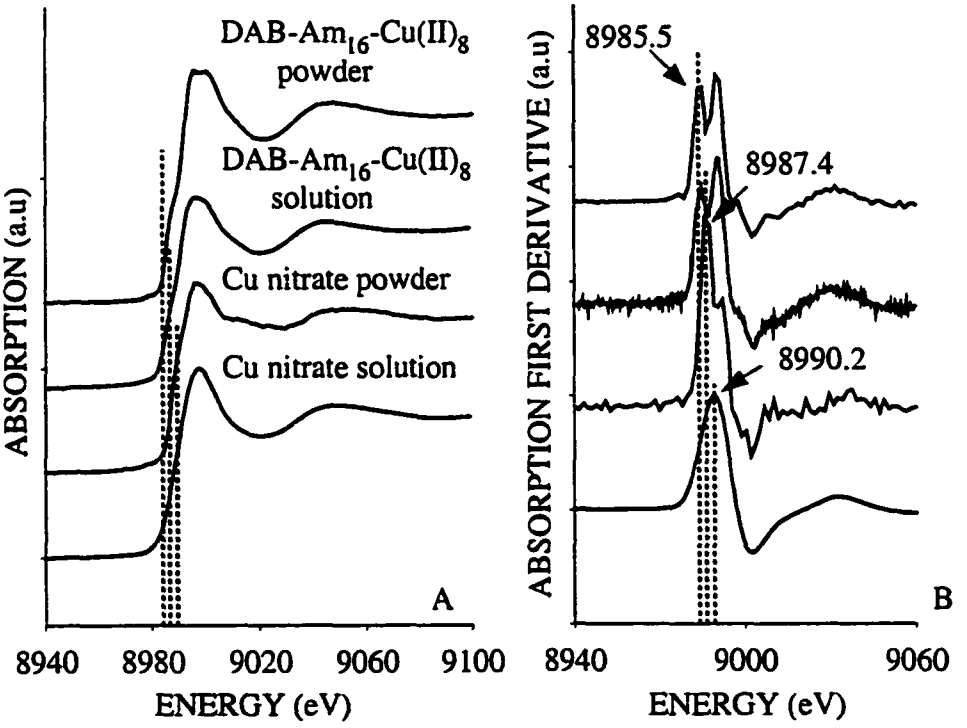

Figure 5.2. A. Comparison of the normalized Cu K-edge spectra for the DAB-Am_{16}-$Cu(II)_8$ and $Cu(NO_3)_2$ (solid state and solution). B. Derivative of the corresponding XANES spectra. The reference lines point at the position of Feature B in Figure 5.1.

We attribute this intensity increase for feature D to an increase in the degree of covalency of the Cu–N bond as a result of a distortion of the copper-dendrimer complex, possibly caused by increased steric crowding of the Cu(II)-dendrimer complexes with increased dendrimer generation. This distortion is further supported by the presence of feature A at 8977.3 eV in the solution and solid-state (Figure 5.2 A) XANES spectra. The position of spectral feature A is consistent with the electric dipole forbidden 1s→3d transition[27] associated with a variety of distorted Cu(II)–N complexes.[12,14,28,29]

The electronic (UV/vis) spectra of the DAB-Am$_n$-Cu(II)$_x$ complexes in methanol (MeOH) are virtually indistinguishable and consist of a d-d band (Figure 5.3) near 630 nm.[1,30] Observation of this transition is consistent with trigonal bipyramidal and square-based pyramidal geometries for Cu(II) complexes.[30,31] Electron paramagnetic resonance (EPR) data obtained by Bosman[1,31] for DAB-Am$_n$-Cu(II)$_x$ indicate that the latter case is more likely.[32]

5.3. Studies of DAB-Am$_n$-Cu(II)$_x$ in the Solid State

X-ray spectroscopy experiments with DAB-Am$_n$-Cu(II)$_x$ solids were undertaken in order to obtain high quality (high signal-to-noise ratio) spectra that could be used to accurately determine the structure of the Cu(II)-dendrimer complexes.[33] Free-flowing "baby blue" DAB-Am$_n$-Cu(II)$_x$ powders were obtained for n=1–5 by vacuum evaporation of the MeOH solvent. Representative XANES spectra for all Cu(II)-dendrimer complexes are displayed in Figure 5.4. In general, the solid-state spectra are almost identical to the solution-phase spectra (cf. solution and powder spectra for n=16 in Figure 2A), with the differences being associated solely with the intensities of features A and D.

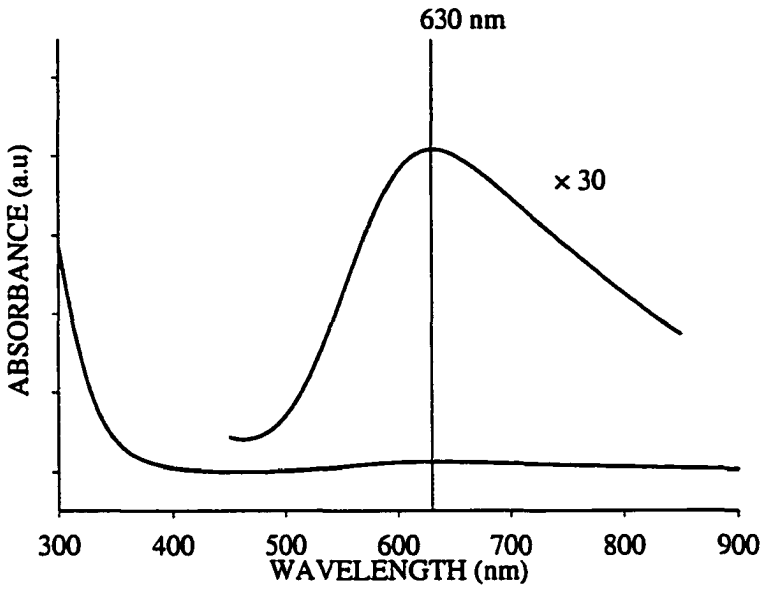

Figure 5.3. UV-vis spectrum of Dab-Am_{32}-$Cu(II)_{16}$ in methanol

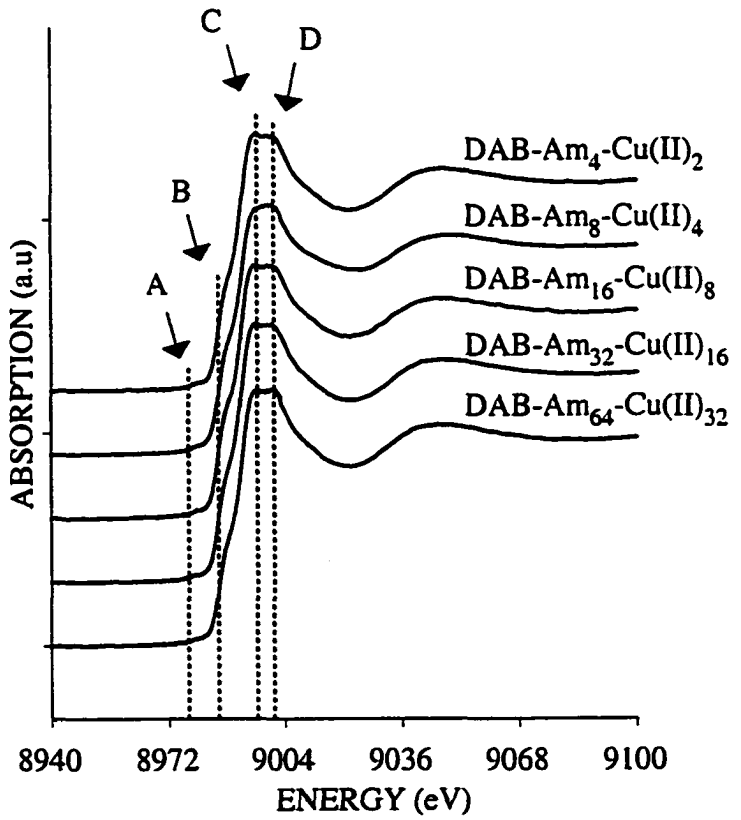

Figure 5.4. Normalized Cu K-edge XANES spectra for DAB-Am_n-$Cu(II)_x$ (n=4 to 64, x=n/2) complexes in the solid state.

As discussed above for the solution-phase spectra, features A and D arise when the geometry of Cu(II)-ligand complexes is distorted.[14,28,29] Thus, the Cu(II)-dendrimer complexes in the solid state have a structure with a higher degree of distortion than when in solution, albeit only slightly more distorted. It can be concluded that the Cu oxidation state and overall structure of the DAB-Am_n-$Cu(II)_x$ materials around the Cu ions is virtually the same when the Cu-dendrimer complexes are in the solid state or in MeOH solution.

Analysis of the EXAFS data provides a means of determining bond distances and coordination numbers for Cu(II) in the DAB-Am_n-$Cu(II)_x$ materials, and can be utilized to identify the nearest neighbors to Cu(II). Previous studies involving comparison of EPR data for DAB-Am_n-$Cu(II)_x$ complexes with that for a N, N, N', N'-tetrakis (3-aminopropyl)-1,5-diamino-3-oxapentane di-Cu(II) complex suggest that Cu(II) is most likely coordinated to two primary amines, one tertiary amine, and two other ligands (such as MeOH or H_2O) in the DAB-Am_n-$Cu(II)_x$ complexes.[1,34] Due to the similarity of the atomic weight, size and electronic configuration of oxygen and nitrogen, their backscattering functions are sometimes difficult to differentiate and could lead to ambiguities in assignment of ligand identity. However, it is possible to overcome this challenge by comparing the experimental EXAFS data to simulated EXAFS data generated using all possible combinations of O and N atoms coordinated to Cu(II).

The Fourier transforms of the EXAFS function (experimental–solid lines) and the calculated fits using Feff7[11,35] (dotted lines) are shown in Figure 5.5 for the five DAB-Am_n-$Cu(II)_x$ complexes. Table 5.1 lists the coordination numbers and bond distances obtained from the curve fitting procedure.

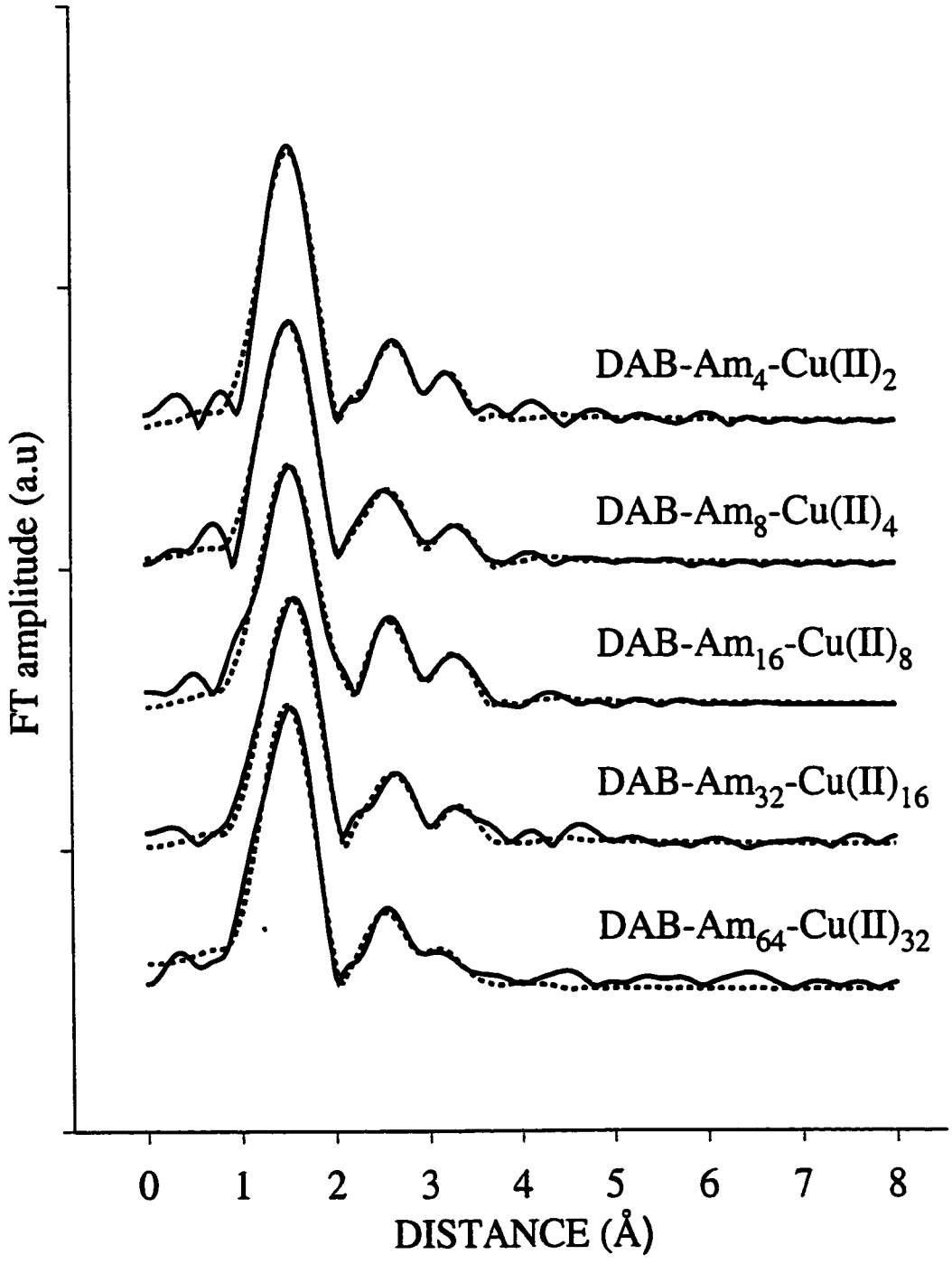

Figure 5.5. Fourier transforms of the EXAFS function for the DAB-Am$_n$-Cu(II)$_x$ (n=4 to 64, x=n/2, 4, 8, 16, 32) complexes in the solid state. Experimental data (solid line) and calculated fits (dashed line) are shown.

Table 5.1. EXAFS parameters obtained from curve fitting analysis for the DAB-Am_n-$Cu(II)_x$ (n=4 to 64, x=n/2) complexes.

Sample	Element	Coordination Number	Bond distance (Å)	Debye-Waller factor σ^2
DAB-Am_4-$Cu(II)_2$	N, O	4	1.99	0.0071
	O	1	2.67	0.0118
	C	3	3.03	0.0062
	Cu	1	3.36	0.0078
DAB-Am_8-$Cu(II)_4$	N, O	4	2.00	0.0089
	O	1	2.64	0.0125
	C	3	3.00	0.0065
	Cu	1	3.50	0.0107
DAB-Am_{16}-$Cu(II)_8$	N, O	4	1.99	0.0089
	O	1	2.60	0.0168
	C	3	2.99	0.0078
	Cu	1	3.45	0.0082
DAB-Am_{32}-$Cu(II)_{16}$	N, O	4	2.01	0.0081
	O	1	2.68	0.0146
	C	3	3.03	0.0083
	Cu	1	3.47	0.0109
DAB-Am_{64}-$Cu(II)_{32}$	N, O	4	2.00	0.0087
	O	1	2.61	0.0104
	C	3	3.01	0.0067
	Cu	1	3.42	0.0107

The shape of the Fourier transform data is reminiscent of that obtained for Cu(II) complexes having one or two axial oxygen ligands;[36-40] the fits of the Fourier transform data and previous literature[23] allow us to clearly identify one axial O atom at about 2.6 Å away from the Cu(II). As determined from the data in Figure 5.5, the first coordination shell contains a combination of four nitrogen and/or oxygen atoms in the equatorial plane of the complex. But, the Cu-ligand atom bond distances obtained (1.99 Å) are higher than those for known oxygen-coordinated Cu(II) complexes (typical bond distances between 1.85 and 1.96 Å), indicating that the atoms in the equatorial plane are most likely not oxygen but nitrogen.[25]

In order to identify the ligand atoms in the equatorial plane, the first coordination peak centered at 1.6 Å in the Fourier transform data (without phase-shift correction) that corresponds to the contribution of the four equatorial atoms (see Figure 5.6) was back transformed to k space.

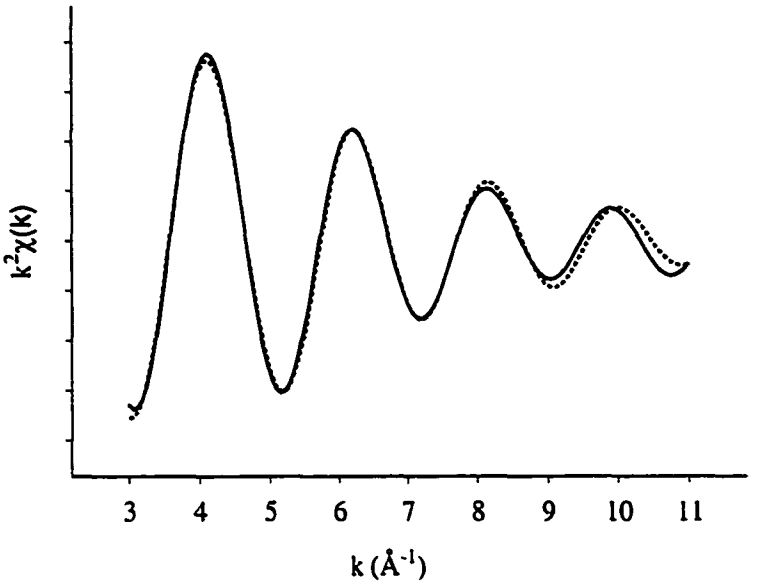

Figure 5.6. Example of the best fit of the Fourier back-transform of the first coordination peak in Figure 4 for the DAB-Am_{32}-$Cu(II)_{16}$. Bond distances and coordination numbers for the DAB-Am_n-$Cu(II)_x$ (n=4 to 64, x=n/2) series are listed in Table 5.2.

Table 5.2. Bond distances and coordination numbers obtained from fitting of the Fourier back-transform of the first coordination peak in Figure 5.5 for the DAB-Am_n-$Cu(II)_x$ (n=4 to 64, x=n/2) series.

	1 O (Å)	3 N (Å)
DAB-Am_4-$Cu(II)_2$	1.92	2.02
DAB-Am_8-$Cu(II)_4$	1.95	2.02
DAB-Am_{16}-$Cu(II)_8$	1.96	2.03
DAB-Am_{32}-$Cu(II)_{16}$	1.96	2.04
DAB-Am_{64}-$Cu(II)_{32}$	1.92	2.04

Then, the k space data was fitted using standard procedures.[11,35] The best fit to the experimental data was obtained through the use of a model with 3 nitrogen atoms and 1 oxygen atom in the equatorial plane.[41,42] Similar results were obtained for the other DAB-Am_n-Cu(II)$_x$ complexes, Table 5.2. The bond distances obtained are typical of Cu–O at 1.92 Å and Cu–N at 2.03 Å.[15,17,25,38,40,43]

The results from this analysis strongly support a structure which has the Cu(II) surrounded by three nitrogen atoms in the equatorial plane and an oxygen atom at 1.92 Å at the base of the pyramid. An axial oxygen atom at approximately 2.6 Å completes the square-based pyramid. The oxygen atoms in the equatorial plane and the axial position could be associated with the methanol solvent, nitrate anions, or water; we are currently unable to further delineate the structure of the Cu complex. A representation of the Cu(II)-dendrimer end-group structure is shown schematically in Figure 5.7 for DAB-Am_{16}-Cu(II)$_8$.

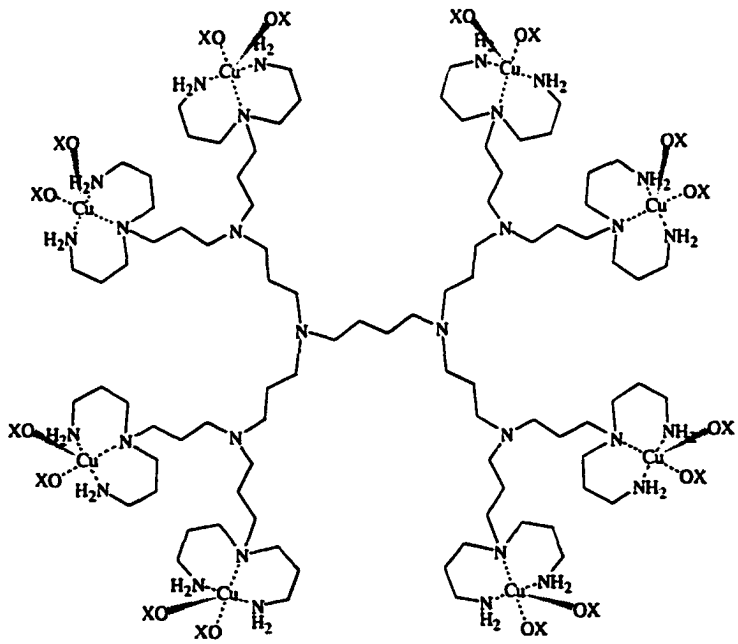

Figure 5.7. Representation of the DAB-Am_{16}-Cu(II)$_8$ complex.

5.4. Reduction of the DAB-Am_n-$Cu(II)_x$ Complexes and Structural Evaluation of the Resulting Cu(0) Nanocluster-Dendrimer Composites

Samples obtained from reduction of DAB-Am_n-$Cu(II)_x$ (n=4 to 64, x=n/2) with a fixed concentration of Cu(II) have been investigated. The preparation of the reduced materials is summarized below. The requisite amount of a given generation dendrimer solution was added to a MeOH solution containing 2 mM $Cu(NO_3)_2 \cdot 2.5\ H_2O$ to maintain the primary amine-Cu(II) ratio at 2:1 for all generations (no excess Cu(II) in solution). This procedure results in Cu(II)-dendrimer solutions that contain a fixed concentration of Cu(II) but a varying concentration of dendrimer (1 mM to 0.0625 mM). Upon reduction of DAB-Am_n-$Cu(II)_x$ complexes with methanolic $NaBH_4$, a golden brown solution resulted. UV-vis spectra did not reveal the presence of any remaining DAB-Am_n-$Cu(II)_x$, as noted by the lack of the characteristic d-d band for the Cu(II) species (Figure 5.8) at 630 nm[1,30] and Cu(II) signal in the XANES spectra, vide infra.

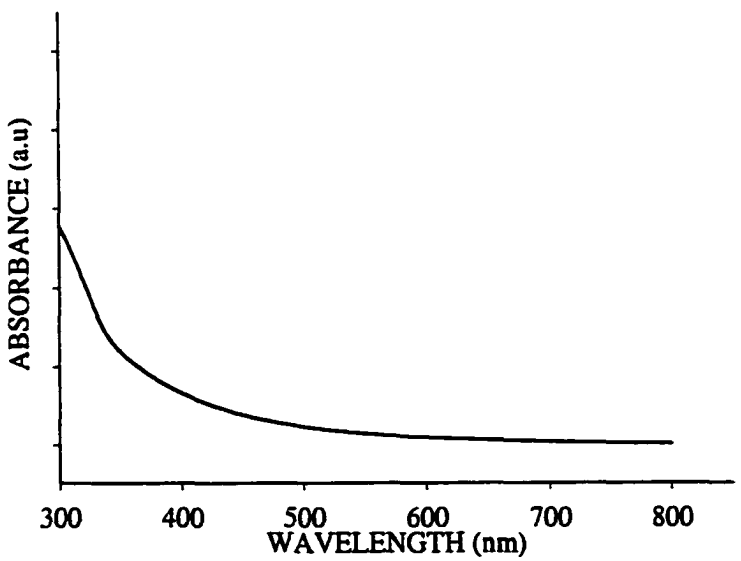

Figure 5.8. UV-vis spectrum of Dab-Am_{32}-$Cu(0)_{cluster}$ in methanol

When stored under an inert atmosphere, these solutions were stable (no precipitates or color changes) for a minimum of 3 days, the longest time evaluated. Brown powders were obtained from these solutions by vacuum removal of solvent; the solids were stored and handled under an inert atmosphere at all times.

The EXAFS spectra for powders obtained as described above are displayed and compared to that of a 7.5 μm-thick copper foil in Figure 5.9.

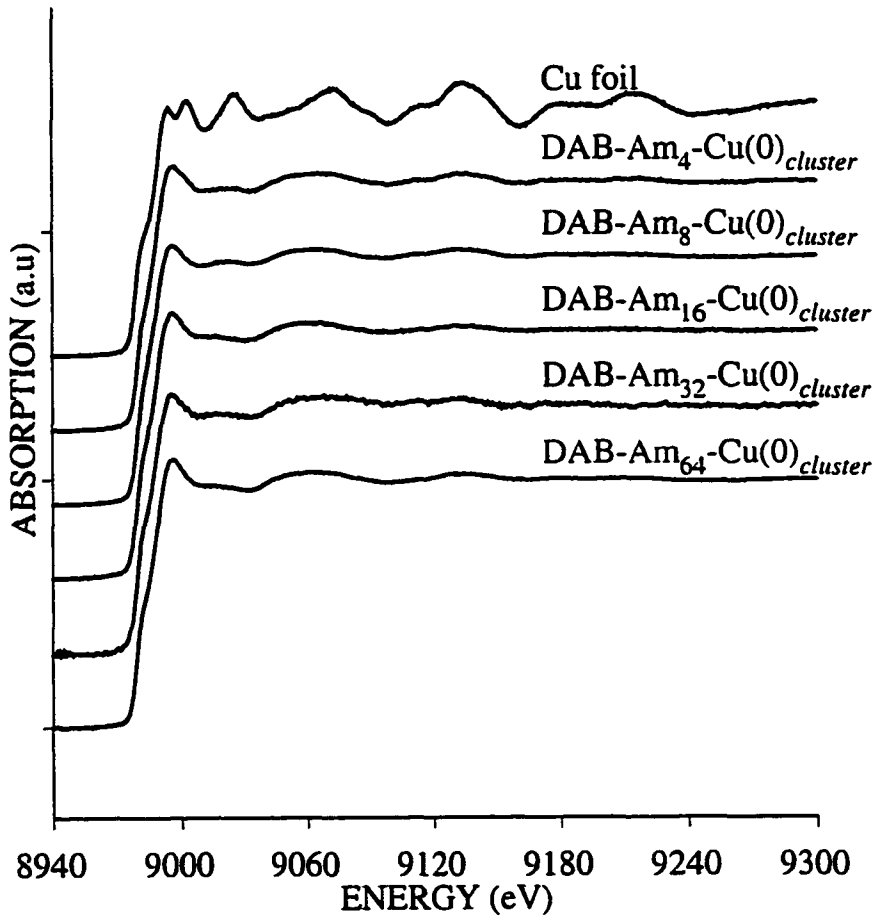

Figure 5.9. EXAFS spectra (8940-9300 eV displayed) of the reduced DAB-Am_n-$Cu(II)_x$ (n=4 to 64, x=n/2) complexes and Cu foil.

The similarities between the spectra of the reduced DAB-Am_n-Cu(II)$_x$ complexes and that of the copper foil are striking and demonstrate the existence of metallic Cu(0) domains in the reduced DAB-Am_n-Cu(II)$_x$, denoted as DAB-Am_n-Cu(0)$_{cluster}$. The position of the K-edge threshold for all of the DAB-Am_n- Cu(0)$_{cluster}$ materials is 1.4 eV higher in energy than that of the pure fcc metal at 8979 eV. This shift in K-edge threshold is characteristic of Cu(0) nanoclusters,[44] thus pointing to their presence in the reduced dendrimer complexes. Furthermore, the amplitudes of the EXAFS features are strongly decreased when compared to those of the fcc copper reference foil, as is expected for Cu(0) nanoclusters.[44] Finally, the presence of nanoclusters is corroborated by UV-vis data. The electronic spectra obtained are characteristic of Cu(0) nanoclusters,[45-49] as noted by the presence of a monotonical increase in the absorbance with increasing energy. Absence of a plasmon band near 550 nm in the UV-vis spectra indicates that the diameter of the nanoclusters is less than 5 nm for all DAB-Am_n-Cu(0)$_{cluster}$ studied.[45-49]

Changes in the X-ray absorption spectra as a function of increasing dendrimer generation indicate a decrease in the size of the Cu(0) nanoclusters with increased dendrimer generation, Figure 5.9. The amplitude of the post-edge features (>9000 eV) in the spectra is found to decrease with increasing dendrimer generation. Such a decrease in spectral amplitude can be correlated to an increase of the surface to volume ratio of nanoclusters,[44,50] which points to a decrease in the average Cu(0) nanocluster size with increased size of the dendrimer.

The Fourier transform of the EXAFS function was obtained for each generation of DAB-Am_n-Cu(0)$_{cluster}$; representative spectra are displayed in Figure 5.10 for the DAB-Am_n-Cu(0)$_{cluster}$ series.

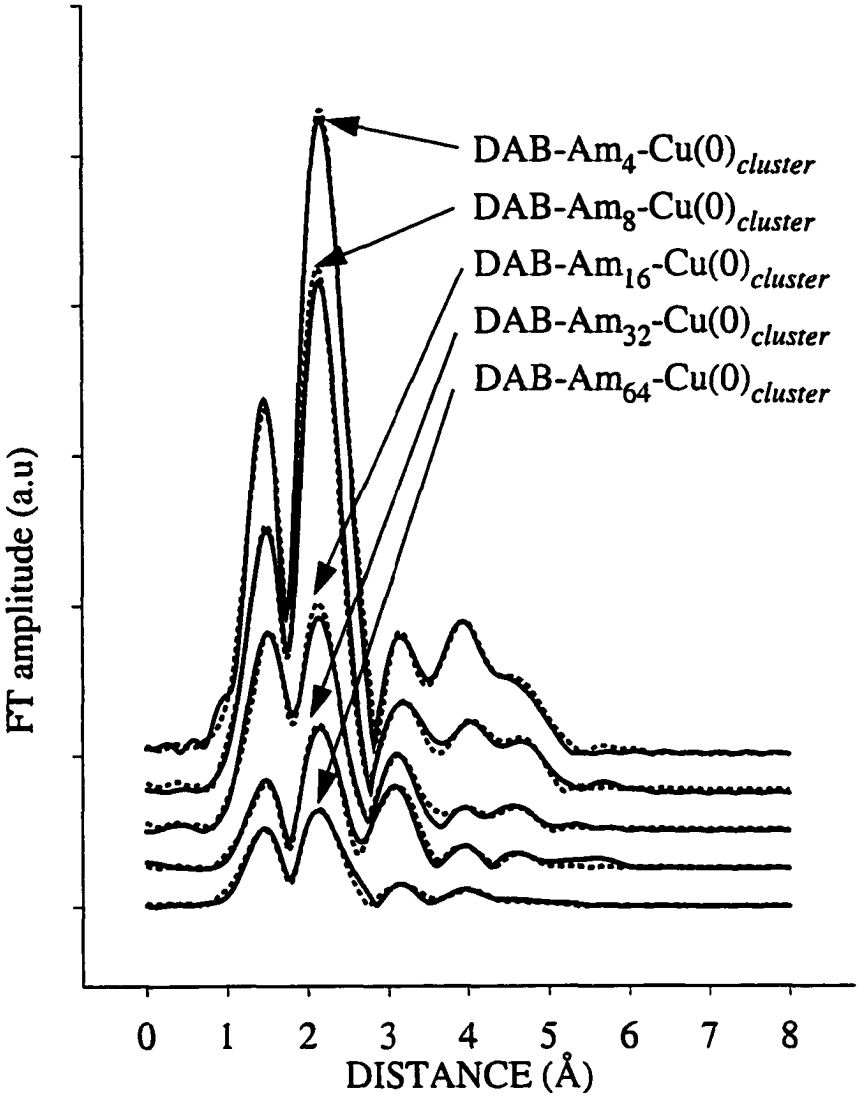

Figure 5.10. Fourier transforms of the EXAFS function for the reduced DAB-Am_n-Cu(II)$_x$ (n=4 to 64, x=n/2) complexes. Experimental data (solid line) and calculated fits (dashed line) are shown.

Table 5.3 lists the EXAFS parameters[11] for the successive copper shells of the nanoclusters in the DAB$_n$–Cu(0)$_{cluster}$ series. The Debye-Waller factors used in the fitting protocol are those determined from previous studies of Cu(0) nanoparticles.[51] Care must be exercised to keep the Debye-Waller factors physically reasonable, or one can obtain improbable coordination numbers. However, the analysis used for the

present data was checked in several ways. While the use of other Debye-Waller factors,[52,53] including values for bulk Cu(0), leads to variations in the coordination numbers and sizes of the nanoclusters, all approaches tested yield a trend of decreased coordination number, first coordination shell bond distance, and nanocluster size with increased dendrimer generation.

Table 5.3. EXAFS parameters obtained from curve fitting analysis for the reduced DAB-Am$_n$-Cu(II)$_x$ (n=4 to 64, x=n/2) complexes and Cu foil.

Sample	Element coordination shell	Coordination Number	Bond distance (Å)	Debye-Waller factor σ^2
Cu foil	Cu_1	12	2.55	0.0096
	Cu_2	6	3.62	0.0147
	Cu_3	24	4.43	0.0175
	Cu_4	9	5.02	0.0103
DAB-Am$_4$-Cu(0)$_{cluster}$	Cu_1	2.1	2.52	0.0095
	Cu_2	1.1	3.54	0.0110
	Cu_3	2.9	4.41	0.0140
	Cu_4	1.6	4.96	0.0120
DAB-Am$_8$-Cu(0)$_{cluster}$	Cu_1	1.6	2.50	0.0098
	Cu_2	0.9	3.51	0.0125
	Cu_3	1.9	4.42	0.0170
	Cu_4	1.5	4.96	0.0140
DAB-Am$_{16}$-Cu(0)$_{cluster}$	Cu_1	0.8	2.50	0.0110
	Cu_2	0.4	3.48	0.0065
	Cu_3	0.9	4.40	0.0220
	Cu_4	0.9	4.86	0.0180
DAB-Am$_{32}$-Cu(0)$_{cluster}$	Cu_1	0.5	2.50	0.0109
	Cu_2	0.3	3.47	0.0040
	Cu_3	1.2	4.44	0.0200
	Cu_4	0.5	4.84	0.0140
DAB-Am$_{64}$-Cu(0)$_{cluster}$	Cu_1	0.4	2.50	0.0120
	Cu_2	0.2	3.51	0.0115
	Cu_3	0.6	4.47	0.0160
	Cu_4	0.4	5.00	0.0140

As has been shown previously, the observed contraction of the first coordination shell Cu-Cu bond distance has been correlated to a decrease in cluster size.[44,52,54] In this work by Montano,[44] Apai,[54] and Gota[52] it was demonstrated that the size of Cu nanoclusters can be estimated by examination of the first coordination shell Cu-Cu bond distance and the coordination numbers of the successive copper shells.[55] The average Cu-Cu bond distance of the first copper shell obtained for our samples (for example, 2.53 Å for DAB-Am_4-$Cu(0)_{cluster}$), is very close to that of fcc Cu (2.55 Å) and is found to slightly decrease with increasing generation, reaching 2.50 Å for DAB-Am_{64}-$Cu(0)_{cluster}$. By comparing the bond distances of the first coordination shell Cu-Cu bond distance determined in this study with data from Apai et al.,[54] we estimate a diameter of roughly 4 nm for DAB-Am_4-$Cu(0)_{cluster}$, and 1.5 nm for DAB-Am_{64}-$Cu(0)_{cluster}$, thus confirming the suggested decrease in cluster size with increase in dendrimer generation (decreased amplitude of the post-edge features, vide supra). In addition, the ratio of the coordination numbers of one copper shell to the others for a given cluster-dendrimer complex agrees well with the corresponding ratio for bulk fcc Cu(0), Table 5.3.

The low coordination numbers that are reported in Table 5.3 for the third and fourth Cu coordination shells could be the result of the presence of small defects caused by a film (copper oxide or dendrimer) on the cluster surface. This hypothesis is substantiated by the presence of an additional peak at ~1.6 Å (without phase shift correction) in the Fourier transforms of all the samples. This peak could arise from a layer of copper oxide at the surface,[56] but its position is also consistent with the binding of nitrogen atoms from the dendrimer to the copper atoms of the cluster surface.[57,58] Although it is difficult to differentiate between nitrogen and oxygen solely on their backscattering properties, a Cu_2O oxide layer on the surface of the cluster would

generate a peak in the Fourier transform at about 2.3 Å (without phase shift correction),[56] which is not the case for any of the DAB_n–$Cu(0)_{cluster}$ materials. Thus, these observations are consistent with the presence of dendrimers adsorbed on the Cu(0) nanocluster surface through nitrogen functionalities.

Transmission electron microscopy (TEM) images obtained for nanoclusters made by reduction of DAB-Am_n-$Cu(II)_x$ (n=4 to 64, x=n/2) complexes are displayed in Figure 5.11. Electron diffraction patterns were also obtained for each sample (not shown); the diffractograms indicate a predominant fcc structure, thereby corroborating the EXAFS data. The size distributions (based on cluster diameter) for all of the DAB-Am_n-$Cu(0)_{cluster}$ are displayed in Figure 5.12 and demonstrate that the dispersity in size of the Cu(0) nanoclusters is quite low. Furthermore, the TEM images demonstrate a decrease in size of the nanoclusters with increasing dendrimer generation, as indicated by the EXAFS studies.

The decrease in Cu(0) nanocluster size with increasing dendrimer generation indicates that the size and possibly the location of the nanoclusters with respect to the dendrimer interior is a function of a property associated with the dendrimer and/or the Cu(0) clusters. We address the location of the Cu(0) nanoclusters first by postulating that the Cu(0) nanoclusters are coated with a layer of dendrimer in the case of the low generation dendrimers, but the smaller nanoclusters generated from the larger dendrimers are stabilized by being encapsulated inside the dendrimers, coated by the dendrimers, or a combination of the two. From simple geometric considerations, the DAB-Am_4 (diameter of ~0.8 nm) cannot contain the Cu(0) clusters (diameter of 3.7 nm). However, we do not observe precipitation of material from solutions of any DAB-Am_n-$Cu(0)_{cluster}$ material.

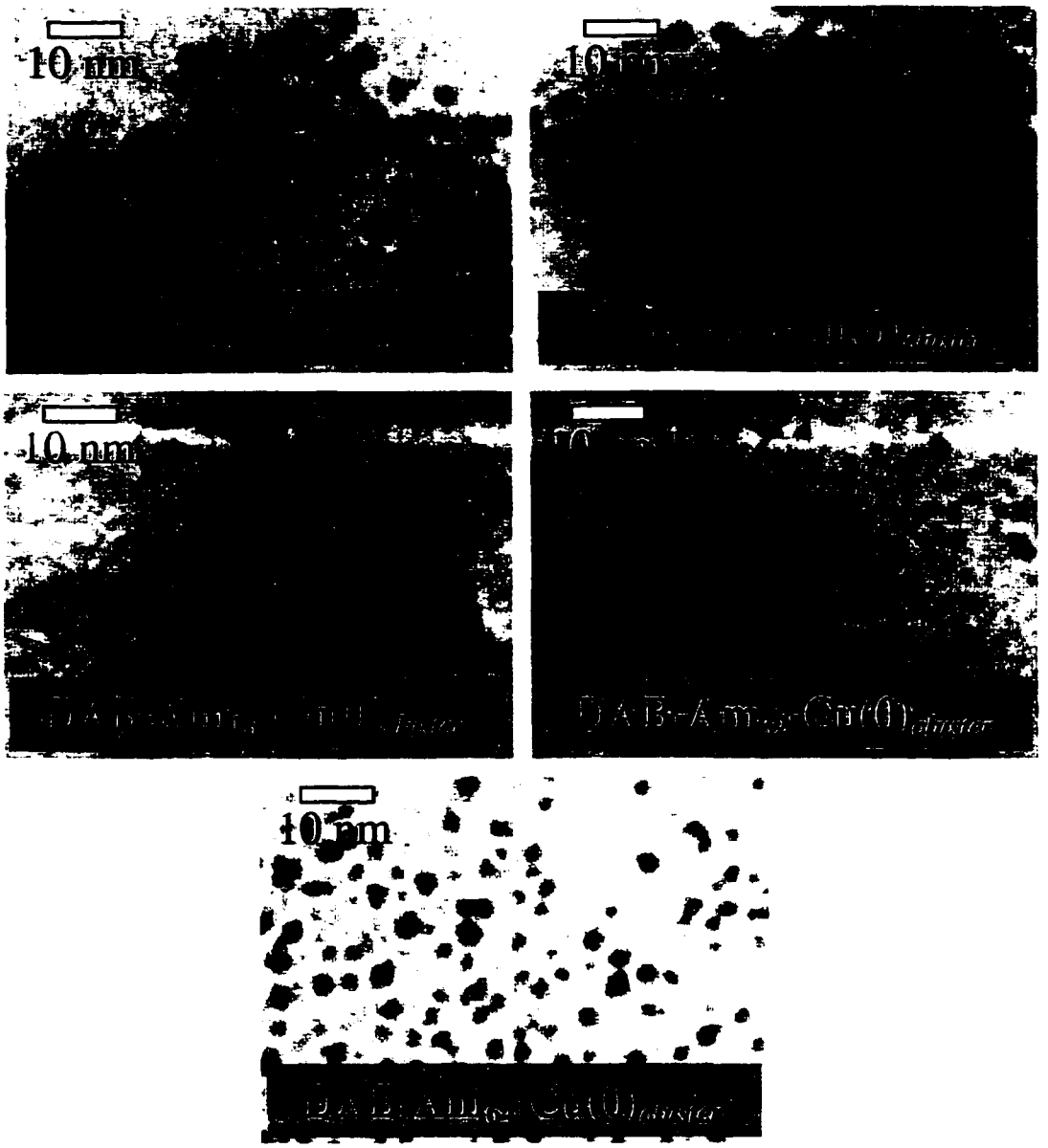

Figure 5.11. TEM images of copper nanoclusters obtained by reduction of the DAB-Am$_n$-Cu(II)$_x$ (n=4 to 64, x=n/2).

Thus, the resulting DAB-Am$_4$-Cu(0)$_{cluster}$ composite is most likely one in which the resulting cluster is coated with a large number of DAB-Am$_4$ dendrimers that act to stabilize the Cu(0) cluster. A similar argument can be made for protection of the Cu(0) nanoclusters by the n=8-16 materials. Only in the case of the n=64 dendrimer (diameter

of roughly 2.4 nm) is it possible to have some degree of encapsulation of the Cu clusters (diameter ~2 nm).

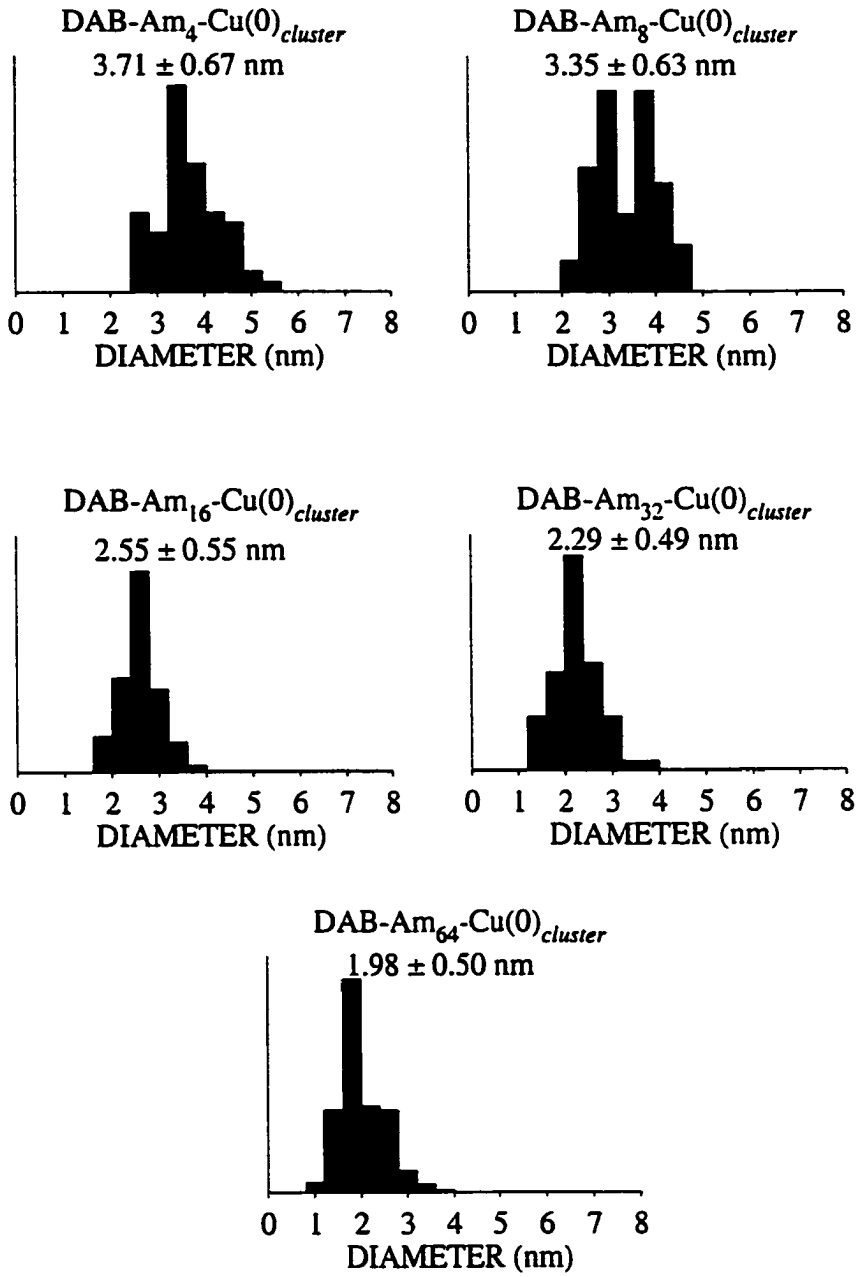

Figure 5.12. Size distribution of the DAB-Am$_n$-Cu(0)$_{cluster}$ (n=4 to 64), [Cu(II)]=2mM. (measured over ≈ 200 particles)

We propose that the observed decrease in Cu(0) nanocluster size with increasing dendrimer generation is the result of steric interactions between dendrimers adsorbed on nascent Cu(0) nanoclusters or dendrimers containing the incipient Cu(0) nanoclusters. Immediately upon reduction, the newly formed Cu(0) atoms near the periphery of the dendrimer can either diffuse into the interior of the dendrimer or be captured at the periphery of the dendrimer. In either case, the Cu(0) atoms diffuse until they encounter other atoms and then form a nucleus/cluster. The nucleus/cluster then will continue to grow only if the interaction between the dendrimer and Cu(0) species is sufficient. If the nucleus/cluster is effectively encapsulated inside the dendrimer, then the resulting cluster will grow and eventually emerge from the dendrimer when it is too large to be contained. Further growth would then be retarded by adsorbed dendrimer, which should be slower in the case of the larger dendrimers due to the larger coating thickness on the Cu clusters. In the case of nucleus/cluster formation at the periphery of the dendrimer, cluster growth will be inhibited by similar steric interactions, yielding a similar trend between the size of the final nanocluster and the dendrimer size.

Significant decreases in the Cu(0) cluster size and size dispersity can be obtained by varying the ratio of primary amines to Cu(II) ions in the dendrimer precursor. This was achieved through the use of "half-functionalized" materials, such as DAB-Am_{64}-$Cu(II)_{16}$, where the ratio of primary amine groups to copper atoms in the nanocluster precursor is increased from 2:1 to 4:1. Upon reduction, nanoclusters with sizes of 1.60 ± 0.31 nm were obtained, see Figure 5.13. This result is not due to a mere decrease in the concentration of Cu(II) in the solution, as indicated by TEM data for clusters formed from DAB-Am_n-$Cu(II)_x$, $x=n/2$, solutions that were two-fold lower in

total Cu(II)-dendrimer concentration (Figure 5.14). Further studies aimed at controlling the size of Cu(0) clusters by varying the ratio of amine groups to Cu(II) are underway.

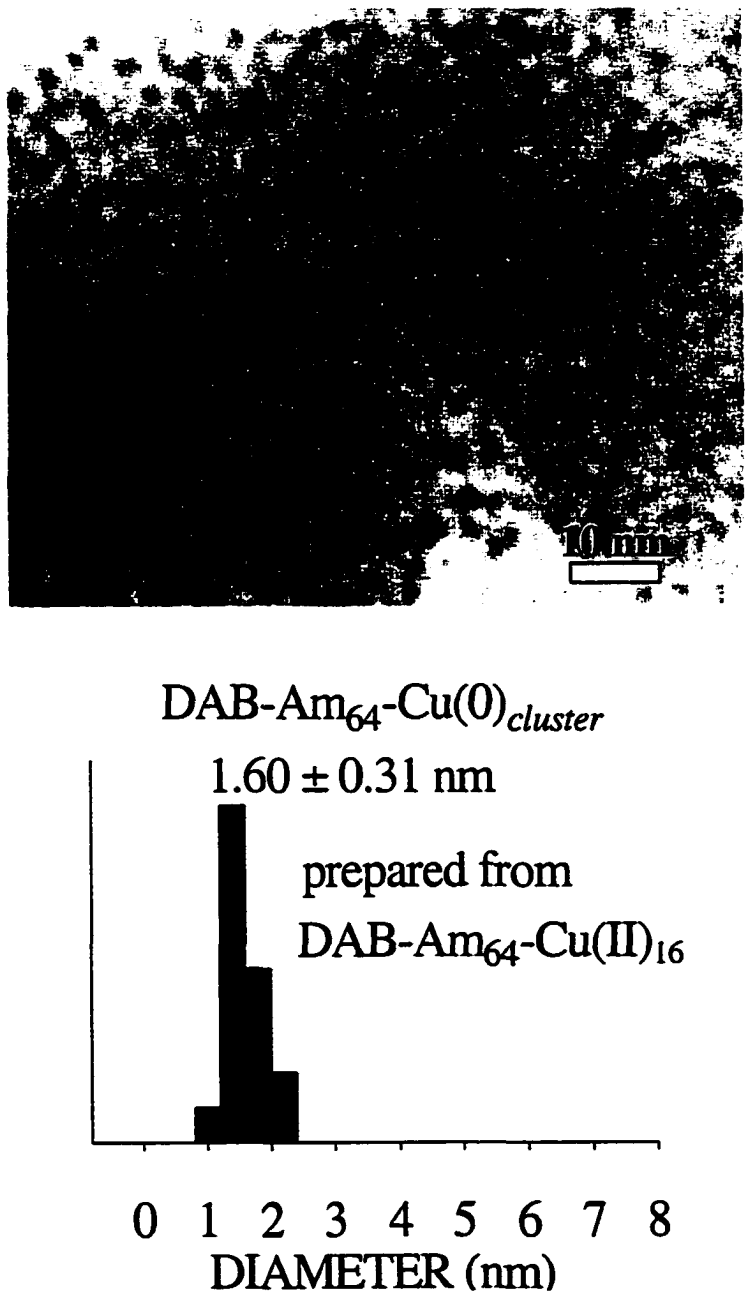

Figure 5.13. TEM image and size distribution of the nanoclusters made from DAB-Am_{64}-$Cu(II)_{16}$.

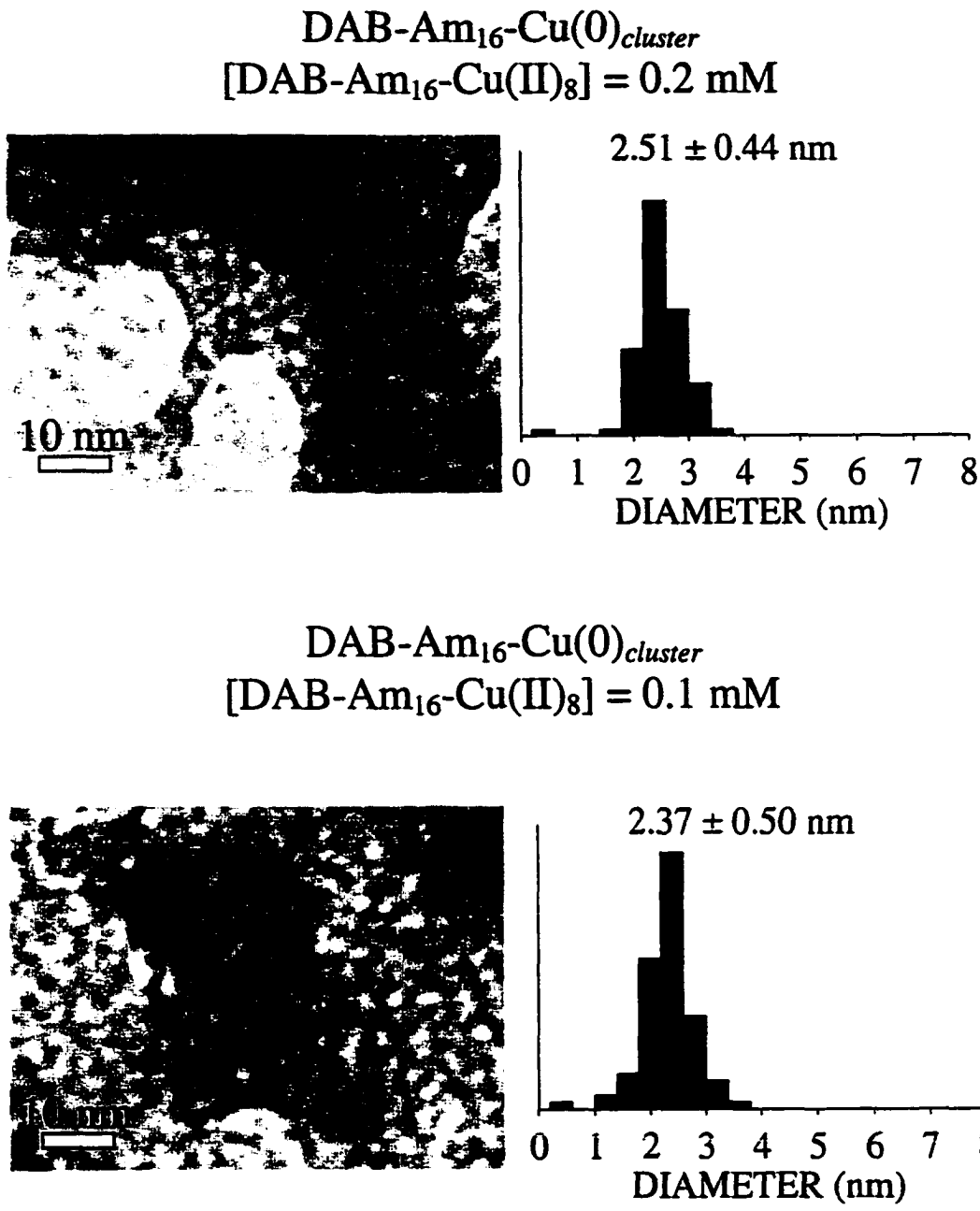

Figure 5.14. TEM images and size distribution of the clusters produced using 0.2 mM, and 0.1 mM DAB-Am_{16}-$Cu(II)_8$.

5.5. Conclusions

EXAFS and XANES have been successfully applied to the determination of the Cu(II) complex geometry formed upon reaction of $Cu(NO_3)_2 \cdot 2.5\ H_2O$ with poly(propylene imine) dendrimers containing 4 to 64 primary amine groups. These techniques, routinely applied in the study of inorganic materials and catalysts, offer a

powerful tool for the structural investigation of supramolecular metal complexes such as the Cu-dendrimer complexes studied in this work. Analysis of the XANES spectra points to an identical environment of the Cu ions in each of the dendrimer end-groups for each generation. The DAB-Am_n-$Cu(II)_x$ complexes were found to be penta-coordinated in a square-base pyramidal geometry. Each Cu ion binds to three nitrogens from the dendrimer dipropylene triamine end group (Cu – N distance=2.03 Å) and an oxygen atom completes the equatorial plane (Cu – O distance=1.92 Å). Another oxygen atom occupies an axial position at about 2.6 Å. To our knowledge, this is the first study which has given clear geometric information on the complexation of Cu(II) poly(propylene imine) dendrimers; such structural information on the precursor is essential for developing a clear picture of Cu(0) nanocluster formation.

The evidence of nanocluster formation upon reduction with $NaBH_4$ is demonstrated in the XANES data by a shift of the K-edge threshold of 1.4 eV. The EXAFS results indicate a decrease in the size of the clusters with increasing dendrimer generation and are in agreement with the TEM results. However, the presence of a peak at about 1.6 Å in the Fourier transforms of the DAB-Am_n-$Cu(0)_{cluster}$ indicates a complex environment of the copper atoms at the cluster surface. We attribute the presence of this peak to Cu-N bonds between the dendrimer and cluster surface as the result of adsorbed dendrimer. Based on this observation and the generation-dependent cluster size, we propose a model in which the dendrimer acts as a surfactant for the copper nanoclusters. For example, clusters synthesized from DAB-Am_4-$Cu(II)_2$, are larger in size because of the more facile diffusion of copper atoms and the smaller size of the dendrimer, which allows for multiple Cu-N bonds on the cluster surface. However, when the size of the dendrimer is increased, steric hindrance impedes

diffusion of copper atoms. This results in a decreased number of Cu-N bonds at the surface of the cluster, and the formation of smaller Cu nanoclusters, which then may be located inside the dendrimer. TEM studies demonstrate that it is possible to further decrease the size of the clusters by varying factors such as concentration and the NH_2 to Cu ratio. Future work will focus on the preparation and characterization of smaller monometallic and bimetallic nanoclusters and the application of EXAFS and XANES to the study of adsorbed Cu-dendrimer complexes on gold.

5.6. Bibliography

5.1) Bosman, A. W. *Dendrimers in Action*; Technische Universiteit Eindhoven: Eindhoven, 1998, pp 142.

5.2) *Increasing the molar ratio of $NaBH_4$ does not induce any change in the UV-vis spectra of any of the DAB-Am_n-$Cu(0)_{cluster}$ complexes but prevents the rapid oxidation of the copper atoms back to Cu(I) or Cu(II), thus increasing their stability.*

5.3) Lemonnier, M.; Collet, O.; Depautex, C.; Esteva, J.-M.; Raoux, D. *Nucl. Instrum. Met.* **1978**, *152*, 109-111.

5.4) Stern, E. A.; Heald, S. M. *Rev. Sci. Instr.* **1979**, *50*, 1579-1582.

5.5) Frahm, R. *Nuclear Instruments and Methods in Physics Research Section A* **1988**, *270*, 578-581.

5.6) Schoonmaker, J. M.; Tittsworth, R. *In Preparation* **2001**.

5.7) Teo, B. K. *EXAFS : Basic principles and data analysis*; Springer-Verlag: New York, 1986.

5.8) Koningsberger, D. C.; Prins, R. *X-ray Absorption - Principles, Applications, Techniques of EXAFS, SEXAFS and XANES*; Wiley and Sons: New York, 1988; Vol. 92.

5.9) Ressler, T. *J. Physique IV* **1997**, *7*, C2-C269.

5.10) Newville, M.; Caroll, S. A.; O'Day, P. A.; Waychunas, G. A.; Ebert, M. *J. Synchrotron Rad.* **1999**, *6*, 276-277.

5.11) Zabinsky, S. I.; Rehr, J. J.; Ankudinov, A.; Albers, R. C.; Eller, M. J. *Phys. Rev. B* **1995**, *52*, 2995-3009.

5.12) Grunes, L. A. *Phys. Rev. B* **1983**, *27*, 2111-2131.

5.13) Bair, R. A.; Goddard III, A. *Phys. Rev. B* **1980**, *22*, 2767-2776.

5.14) Kau, L.-S.; Hodgson, K. O.; Solomon, E. I. *J. Am. Chem. Soc.* **1989**, *111*, 7103-7109.

5.15) Kau, L.-S.; Spira-Solomon, D. J.; Penner-Hahn, J. E.; Hodgson, K. O.; Solomon, E. I. *J. Am. Chem. Soc.* **1987**, *109*, 6433-6442.

5.16) Brown, J. M.; Powers, L.; Kincaid, B.; Larrabee, J. A.; Spiro, T. G. *J. Am. Chem. Soc.* **1980**, *102*, 4210-4216.

5.17) Nomura, M.; Kazusaka, A.; Kakuta, N.; Ukisu, Y.; Miyahara, K. *J. Chem. Soc. Faraday Trans. 1* **1987**, *83*, 1227-1235.

5.18) *A notable difference in the absorption spectra of copper nitrate in solution and in the solid state is observed. This is most likely due to the effect of the MeOH solvent, for the Cu(II) complex may extend its geometry to that of a strongly favored octahedron by weakly binding to solvent molecules or nitrate groups.*

5.19) Onori, G.; Santucci, A.; Scafati, A.; Belli, M.; Della Longa, S.; Bianconi, A.; Palladino, L. *Chem. Phys. Lett.* **1988**, *149*, 289-294.

5.20) Ohtaki, H.; Maeda, M. *Bull. Chem. Soc. Japan* **1974**, *47*, 2197.

5.21) Magini, M. *Inorg. Chem.* **1982**, *21*, 1535.

5.22) Kosugi, N.; Kondoh, H.; Tajima, H.; Kuroda, H. *Chem. Phys.* **1989**, *135*, 149-160.

5.23) Choy, J.-H.; Kim, D.-K.; Park, J.-C.; Choi, S.-N.; Kim, Y.-J. *Inorg. Chem.* **1997**, *36*, 189-195.

5.24) Martens, G.; Rabe, P.; Schwentner, N.; Werner, A. *Phys. Rev. B* **1978**, *17*, 1481-1488.

5.25) Lamberti, C.; Bordiga, S.; Salvalaggio, M.; Spoto, G.; Zecchina, A.; Geobaldo, F.; Vlaic, G.; Bellatrecia, M. *J. Phys. Chem. B* **1997**, *101*, 344-360.

5.26) Fitts, J. P.; Trainor, T. P.; Grolimund, D.; Bargar, J. R.; Parks, G. A.; Brown, J. G. E. *J. Synchrotron Rad.* **1999**, *6*, 627-629.

5.27) Sarode, P. R.; Sankar, G.; Rao, C. N. R. *Proc. Indian Acad. Scie. (Chem. Sci.)* **1983**, *92*, 527-542.

5.28) Palladino, L.; Della Longa, S.; Reale, A.; Belli, M.; Scafati, A.; Onori, G.; Santucci, A. *J. Chem. Phys.* **1993**, *98*, 2720-2726.

5.29) Sano, M.; Komorita, S.; Yamatera, H. *Inorg. Chem.* **1992**, *31*, 459-463.

5.30) Lever, A. B. P. *Inorganic Electronic Spectroscopy, 2nd Edition*; Elsevier: Amsterdam, 1984; Vol. 33.

5.31) Bosman, A. W.; Schenning, A. P. H. J.; Janssen, R. A. J.; Meijer, E. W. *Chem. Ber./Recueil* **1997**, *130*, 725-728.

5.32) Velayutham, M.; Varghese, B.; Subramanian, S. *Inorg. Chem.* **1998**, *37*, 5983-5991.

5.33) *Increases in the Cu(II)-dendrimer complex concentration such that X-ray spectra with sufficiently high S/N ratios could be obtained (needed for accurate structural assignments) were met with frustration due to the limited solubility of the Cu(II)-dendrimer complexes in MeOH.*

5.34) Adams, H.; Bailey, N. A.; Carlisle, W. D.; Fenton, D. E. *Acta Cryst.* **1990**, *C46*, 1439-1441.

5.35) Rehr, J. J. *Surf. Rev. & Lett.* **1995**, *2*, 63-69.

5.36) D'Angelo, P.; Bottari, E.; Festa, M. R.; Nolting, H.-F.; Pavel, N. V. *J. Phys. Chem. B* **1998**, *102*, 3114-3122.

5.37) Carrado, K. A.; Wasserman, S. R. *J. Am. Chem. Soc.* **1993**, *115*, 3394-3395.

5.38) D'Angelo, P.; Bottari, E.; Festa, M. R.; Nolting, H.-F.; Pavel, N. V. *J. Chem. Phys.* **1997**, *107*, 2807-2812.

5.39) Korshin, G. V.; Frenkel, A. I.; Stern, E. A. *Env. Sci. Technol.* **1998**, *32*, 2699-2705.

5.40) Inada, Y.; Ozutsumi, K.; Funahashi, S.; Soyama, S.; Kawashima, T.; Tanaka, M. *Inorg. Chem.* **1993**, *32*.

5.41) *All possible combinations for a total of 4 atoms were considered when the fitting procedures were implemented.*

5.42) *The additional peaks in the Fourier-transform data are due to contributions arising from multiple scattering from the high number of carbon atoms surrounding the Cu(II) or possibly a weakly bound oxygen from water, methanol or nitrate. In addition, the back Fourier transform of the peaks between 2 and 4 Å presents some characteristics of heavy element backscattering. Furthermore, a beat node indicative of atoms with very different backscattering function frequencies can be observed in the EXAFS function. Thus, the proximity of another copper atom contributing to the EXAFS of the absorber can not be excluded and was considered in the fits.*

5.43) Alagna, L.; Prosperi, T.; Tomlinson, A. A. G.; Vlaic, G. *J. Chem. Soc. Dalton Trans.* **1983**, 645-648.

5.44) Montano, P. A.; Shenoy, G. K.; Alp, E. E.; Shulze, W.; Urban, J. *Phys. Rev. Lett.* **1986**, *56*, 2076-2079.

5.45) Rothe, J.; Hormes, J.; Bönnemann; Brijoux, W.; Siepen, K. *J. Am. Chem. Soc.* **1998**, *120*, 6019-6023.

5.46) Abe, H.; Charle, K. P.; Tesche, B.; Schulze, W. *Chem. Phys.* **1982**, *68*, 137-141.

5.47) Curtis, A. C.; Duff, D. G.; Edwards, P. P.; Jefferson, D. A.; Johnson, B. F. G.; Kirkland, A. I.; Wallace, A. S. *Angew. Chem. Int. Ed. Engl.* **1988**, *27*, 1530-1533.

5.48) Lisiecki, I.; Pileni, M. P. *J. Am. Chem. Soc.* **1993**, *115*, 3887-3896.

5.49) Lisiecki, I.; Billoudet, F.; Pileni, M. P. *J. Phys. Chem.* **1996**, *100*, 4160-4166.

5.50) Traverse, A.; Parent, P.; Mimault, J.; Hagège, S.; Du, J. *Nucl. Instr. and Meth. B* **1994**, *84*, 204-207.

5.51) Telgheder, F.-W.; Urban, J. *J. Electron. Spec. & Rel. Phenom.* **1998**, *95*, 267-279.

5.52) Gota, S.; Gautier, M.; Douillard, L.; Thromat, N.; Duraud, J. P.; Le Fèvre, P. *Surf. Sci.* **1995**, *323*, 163-174.

5.53) Borowski, M. *J. Physique IV* **1997**, *C2*, 259-260.

5.54) Apai, G.; Hamilton, J. F.; Stöhr, J.; Thompson, A. *Phys. Rev. Lett.* **1979**, *43*, 165-169.

5.55) *Although these authors have found different results in the determination of the size of clusters ranging from dimers to 40 Å Cu clusters, they showed that there is a strong correlation between bond distance of the first coordination shell and the size of the clusters. Additionally, they agreed on the decrease of the bond distance being a manifestation of the decrease in size of the cluster.*

5.56) Lamberti, C.; Spoto, G.; Scarano, D.; Paze, C.; Salvalaggio, M.; Bordiga, S.; Zecchina, A.; Turnes; Palomino, G.; D'Acapito, F. *Chem. Phys. Lett.* **1997**, *269*, 500-508.

5.57) Wiell, T.; Klepeis, J. E. *Phys. Rev. B* **1998**, *58*, 1655-1664.

5.58) Wende, H.; Arvanitis, D.; Tischer, M.; Chauvistre, R.; Henneken, H.; May, F.; Baberschke, K. *Phys. Rev. B* **1996**, *54*, 5920-5926.

Chapter 6. Summary and Outlook

6.1. General

The previous chapters describe a wide variety of new data that have been generated and interpreted for new classes of chemically significant systems. However, it should be realized that these results represent a first step. Many refinements, as well as fundamentally new studies, are suggested by the work done to date. This chapter summarizes what has been accomplished and also describes useful new experimnents suggested by the completed work.

6.2. Mixed Monolayers

Mixed monolayers composed of an electroactive group and simple *n*-alkanethiols have been used to investigate interfacial electron transfer on chemically modified surfaces.[1-5] These studies have shown that the structure and composition of the mixed monolayers depend on the physical and chemical properties of the electroactive group, the chain length and the molar fraction of both of the components. Electrochemical studies of mixed monolayers containing ferrocene-terminated alkanethiols and an *n*-alkanethiol of various chain lengths[6,7] have demonstrated that when the chain length of the *n*-alkanethiol is longer than that of the ferrocene-terminated thiol, the surface coverage of the ferrocene constituent is decreased and variations of the redox potential to more positive values are observed. The GIXAFS results obtained by our group on both ferrocene-terminated thiol monolayers and mixed monolayers show that XAFS is an alternative method to study these systems and could deliver a great deal of information on these structures. Coupled with the emerging capability of measuring EXAFS signals in a very short time - as shown in Chapter 5 with the QUICKEXAFS studies of copper-dendrimer nanoparticles - it should now be

possible to realize a combined in situ electrochemistry-XANES experiment in which, minute changes of the ferrocene environment could be probed by XANES as the electrochemical potentials are scanned using cyclic voltammetry.

6.3. *n*-Alkanethiol Monolayers on Au, Ag, and Cu

Improvement of the data obtained for *n*-alkanethiols on Au would be possible through the use of a 13-element Ge detector.[8] As shown by the results obtained for *n*-alkanethiols on Ag, and comparison of Figure 4.7 and Figure 4.8, the apparatus used at CAMD is as sensitive as the one used in Bonn to collect the published alkanethiol data.[9] The GIXAFS technique offers a great control over the incidence angle, and the method can be implemented by a more efficient detection and amplification of the small sulfur signal and filtering of the strong gold fluorescence. This could be achieved with the use of a 13-element detector where each diode acts as a single detector but where the signals collected by the 13 diodes can be collected and added up together. This new feature could also benefit the investigations of *n*-alkanethiols on Ag. However, the data that was obtained for the n-alkanethiols on Ag was of very sufficient quality to be able to detect variations in the XANES spectra as a function of chain length and very shallow angles. It was shown that among the series that was investigated (C_6, C_{12}, C_{14}, C_{16}, C_{18}, and C_{22}), the amount of oxidation decreased with increasing chain length.

6.4. Thiol-Capped Ag Nanoparticles

In our XANES studies of *n*-alkanethiols on Ag, it was proposed that the substrate might play a role in the appearance of a particular feature for C_{18}. We are interested in pursuing a series of experiments where the effect of the chain length is probed for *n*-alkanethiols adsorbed on various Ag substrates. An interesting way to realize this is to fabricate Ag nanoparticles of different sizes which should display

significant variations in their surfaces (orientations, step-edge density). These nanoparticles can be derivatized with alkanethiols of different chain lengths. Most of the studies of thiol-capped metal nanoparticles involve gold clusters[10-21] with just a few concerning silver nanoparticles.[17,18,22-25] By acquiring sulfur K-edge and silver K-edge XANES spectra of these systems, we can study the adsorption of *n*-alkanethiols on Ag particles, and we expect to be able to draw important conclusions regarding the influence of the substrate by comparing the results with that obtained from *n*-alkanethiols adsorbed on planar Ag. A series of small (≈5 nm), medium (≈30 nm), and large (≈100-200 nm) particles can be synthesized and capped with C_6, C_{12}, and C_{18} for each size (drawn to scale in Figure 6.1).[22]

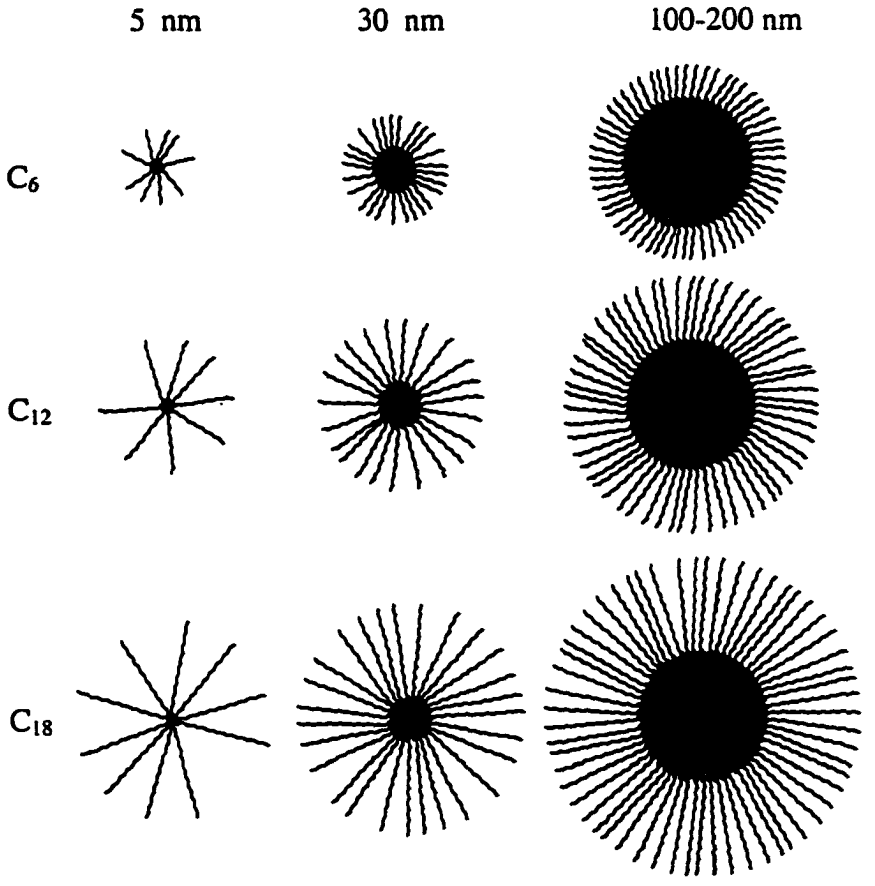

Figure 6.1. Cartoon depicting the thiol-capped Ag nanoparticles.

As the size of the particles increases, the surface of the particles is expected to begin to resemble that of a flat Ag(111) surface. Thus, the XANES spectra should display similarities with those of *n*-alkanethiols adsorbed on Ag/Si. However, when the size of the particles is decreased to just a few nanometers, important changes in the surface of the particles should induce significant variations in the adsorption of the sulfur atoms on the surface and could be monitored by XANES spectroscopy. Such variations in S adsorption sites have been shown for thiols on Au nanoparticles.[12]

Preliminary experiments were conducted at the DCM beamline at CAMD. Samples of Ag nanoparticles capped with C_6, C_{12}, and C_{18} were synthesized according to a procedure described in the literature.[22] This one-phase synthesis is reported to result in the formation of thiol-capped Ag nanoparticles of about 8 nm in diameter. Powders were obtained by evaporation of the solvent (ethanol) and placed between layers of kapton tape for scans in the transmission mode. The spectrum of the C_{12}-capped Ag nanoparticles is given as an example in Figure 6.2.

This spectrum presents fundamental differences between that of free *n*-dodecanethiol indicating that the sulfur species present are adsorbed on the Ag surface. In addition, similarities with the spectra of adsorbed C_{12} on planar Ag can be observed. The silver L_{III}-edge spectra for C_6, C_{12}, and C_{18} exhibit cluster size effects as noted by the dampening of the oscillations seen for that of a Ag foil but demonstrate the metal-like character of the silver nanoparticles (Figure 6.3).

These preliminary studies set the stage for new experiments that will further our understanding of alkanethiol adsorption on metal surfaces.

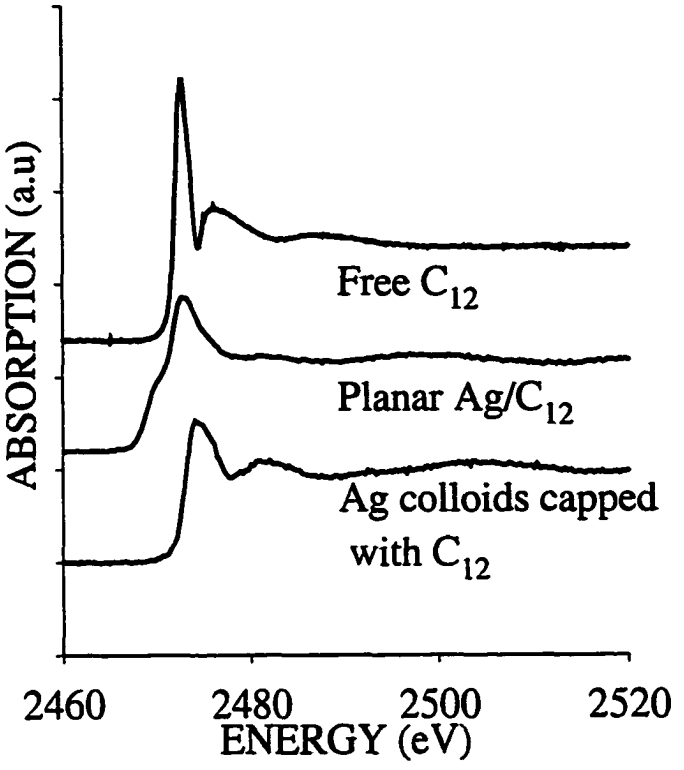

Figure 6.2. Sulfur K-edge spectrum of *n*-dodecanethiol on silver nanoparticles compared to that of C_{12} on planar Ag and free C_{12}.

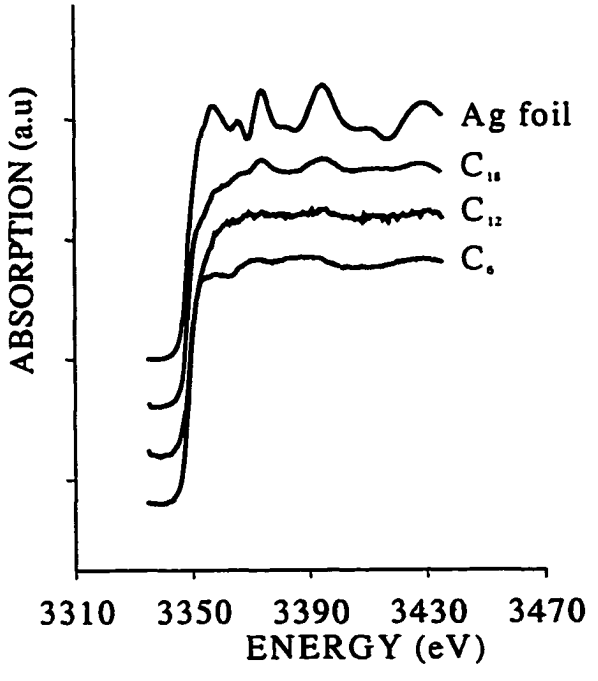

Figure 6.3. Silver L_{III}-edge spectrum of *n*-alkanethiols on silver nanoparticles compared to that of a metallic Ag foil.

6.5. Ferrocene-Functionalized Dendrimers

Poly(propylene imine) dendrimers can be functionalized with ferrocene end-groups.[26-28] As for the DAB-Am_n-$Cu(II)_x$ series, the spatial architecture of the dendrimer itself is not known, and functionalizing the outside of the dendrimer with ferrocene could give us some insight into the structure of such assemblies. In particular, as the size of the dendrimer increases with increasing generation, steric hindrance could force the ferrocene units to get closer to each other. We have conducted preliminary EXAFS studies of generation 1 to 5 ferrocenyl dendrimers or DAB-Am_n-Fc_n, (n=4 to 64), and ferrocene (Fc), and polyvinyl-ferrocene (pvFc) as reference standards. The Fourier transform of the EXAFS function for each generation measured in the solid state is shown in Figure 6.4 as well as those of Fc and pvFc. No noticeable difference can be seen between the XANES spectra of the dendrimers, indicating that they all share a similar chemical environment. Slight changes can be detected in the Fourier transforms of their EXAFS functions. When compared to Fc and pvFc, a shift of the absorption edge to lower energy for the Fc dendrimers indicates the presence of the carbonyl electron-withdrawing group close to the ferrocene unit in the dendrimer. The Fourier transforms obtained for generations 1, 2, and 3 present the same shape as that of pvFc in the region following the first coordination shell corresponding to 10 carbon atoms.

However, some change is discernable for generations 4 and 5, with the Fourier transform of generation 5 appearing identical to that of Fc. Fourier back-transforms of the region between 2 and 4 $Å^{-1}$ indicate the possible presence of a heavy backscatterer for generation 4 and 5. This means that as the generation of the dendrimer increases, some ferrocene groups are moving closer to each other, enough to generate this signal

in the Fourier back-transform. More studies are planned of adsorbed DAB-Am$_n$-Fc$_n$ on gold surfaces, which are expected to show increased interaction of the ferrocene groups due to distortion of the dendrimers on the surface.[29,30]

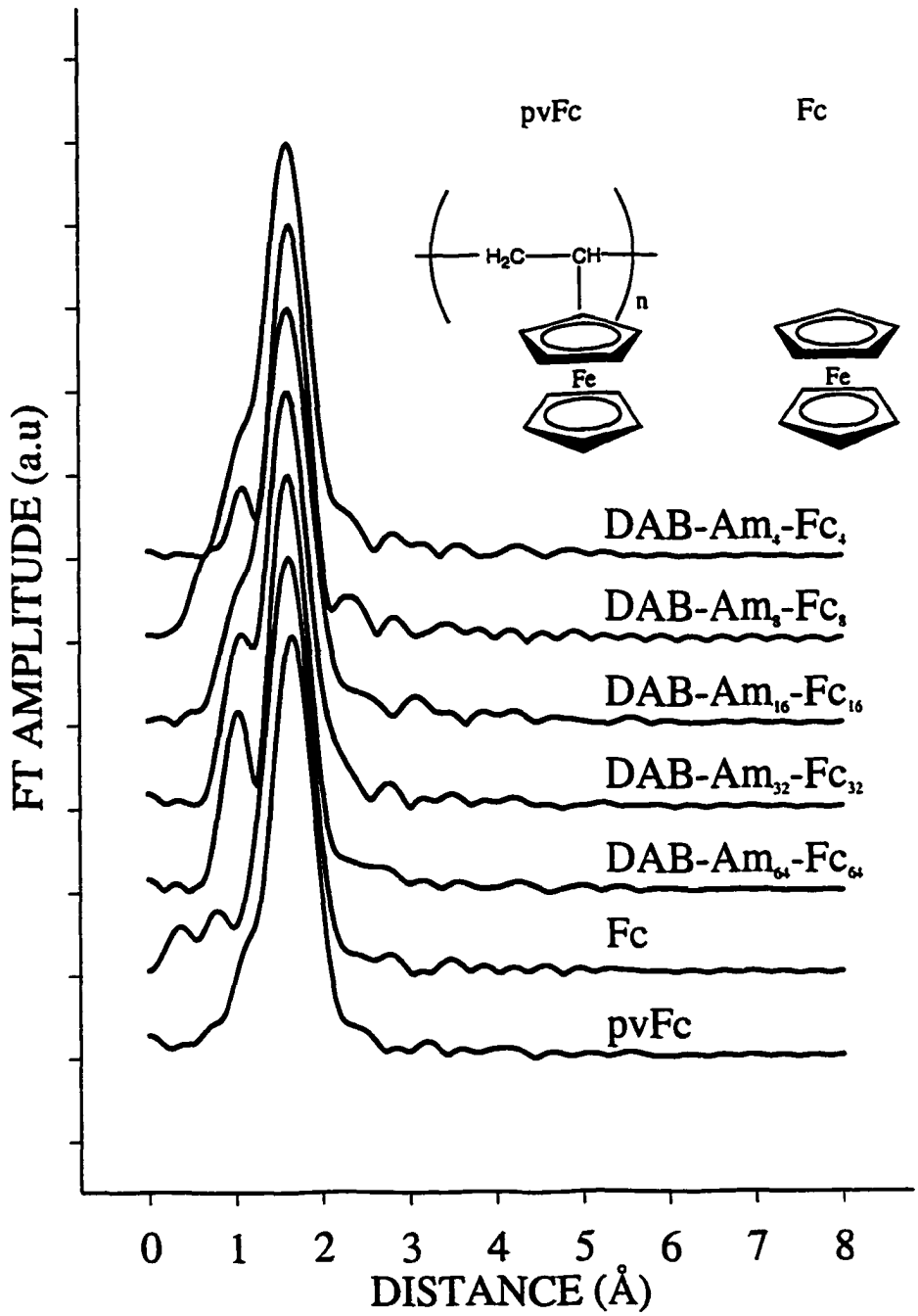

Figure 6.4. Fourier transforms of the EXAFS function for the series of DAB-Am$_n$-Fc$_x$, and reference standards.

Recently proposed mixed dendrimers-alkanethiols systems present some novel characteristics that complement those of SAMs of alkanethiols by extension to a three-dimensional architecture. Dendrimers have been shown to be compressed on the surface upon coadsorption with alkanethiols on surfaces,[31,32] which gives us a way to study and control the ferrocene groups interaction. The work presented in this dissertation outlines possible ways in which to study these systems at the iron K-edge and at the sulfur K-edge at grazing incidence angles in order to obtain structural information.

6.6. Bimetallic Clusters

The advances realized in the characterization of dendrimers as shown by the EXAFS, XANES, and TEM work on the DAB-Am_n-$Cu(II)_x$ and the nanoparticles in the DAB-Am_n-$Cu(0)_{cluster}$ series created upon reduction of the dendrimer-copper complexes (Chapter 5) open new avenues in the fabrication of nanoparticles and their characterization. In particular, it was shown that we can obtain very small (≈1.6 nm) and very monodisperse particles when reducing the ratio of Cu to amine groups. It is also possible to load the dendrimers with two different metallic ions and use the dendrimers as templates for the production of bimetallic nanoclusters. Such clusters[33-36] are of high interest for potential applications in catalysis. A combination of the dendrimer work presented here with routine EXAFS experiments on bimetallic clusters is proposed in order to effectively design nanoparticles composed of mixed metals and of a chosen composition. This would be very useful in a number of applications. For example, in the design of carbon nanotubes, the size of the catalyst used during the chemical vapor depostion process governs the diameter of the structures produced.[37-46] The increased control of the size and composition of the catalyst using the dendrimer

synthesis route, combined with the possibility to adsorb the dendrimers on surfaces could lead to great advances in the production of carbon nanotubes and their use for patterning surfaces and creating three-dimensional nano-architectures.

6.7. Bibliography

6.1) Chidsey, C. E. D.; Loiancono, D. N. *Langmuir* **1990**, *6*, 682.

6.2) Whitesides, G. M.; Laibinis, P. E. *Langmuir* **1990**, *6*, 87.

6.3) Bain, C. D.; Whitesides, G. M. *J. Am. Chem. Soc.* **1989**, *111*, 7155.

6.4) Bain, C. D.; Whitesides, G. M. *J. Am. Chem. Soc.* **1989**, *111*, 7164.

6.5) Bain, C. D.; Whitesides, G. M. *Science* **1988**, *240*, 62.

6.6) Creager, S. E.; Rowe, G. K. *Anal. Chim. Acta* **1991**, *246*, 233-239.

6.7) Chidsey, C. E.; Bertozzi, C. R.; Putvinsky, T. M.; Mujsce, A. M. *J. Am. Chem. Soc.* **1990**, *112*, 4301-4306.

6.8) Cramer, S. P.; Tench, O.; Yocum, M.; George, G. N. *Nucl. Instrum. Meth. A* **1988**, *266*, 586.

6.9) Floriano, P. N.; Schlieben, O.; Doomes, E. E.; Klein, I.; Janssen, J.; Hormes, J.; Poliakoff, E. D.; McCarley, R. L. *Chem. Phys. Lett.* **2000**, *321*, 175-181.

6.10) Grabar, K. C.; Freeman, R. G.; Hommer, M. B.; Natan, M. J. *Anal. Chem.* **1995**, *67*, 735-743.

6.11) Badia, A.; Gao, W.; Singh, S.; Demers, L.; Cuccia, L.; Reven, L. *Langmuir* **1996**, *12*, 1262-1269.

6.12) Bourg, M.-C.; Badia, A.; Lennox, B. *J. phys. Chem. B* **2000**, *104*, 6562-6567.

6.13) Chen, S. *J. Phys. Chem. B* **2000**, *104*, 663-667.

6.14) Hostetler, M. J.; Wingate, J. E.; Zhong, C.-J.; Harris, J. E.; Vachet, R. W.; Clark, M. R.; Londono, J. D.; Green, S. J.; Stokes, J. J.; Wignall, G. D.; Glish, G. L.; Porter, M. D.; Evans, N. D.; Murray, R. W. *Langmuir* **1998**, *14*, 17-30.

6.15) Fitzmaurice, D.; Rao, S. N.; Preece, J. A.; Stoddart, J. F.; Wenger, S.; Zaccheroni, N. *Angew. Chem. Int. Ed.* **1999**, *38*, 1147-1150.

6.16) Martin, J. E.; Wilcoxon, J. P.; Odinek, J.; Provencio, P. *J. Phys. Chem. B* **2000**, *104*, 9475-9486.

6.17) Bensebaa, F.; Zhou, Y.; Deslandes, Y.; Kruus, E.; Ellis, T. H. *Surf. Sci.* **1998**, *405*, L472-L476.

6.18) Venkataramanan, M.; Ma, S.; Pradeep, T. *J. Coll. Interface Surf.* **1999**, *216*, 134-142.

6.19) Zanchet, D.; Tolentino, H.; Martins Alves, M. C.; Alves, O. L.; Ugarte, D. *Chem. Phys. Lett.* **2000**, *323*, 167-172.

6.20) Badia, A.; Cuccia, L.; Demers, L.; Morin, F.; Lennox, R. B. *J. Am. Chem. Soc.* **1997**, *119*, 2682-2692.

6.21) Weisbecker, C. S.; Merritt, M. V.; Whitesides, G. M. *Langmuir* **1996**, *12*, 3763-3772.

6.22) Kang, S. Y.; Kim, K. *Langmuir* **1998**, *14*, 226-230.

6.23) Ah, C. S.; Han, H. S.; Kim, K.; Jang, D.-J. *J. phys. Chem. B* **2000**, *104*, 8153-8159.

6.24) Rodriguez-Sanchez, L.; Blanco, M. C.; Lopez-Quintela, M. A. *J. Phys. Chem. B* **2000**, *104*, 9683-9688.

6.25) Korgel, B. A.; Fitzmaurice, D. *Phys. Rev. B* **1999**, *59*, 14191-14201.

6.26) Casado, C. M.; Gonzalez, B.; Cuadrado, I.; Alonso, B.; Moran, M.; Losada, J. *Angew. Chem. Int. Ed.* **2000**, *39*, 2135-2138.

6.27) Cuadrado, I.; Casado, C. M.; Alonso, B.; Morán, M.; Losada, J.; Belsky, V. *J. Am. Chem. Soc.* **1997**, *119*, 7613-7614.

6.28) Cuadrado, I.; Morán, M.; Casado, C. M.; Alonso, B.; Losada, J. *Coord. Chem. Rev.* **1999**, *193-195*, 395-445.

6.29) Hierlemann, A.; Campbell, J. K.; Baker, L. A.; Crooks, R. M.; Ricco, A. J. *J. Am. Chem. Soc.* **1998**, *120*, 5323-5324.

6.30) Tsukruk, V. V.; Rinderspacher, F.; Bliznyuk, V. N. *Langmuir* **1997**, *13*, 2171-2176.

6.31) Lackowski, W. M.; Campbell, J. K.; Edwards, G.; Chechik, V.; Crooks, R. M. *Langmuir* **1999**, *15*, 7632-7638.

6.32) Tokuhisa, H.; Zhao, M.; Baker, L. A.; Phan, V. T.; Dermody, D. L.; Garcia, M. E.; Peez, R. F.; Crooks, R. M.; Mayer, T. M. *J. Am. Chem. Soc.* **1998**, *120*, 4492-4501.

6.33) Nashner, M. S.; Somerville, D. M.; Lane, P. D.; Adler, D. L.; Shapley, J. R.; Nuzzo, R. G. *J. Am. Chem. Soc* **1996**, *118*, 12964-12974.

6.34) Nashner, M. S.; Frenkel, A. I.; Adler, D. L.; Shapley, J. R.; Nuzzo, R. G. *J. Am. Chem. Soc.* **1997**, *119*, 7760-7771.

6.35) Bondos, J. C.; Drummer, N. E.; Gewirth, A. A.; Nuzzo, R. G. *J. Am. Chem. Soc.* **1999**, *121*, 2498-2507.

6.36) Hills, C. W.; Nashner, M. S.; Frenkel, A. I.; Shapley, J. R.; Nuzzo, R. G. *Langmuir* **1999**, *15*, 690-700.

6.37) Su, M.; Zheng, B.; Liu, J. *Chem. Phys. Lett.* **2000**, *322*, 321-326.

6.38) Su, M.; Li, Y.; Maynor, B.; Buldum, A.; Lu, J. P.; Liu, J. *J. Phys. Chem. B* **2000**, *104*, 6505-6508.

6.39) Shelimov, K. B.; Moskovits, M. *Chem. mater.* **2000**, *12*, 250-254.

6.40) Ajayan, P. M. *Chem. Rev.* **1999**, *99*, 1787-1799.

6.41) Cassell, A. M.; Raymakers, J. A.; Kong, J.; Dai, H. *J. phys. Chem. B* **1999**, *103*, 6484-6492.

6.42) Bower, C.; Zhou, O.; Zhu, W.; Werder, D. J.; Ji, S. *Appl. Phys. Lett.* **2000**, *77*, 2767-2769.

6.43) Gates, B.; Yin, Y.; Xia, Y. *J. Am. Chem. Soc.* **2000**, *122*, 12582-12583.

6.44) Kong, J.; Cassell, A. M.; Dai, H. *Chem. Phys. Lett.* **1998**, *292*, 567-574.

6.45) Kukovecz, A.; Konya, Z.; Nagaraju, N.; Willems, I.; Tamasi, A.; Fonseca, A.; Nagy, J. B.; Kiricsi, I. *Phys. Chem. Chem. Phys.* **2000**, *2*, 3071-3076.

6.46) Ma, X.; Wang, E. G.; Tilley, R. D.; Jefferson, D. A.; Zhou, W. *Appl. Phys. Lett.* **2000**, *77*, 4136-4138.

Appendix I. X-Ray Properties of Au, Cu, Ag, Fe, and S

	79	47	29	26	16
	196.96	107.86	63.546	55.847	32.066
	2602.0	823.1	1240.0	150	214.8
	1.1624× 10^{-2}	1.7267× 10^{-2}	2.0493 ×10^{-2}	6.7998 ×10^{-2}	3.7682 ×10^{-2}
	19.3	10.5	8.96	7.87	2.05
	0.1989	1.157	0.9003	8.482	22.71
	1.45	1.33	1.35	0.335	0.395
	80713	25517			
	14353	3810	1100	849	193
	13733	3528	953	721	164
	11919	3352	933	708	163
	3379	734	135	93	
	3149	619	90		
		588			
		389			
		383			
	762				
	642				
	546				
	353				
	335				
	87				
	83				
	107				
	74				
	57				

Appendix II. Data Analysis Procedures

This appendix is a brief summary of the steps involved in EXAFS data analysis. The reader is strongly encouraged to refer to literature that is listed in Chapter 2 as well as manuals that can be obtained for the software mentioned in this appendix.

Raw data is obtained and the background is subtracted using Winxas 97 or autobk. The procedures are automated in Winxas and were achieved by fitting a polynomial of first order to the pre-edge and a 3rd order polynomial to the post-edge. Background removal with autobk necessitates the use of an autobk input file (autobk.inp), dos4gw.exe, and autobk.exe. The program runs in DOS. The raw data file (with an extension .dat) that is used in autobk.inp has a format that can be created by importing the raw data in Winxas. The energy units need to be converted to eV. The proper procedure consists in opening the file saved under Winxas with Axum 5.0. Axum opens it as a program file. The three first lines must be deleted, and the rest selected and copied into a microsoft wordpad template document. The template document consists of the following succesion of characters:

#----------

energy xmu

The selection obtained in Axum must be pasted after the first two lines. Background removal with Winxas normalizes the edge jump to 1. Normalization can also be obtained with autobk (see autobk manual). A background-removed and normalized Cu spectrum is shown in Figure II.1.

After determination of E_0, the spectrum is then converted from energy space to k space using equation 2.3 in section 2.1.5.1. An example is given for Cu in Figure II.2.

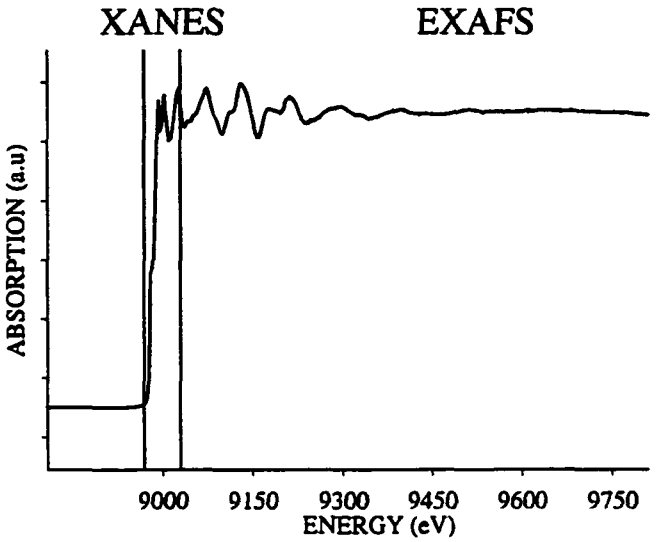

Figure II.1. Background removed and normalized Cu fcc foil spectrum.

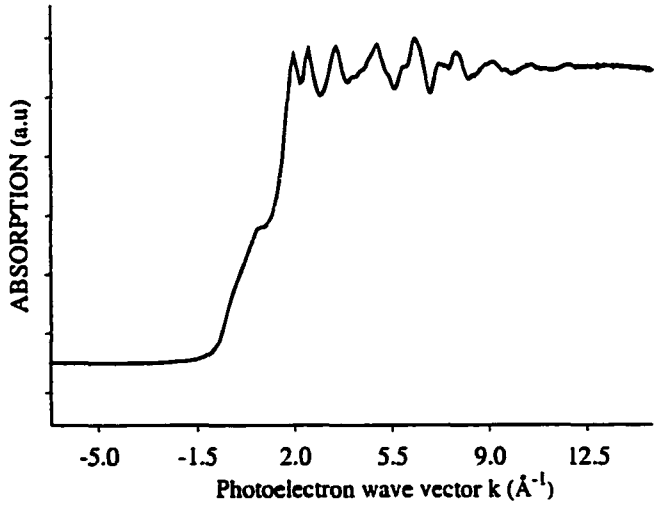

Figure II.2. Conversion to k space and μ_0 (k) correction.

The next step or correction consists in determining the atomic absorption in the EXAFS region and extracting the EXAFS function by fitting a series of cubic splines to approximate the total absorption curve μ (k) with a smooth background absorption curve μ_o (k). This step is illustrated by Figure II.3.

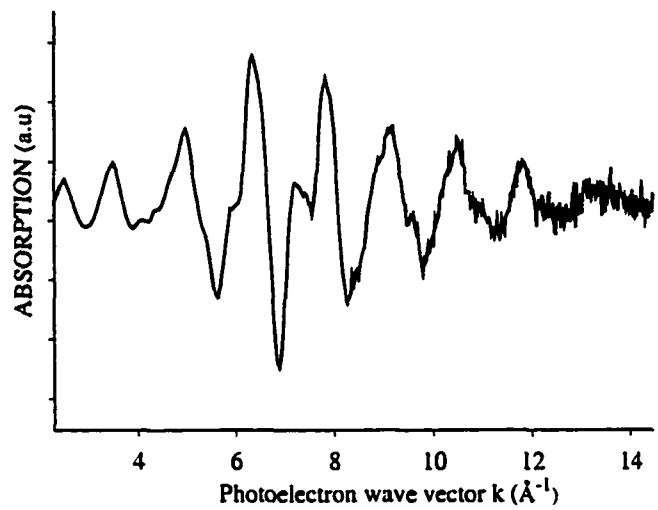

Figure II.3. EXAFS function extracted from the spectrum in Figure II.2.

The obtained χ(k) versus k curve or EXAFS function is weighted by k^n in order to compensate for the attenuation of the EXAFS amplitude at high k. The EXAFS function is then Fourier transformed and results in a curve of amplitude versus distance as shown in Figure II.4.

Curve fitting is based on least-squares and aims at best fitting the $k^n\chi(k)$ or its Fourier transform with theoretical models.

The solid lines in Figure II.4 represent the experimental data and the fit is represented by the dotted lines.

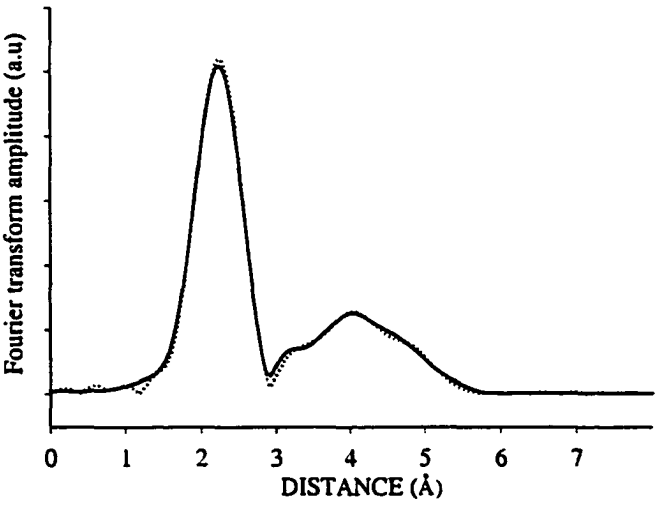

Figure II.4. Fourier transform of the EXAFS function form Figure II.3.

Vita

Pierre N. Floriano was born in Besançon, France, on October 19th, 1970. He went to high school in Besançon, and joined the Faculté des Sciences et des Techniques of Besançon as an undergraduate after the completion of his Baccalauréat C. After obtaining a Diplôme d'Etudes Universitaires Générales (D. E. U. G.) in mathematics, physics, and chemistry in 1991, he obtained a License and Maîtrise in chemistry and applied electrochemistry, in 1992 and 1993, respectively, at the same university. He completed his French education with a Diplôme d'Etudes Approfondies (D. E. A.) in physical chemistry in May 1994. He served in the French Army from 1994 to 1995, and then came to the United States of America with his wife Christy. He expects to receive his Degree of Doctor of Philosophy in chemistry in May 2001 in the doctoral program that he started in August 1996 in the department of Chemistry at Louisiana State University.

DOCTORAL EXAMINATION AND DISSERTATION REPORT

Candidate: Pierre Floriano

Major Field: Chemistry

Title of Dissertation: X-Ray Absorption Fine Structure (EXAFS and XANES) and Microscopic Investigations of Supramolecular Systems

Approved:

Major Professor and Chairman

Dean of the Graduate School

EXAMINING COMMITTEE:

Date of Examination:

March 9, 2001